Advanced modulation formats and signal processing for high speed spectrally efficient optical communications

Rafael Rios Müller

Spécialité : Electronique et communications

Ecole doctorale : Informatique, Télécommunications et Electronique de Paris

Présentée par

Rafael Rios Müller

Pour obtenir le grade de
DOCTEUR DE TELECOM SUDPARIS

Soutenue le 20/04/2016

Formats de modulation et traitement du signal avancés pour les communications optiques très hauts débits à forte efficacité spectrale

Devant le jury composé de :

Directeur de thèse
Prof. Badr-Eddine Benkelfat

Encadrants
Dr. Jérémie Renaudier
Dr. Yann Frignac

Rapporteurs
Prof. Magnus Karlsson
Prof. Gabriella Bosco

Examinateurs
Prof. Abderrahim Ramdane
Prof. Darli Augusto de Arruda Mello
Prof. Frédéric Lehmann

N° NNT : 2016TELE0006

Contents

Résumé

La détection cohérente combinée avec le traitement du signal s'est imposée comme le standard pour les systèmes de communications optiques longue distance à 100 Gb/s (mono-porteuse) et au-delà. Avec l'avènement des convertisseurs numérique-analogique à haute vitesse et haute résolution, la génération de formats de modulation d'ordre supérieur avec filtrage numérique est devenue possible, favorisant l'émergence de transmissions à forte densité spectrale. Par ailleurs, la généralisation des liaisons non gérées en dispersion permet une modélisation analytique du canal optique et favorise l'utilisation d'outils puissants de la théorie de l'information et du traitement du signal.

En s'appuyant sur ces outils, de nouveaux formats de modulation à entrelacement temporel dits hybrides et formats multidimensionnels sont étudiés et mise en œuvre expérimentalement. Leur impact sur les algorithmes de traitement du signal et sur le débit d'information atteignable est analysé en détail.

La conception de transpondeurs de prochaine génération à 400 Gb/s et 1 Tb/s reposant sur des signaux à débit-symbole élevé est également étudiée, dans le but de permettre une réduction du coût par bit à travers de l'augmentation de la capacité émise par transpondeur. L'élaboration d'algorithmes de traitement du signal avancés associées à l'utilisation de composants optoélectroniques à l'état de l'art ont permis la démonstration d'expériences records: d'une part la première transmission mono-porteuse à 400 Gb/s sur une distance transatlantique (pour une efficacité spectrale de 6 b/s/Hz), et d'autre part la première transmission à 1 Tb/s basée sur la synthèse en parallèle de plusieurs sous-bandes spectrales (8 b/s/Hz).

Abstract

Coherent detection in combination with digital signal processing is now the de facto standard for long-haul high capacity optical communications systems operating at 100 Gb/s per channel and beyond. With the advent of high-speed high-resolution digital-to-analog converters, generation of high order modulation formats with digital pulse shaping has become possible allowing the increase of system spectral efficiency. Furthermore, the widespread use of transmission links without in-line dispersion compensation enables elegant analytical optical channel modeling which facilitates the use of powerful tools from information theory and digital signal processing.

Relying on these aforementioned tools, the introduction of time-interleaved hybrid modulation formats, multi-dimensional modulation formats, and alternative quadrature amplitude modulation formats is investigated in high-speed optical transmission systems. Their impact on signal processing algorithms and achievable information rate over optical links is studied in detail.

Next, the design of next generation transponders based on high symbol rate signals operating at 400 Gb/s and 1 Tb/s is investigated. These systems are attractive to reduce the cost per bit as more capacity can be integrated in a single transponder. Thanks to the development of advanced signal processing algorithms combined with state-of-the-art opto-electronic components, record high-capacity

transmission experiments are demonstrated: the first single carrier 400 Gb/s transmission over transatlantic distance (at 6 b/s/Hz) and the first 1 Tb/s net data rate transmission based on the parallel synthesis of multiple spectral sub-bands (at 8 b/s/Hz).

List of acronyms and symbols

List of acronyms

ADC	analog to digital converter
ASE	amplified spontaneous emission
AWGN	additive white Gaussian noise
BER	bit error rate
BICM	bit interleaved coded modulation
BPS	bits per symbol
BPSK	binary phase shift keying
CD	chromatic dispersion
CMA	constant modulus algorithm
CFE	carrier frequency estimation
CPE	carrier phase estimation
DAC	digital-to-analog converter
DBP	digital backpropagation
DCF	dispersion compensation fiber
DD	Direct detection or decision directed
DEMUX	demultiplexer
DFB	distributed feedback laser
DFE	decision feedback equalizer
DMT	discrete multi-tone
DSP	digital signal processing

ECL	external cavity laser
EDFA	Erbium doped fiber amplifier
FEC	forward error correction
FIR	finite impulse response
GMI	generalized mutual information
GNM	Gaussian noise model
HD	hard-decision
HI	horizontal in-phase
HQ	horizontal quadrature
IC/NLC	intra-channel nonlinear compensation
IM	intensity modulation
ISI	inter-symbol interference
ITU	international telecommunication union
LSPS	loop synchronous polarization scrambler
LDPC	low density parity check
MAP	maximum a posteriori
MI	mutual information
MIMO	multiple-input multiple-output
ML	maximum likelihood
MUX	multiplexer
MZM	Mach-Zendher modulator
NCG	net coding gain
NF	noise figure
NLT	nonlinear threshold
OFDM	frequency division multiplexing
OSA	optical spectrum analyser
OSNR	optical signal to noise ratio
PAM	pulse amplitude modulation
PBC	polarization beam combiner

PBS	polarization beam splitter
PDM	polarization division multiplexing
PMD	polarization mode dispersion
PMF	polarization maintaining fibre
PSCF	pure silica core fibre
PSK	phase shift keying
QAM	quadrature amplitude modulation
QPSK	quaternary phase shift keying
RC	raised-cosine
RRC	root-raised-cosine
RZ	return-to-zero
RX	receiver
SE	spectral efficiency
SER	symbol error ratio
SC	spatially-coupled
SD	soft-decision
SMF	single mode fiber
SNR	signal to noise ratio
SP	set-partioned
SSMF	standard single mode fibre
TX	transmitter
VI	vertical in-phase
VOA	variable optical attenuator
VQ	vertical quadrature
WDM	wavelength division multiplexing
WSS	wavelength selective switch

List of symbols

^	estimation
α	attenuation coefficient
β	mode-propagation constant
ε	error
λ	optical wavelength
γ	nonlinear coefficient
τ	skew
μ	stochastic gradient descent step
γ_{NLI}	nonlinear noise coefficient using Gaussian approximation
ω	angular frequency
$\psi_k(t)$	basis waveforms
B_{ref}	reference bandwidth
b_i	i-th bit of a symbol
c	speed of light in the vacuum ($c=2.99792 \cdot 10^8$ m/s)
d_{min}	minimum Euclidean distance
D	dispersion factor
erfc()	complementary error function
$\mathbb{E}(\,)$	expected value
f	frequency
F	noise factor
$\mathcal{F}(\quad)$	Fourier transform
G	generator matrix
h(t)	impulse response
h	vector representing finite impulse response filter
H	parity-check matrix
I	in-phase component

$I(X;Y)$	mutual information
L	link length
M	modulation order
N_0	noise power spectral-density
N_{span}	number of spans in the transmission line
P_{in}	power per channel at the input of span
P_{ch}	power per channel
P_{out}	power per channel at the output of span
PR	power ratio between inphase and quadrature components
Q	quadrature component
R	symbol rate
S	constellation rotational symmetry
t	time
T_S	symbol period
x	input
y	output

Introduction

In the past decades the Internet has evolved from a small network between research institutions to a global infrastructure. Internet applications have also evolved from simple services such as file-sharing and e-mail to network demanding ones such as video streaming, online gaming, machine-to-machine communication, etc. These new applications require ever-growing connection speeds. Furthermore, the number of network endpoints has increased from a few million in the 1990s to billions nowadays [1]. With the rise of the internet of things, the number of connected devices will soon reach tens of billions. To support the exponential growth of internet traffic, core networks with ever-increasing rates are necessary. Nowadays, core networks are based on fiber optic communications and the capacity and reach of these optical transport networks have been continuously increasing in the past decades thanks to several technologies: low-loss fibers, optical amplifiers, wavelength division multiplexing, polarization multiplexing, coherent detection, digital signal processing, advanced modulation formats, etc. Rates of 2.5 Gb/s per channel over transoceanic distances were possible in 1990, but since then rates have evolved achieving 100 Gb/s per channel in 2010. Additionally, the use of dense wavelength division multiplexing enables the transmission of around 100 channels in a single fiber resulting in capacities exceeding 10 Tb/s per fiber.

Nowadays, coherent detection in combination with digital signal processing is the *de facto* standard for long-haul high capacity optical communications systems operating at 100 Gb/s per channel and beyond. With the advent of high-speed high-

resolution digital-to-analog converters, generation of high order modulation formats with digital pulse shaping has become possible enabling the increase of both the rate per channel as well as the spectral efficiency. Furthermore, the widespread use of transmission links without in-line dispersion compensation allows elegant analytical optical channel modeling which facilitates the use of powerful tools from information theory and digital signal processing. In this thesis, these tools are applied to increase the rate per channel and spectral efficiency of long-haul optical communications systems. Concretely, the concepts investigated in this thesis are attractive for next-generation long-haul transponders operating at 400 Gb/s and 1 Tb/s.

This thesis is organized as follows. In Chapter 1 fundamental notions of digital communications, information theory and channel coding over the linear Gaussian channel are revisited. These notions will be later applied to optimize long-haul optical communications transmission systems. Also, the evolution of error correction codes used in long-haul optical communications systems is described. Finally, a short description of low density parity check (LDPC) codes and a novel class of codes called spatially coupled LDPC codes is provided.

Chapter 2 gives a general description of long-haul high-capacity communication systems. The following system blocks are described: the transmitter capable of arbitrarily modulating the 4-dimensional optical field, the optical channel including transmission effects and optical amplification, and the receiver based on coherent detection, polarization diversity, and digital signal processing. The main algorithms in the receiver signal processing are described in detail. Then, an equivalent channel model is described assuming that both amplifier noise and nonlinear interference can be modeled as additive white Gaussian noise for long-haul highly dispersive links. This greatly simplifies system design since it enables the use of the digital communications and information theory tools described in Chapter 1.

In Chapter 3, I investigate modulation format optimization for long-haul high-capacity communication systems building on the tools, models and algorithms described in Chapter 1 and 2. I focus on constellation optimization, multi-dimensional formats and time-interleaved hybrid formats. The four main contributions in this chapter are: the study of 8-ary quadrature amplitude modulation (QAM) formats, and the impact of constellation choice on carrier recovery algorithms; then, several 8QAM constellations are compared in terms of generalized mutual information that better predicts performance considering practical channel coding implementations; afterwards, two solutions providing 2.5 bits per symbol per polarization, the first one based on 4D-modulation and the second on time-interleaved hybrid modulation, are compared; finally, the use of 4D modulation in intensity modulation and direct

detection systems based on 4PAM is investigated. All these topics are complemented by experimental results that demonstrate the concepts investigated.

In Chapter 4, the design of next generation transponders based on high symbol rate signals operating at 400 Gb/s and 1 Tb/s is investigated. These high bitrate signals are attractive to reduce the cost per bit as more capacity can be integrated in a single transponder, however at such high symbol rates signals are less tolerant to several imperfections. To deal with one of these imperfections, namely the skew between sampling channels at the coherent receiver, I propose a modified blind equalizer tolerant to receiver skew even after long-haul transmission. Skew estimation is also investigated. Then, thanks to the development of advanced signal processing algorithms combined with state-of-the-art opto-electronic components, record high-capacity transmission experiments are demonstrated: the first single carrier 400 Gb/s transmission over transatlantic distance (at 6 b/s/Hz) and the first 1 Tb/s net data rate transmission based on the parallel synthesis of multiple spectral sub-bands (at 8 b/s/Hz).

Chapter 1. Digital communications

In this chapter, we review basic concepts of digital communications and channel coding over the linear Gaussian channel. Then, we briefly describe the evolution of error correction codes for long-haul optical communications systems. In Section 1.1, we deal with modulation, the process of converting an input sequence of symbols into a waveform suitable for transmission over a communication channel and demodulation, the corresponding process at the receiver of converting the received waveform in a sequence of received symbols. Additionally, we discuss pulse shaping that guarantees inter-symbol interference-free communication while limiting the bandwidth occupied by the transmitted signal. We also describe a received symbol discrete model that considers additive white Gaussian noise and matched filter receiver. Then, in Section 1.2, we discuss modulation formats choice (symbol alphabet) and bit labeling. We introduce useful tools to compare different modulation formats including: minimum Euclidean distance, symbol error rate, bit error rate, mutual information and generalized mutual information. Finally, in Section 1.3, channel coding basics are introduced with a focus on codes used in long-haul optical communications systems. We also give a short description of low density parity check (LDPC) codes and a novel class of codes called spatially coupled LDPC codes. Most of the concepts of Section 1.1 and Section 1.2 can be found in digital communications textbooks such as [2] or in review papers such as [3]. Then, concepts of Section 1.3 can be found in [4] (evolution of channel coding in general

from Shannon up to the present) and in [5], [6] (evolution of channel coding schemes for long-haul optical communications).

1.1. *Communications over the Gaussian channel*

The problem of converting an input symbol sequence into waveforms s(t) suitable for transmission can be written as:

$$s(t) = \sum_k x_k \, \psi_k(t) \tag{1.1}$$

where x_k are the discrete symbols we want to transmit over a channel and $\psi_k(t)$ are the basis waveforms. One example of a basis waveform is the set of delayed rectangle (gate) functions:

$$s(t) = \sum_k x_k \, rect\left({}^{t}/_{T_S} - kT_S\right) \tag{1.2}$$

where T_S is the symbol period and the rectangular function:

$$rect(t) = \begin{cases} 0, if \ |t| > 0.5 \\ 1, if \ |t| < 0.5 \\ 0.5, if \ |t| = 0.5 \end{cases} \tag{1.3}$$

However, the rectangle function occupies infinity bandwidth since the Fourier transform of the rectangle pulse is in the sinc function:

$$\mathcal{F}\big(rect(t)\big) = \frac{\sin(\pi f)}{\pi f} = sinc(\pi f) \tag{1.4}$$

To obtain a band-limited basis waveform, we can simply use the sinc pulse in the time-domain:

$$s(t) = \sum_k x_k \, sinc\left(\frac{\pi t}{T_s} - kT_S\right)$$

Now the maximum frequency of the signal *s(t)* is $\frac{1}{2T_S}$. Since the symbol period is T_S, the symbol rate *R* equals 1/T_S and the maximum signal frequency is *R*/2. The sinc basis function has also other interesting property: at particular instants the function $s(t)$ equals only one of sent symbol since $s(kT_s) = x_k$ for all k (integer). Therefore, at the receiver side, a simple receiver rule would be sampling the waveform at every instant kT_s to recover the sent data symbols in the noise-free scenario.

The sinc pulse has one drawback which is its long impulse response: the side lobes have high amplitudes that decrease slowly. However, if we accept a slightly higher spectral occupancy, we can use the raised-cosine pulse family. The frequency response of a raised-cosine pulse is:

$$H_{RC}(f) = \begin{cases} 1, if\ |f| < \dfrac{1-\beta}{2T_s} \\ 0, if\ |f| > \dfrac{1+\beta}{2T_s} \\ 0.5 + 0.5cos\left(\dfrac{\pi T_s}{\beta}\left(|f| - \dfrac{1-\beta}{2T_s}\right)\right), if \dfrac{1+\beta}{2T_s} > |f| > \dfrac{1-\beta}{2T_s} \end{cases} \quad (1.5)$$

where β is the roll-off factor $(0 \leq \beta \leq 1)$ and controls the trade-off between the occupied bandwidth and the amplitude of impulse response side lobes. We can simply obtain the impulse response of the raised-cosine pulse $h_{RC}(t) = \mathcal{F}^{-1}\big(H_{RC}(f)\big)$. We then write the sent signal as:

$$s(t) = \sum_k x_k\, h_{RC}(t - kT_S) \quad (1.6)$$

Then, the signal maximum frequency is $\frac{1+\beta}{2T_s}$ and the signal can be recovered by sampling *s(t)* every T_S. However, when the received signal *r(t)* is corrupted by additive white Gaussian noise (AWGN), the optimum receiver is known as the matched filter receiver. The received noise-corrupted signal can be written as:

$$r(t) = s(t) + n(t) = \sum_k x_k\, \psi_k(t) + n(t) \quad (1.7)$$

where n(t) is AWGN with power spectral density $N(f)=N_0/2$. Using a matched filter receiver, the received symbol is:

$$y_k = \int r(t)\psi_k(t)\, dt = x_k + w_k \quad (1.8)$$

where $\psi_k(t)$ is set of orthonormal waveforms. The discrete-time received sequence $y_k$contains noise estimates of the transmitted symbols x_k.The orthonormality of $\psi_k(t)$ ensures there is no intersymbol interference (ISI) and the noise sequence (w_k) is a set of independent and identically distributed Gaussian random noise variables with zero mean and variance $N_0/2$. To ensure orthonormality, the following requirement should be satisfied:

$$\int \psi_k(t)\psi_l(t)\, dt = \begin{cases} 1, if\ k = l \\ 0, if\ k \neq l \end{cases} \quad (1.9)$$

This can be achieved using the root-raised cosine pulse shape defined as

$$\psi_k(t) = h_{RRC}(t - kT_S) = \mathcal{F}^{-1}\left(\sqrt{\mathcal{F}\left(h_{RC}(t - kT_S)\right)}\right) \tag{1.10}$$

which is equivalent to solving:

$$\int \psi_k(t)\psi_l(t)\, dt = h_{RC}(t - kT_S) \tag{1.11}$$

The root-raised cosine pulse shape occupies the same amount of bandwidth as the raised cosine pulse shape. If baseband transmission is used, x_k is a real number (from a set of constellation points), however in passband transmission x_k can be represented as a complex number and the transmitted signal as:

$$s_{PB}(t) = \Re\left\{\sum_k x_k\, h_{RRC}(t - kT_S)e^{j2\pi f_0 t}\right\} \tag{1.12}$$

where f_0 is the carrier frequency. The receiver needs now an extra block before matched filter to perform down-conversion and low-pass filtering. Then the discrete-time transmission model can be synthesized as:

$$y_k = x_k + z_k \tag{1.13}$$

where x_k is still the transmitted symbol belonging to a finite alphabet (now a complex number), z_k is AWGN with variance $N_0/2$ per dimension (real and imaginary) and y_k is the received noise-corrupted symbol.

1.2. *Modulation formats*

Assuming this linear Gaussian channel model with pass-band transmission, now we focus on the choice of the alphabet. Fig. 1.1 shows six possible modulation formats: BPSK (binary phase shift keying), QPSK (quadrature phase shift keying), 8QAM (8-ary quadrature amplitude modulation), 16QAM, 32QAM and 64QAM containing 2, 4, 8, 16, 32 and 64 possible states, respectively. Defining M as the number of possible states (constellation order), the number of bits that can be transported per symbol period is simply $\log_2(M)$: 1, 2, 3, 4, 5 and 6, respectively.

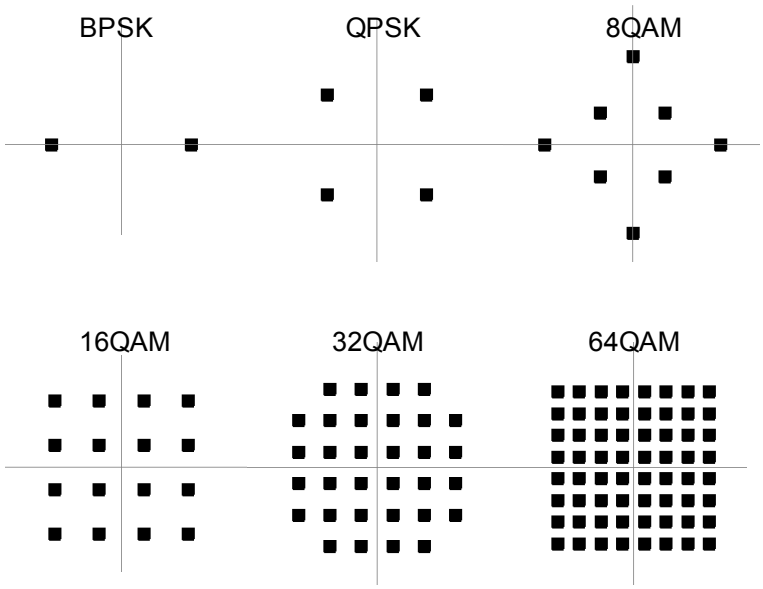

Fig. 1.1: Example of candidate modulation formats for transmission over a passband channel.

The choice of modulation formats can be done using several criteria. One of the most common criteria is the minimum Euclidean distance (d_{min}) defined as the shortest distance between two symbols in the alphabet. Ideally, we would like to maximize this distance to reduce probability of symbol errors when they are corrupted by noise. *Tab. 1.1* shows d_{min} for the formats depicted in Fig. 1.1, with symbol average energy normalized to one.

Format	d_{min}
BPSK	2
QPSK	1.41
8QAM	0.92
16QAM	0.63
32QAM	0.44
64QAM	0.31

Tab. 1.1: Minimum Euclidean distance (normalized to a constellation with unit average symbol energy)

For the tested formats, the higher is the constellation order, the lower is the minimum Euclidean distance. Furthermore, since we are mainly interested in binary communications, we must investigate the problem of how to map bits to symbols and vice-versa. Fig. 1.2 shows Gray bit-mappings for three real-valued alphabets (from top to bottom): BPSK, 4PAM (4-level pulse amplitude modulation) and 8PAM. Gray mapping ensures that neighbor symbols have only one bit difference. This is useful for transmission over noisy channels since the most common errors are the ones between neighbors, thus reducing the bit error rate compared to non-Gray bit-mapping. Additionally, these same mappings can be extended to complex-valued constellations. For example, two bits can define the mapping of the real component of the 16QAM constellation (equivalent of 4PAM) and the two remaining bits define the imaginary component. The same logic can be extended to QPSK (two parallel BPSK) and 64QAM (two parallel 8PAM). Note that it is not possible to use Gray mapping in the 8QAM and 32QAM constellations depicted in Fig. 1.1, however bit-to-symbol mappings that try to minimize the number of different bits between neighbors can be found usually using local search algorithms such as the *binary switching algorithm* [7].

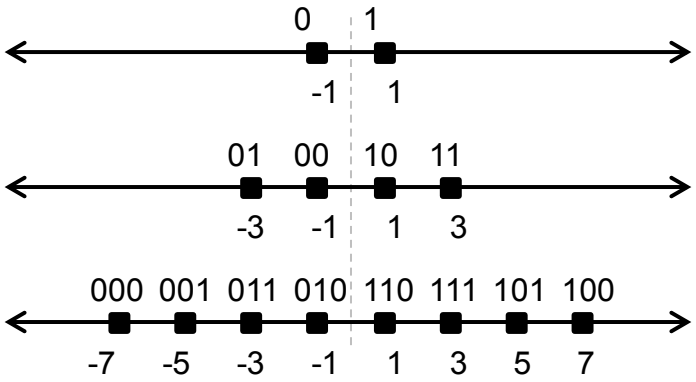

Fig. 1.2: Bit-to-symbol mapping (Gray) for BPSK, 4PAM and 8PAM.

1.2.1 Hard and soft decision

Now, assuming the discrete channel model defined in Eq. *1.13* and modulation formats as the ones defined in Fig. 1.1, we describe the theory of estimating the transmitted symbol after observing a noise-corrupted version of this symbol. The maximum likelihood (ML) symbol detector is:

$$\hat{x} = arg \max_{x} \; p_{Y|X}(y|x) \tag{1.14}$$

where x can take M values ($x^{(1)}, x^{(2)}, \dots, x^{(M)}$) for a constellation with M symbols. To simplify notation, we write $p_{Y|X}(y|x)$ as $p(y|x)$, $p_X(x)$ as $p(x)$ and so on for the rest of this thesis. Then, the probability density function of receiving *y* given *x* (using Eq. *1.13*) is:

$$p(y|x) = \frac{1}{\pi N_0} e^{\frac{-|y-x|^2}{N_0}} \tag{1.15}$$

Then, taking the log, which does not change the maximization, we obtain:

$$\hat{x} = arg\max_x \log\big(p(y|x)\big) = arg\min_x |y-x|^2 \tag{1.16}$$

This is also known as the minimum distance detector. So maximum likelihood hard-decision can be done by testing all possible symbols in the alphabet ($x^{(1)}, x^{(2)}, \dots, x^{(M)}$), and then choosing the one closest to the received signal. To reduce complexity, especially in the case of M-QAM formats, we can pre-calculate thresholds exploiting the structure of the alphabet. Afterwards, bits are obtained from symbols using a demapper (symbol-to-bit).

Note that if you have a priori knowledge of the distribution of sent symbols, we can alternatively maximize the probability of *x* given observation of *y*:

$$\hat{x} = arg\max_x\ p(x|y) = arg\max_x \frac{p(y|x)p(x)}{p(y)} = arg\max_x\ p(y|x)p(x) \tag{1.17}$$

Taking the log

$$\hat{x} = arg\max_x \log\big(p(x|y)\big) = arg\min_x \frac{|y-x|^2}{N_0} - \log\ p(x) \tag{1.18}$$

This is known as maximum a posteriori (MAP) detection. Note that MAP and ML detectors give the same result if the sent symbols are equiprobable (p(x) is constant for all values of x). This is typically the case for M-QAM formats, but can be different when using, for example, probabilistic shaping [3].

Alternatively, a receiver may be designed to exploit not only the most probable symbol but also the probabilities of every possible symbol [8]. This is known as soft-decision. Suppose we have a constellation with M symbols [$x^{(1)}, x^{(2)}, \dots, x^{(M)}$], a soft-decision maximum likelihood decoder would simply output the vector [$p(y|x^{(1)}), p(y|x^{(2)}), \dots, p(y|x^{(M)})$] (calculated from Eq. *1.15* if the channel is Gaussian). Alternatively, if we have a priori knowledge on the distribution of sent symbols, we can perform maximum a posteriori soft-decision and the output vector would be [$p(y|x^{(1)})p(x^{(1)}), p(y|x^{(2)})p(x^{(2)}), \dots, p(y|x^{(M)})p(x^{(M)})$].

If the alphabet is binary the output vector has only two values $p(y|x^{(1)})$ and $p(y|x^{(2)})$, therefore binary soft-decision decoders usually output the likelihood ratio:

$$LR(y) = \frac{p(y|x^{(1)})}{p(y|x^{(2)})} \tag{1.19}$$

or the log likelihood ratio to ensure numerical stability:

$$LLR(y) = \log\left(\frac{p(y|x^{(1)})}{p(y|x^{(2)})}\right) \tag{1.20}$$

Additionally, even when the constellation is not binary, bit-wise soft decoding can be performed. This is attractive to reduce decoding complexity and it is widely used in practical receivers. Assuming the constellation has $\log_2(M)$ bits ($b_1, b_2, \ldots, b_{\log2(M)}$). The bit-wise log likelihood ratio can be written as:

$$LLR(y, b_i) = \log\left(\frac{p(y|b_i = 0)}{p(y|b_i = 1)}\right) = \log\left(\frac{\sum_{m=1}^{M} p(y|x^{(m)})\alpha_{m,i}}{\sum_{m=1}^{M} p(y|x^{(m)})(1-\alpha_{m,i})}\right) \tag{1.21}$$

where $\alpha_{m,i}$ can take values 1 (if symbol b_i of symbol $x^{(m)}$ equals 0) or 0 (if symbol b_i of symbol $x^{(m)}$ equals 1).

1.2.2 Symbol and bit error probability

One of the most common metrics to compare different modulation formats is the symbol (resp. bit) error probability which gives the probability of the decided symbol (resp. bit) being different from the actual sent symbol (resp. bit). Given the constellation and the channel, the symbol error probability can be estimated using Monte Carlo simulation or calculated analytically for some constellations. If we also know the bit-to-symbol mapping, the bit error probability may also be estimated or calculated. Fig. 1.3 shows the Monte Carlo simulation of the bit error rate for the formats depicted in Fig. 1.1 (equiprobable sent symbols), using the Gaussian channel and hard-decision decoding based on maximum likelihood estimation. For BPSK and squared QAM formats, we used Gray bit mapping and for 8QAM and 32QAM the bit mappings proposed in [9], [10] respectively.

We observe that the higher the number of bits per symbol the higher is the required SNR to obtain a given BER, the well known trade-off spectral efficiency vs required SNR. In the optical communications community, due to historical reasons BER is usually converted to another performance metric called Q^2-factor. This metric is related to BER using the following formula and BER and Q^2-factor are used interchangeably for the rest of this thesis.

$$Q^2 factor = 20log_{10}\left[\sqrt{2} \cdot erfc^{-1}(2 \cdot BER)\right] \quad (1.22)$$

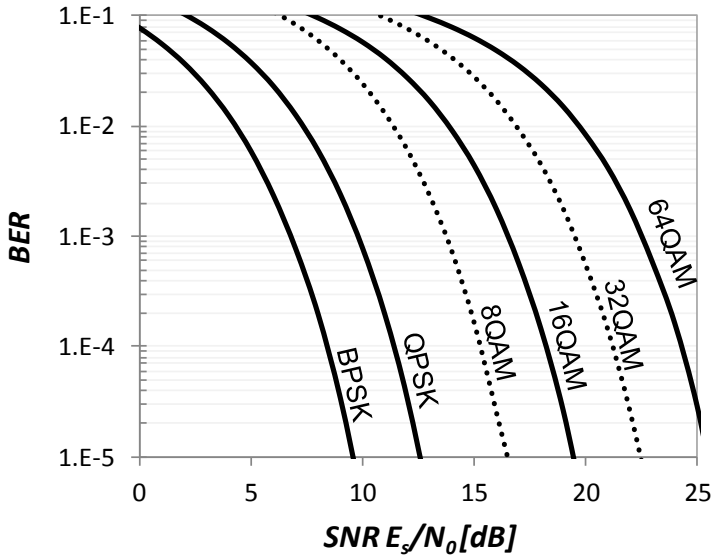

Fig. 1.3: Bit error rate for several constellations. Solid lines represent formats with Gray mapping and dashed lines formats without Gray mapping.

1.2.3 Mutual information

Another important metric when choosing the signal alphabet is the mutual information which quantifies the amount of information shared between two random variables. When these two variables represent the sent signal and the received signal (after transmission over a channel and eventually corrupted by noise), the mutual information gives the maximum amount of information that can be transported over the channel. Assuming two random variables: X representing the signal to be transmitted belonging to a finite set of points, and Y representing the received signal after the channel, the mutual information can be calculated as:

$$I(X;Y) = \iint p(x,y) \cdot log_2\left(\frac{p(x,y)}{p(x)p(y)}\right), \quad (1.23)$$

then using Bayes rule

$$I(X;Y) = \iint p(x,y) \cdot log_2\left(\frac{p(y|x)}{p(y)}\right) \quad (1.24)$$

where p(x) is the probability distribution of the sent signal: usually a discrete equiprobable distribution where each point belongs to a M point constellation with probability 1/M for each point. Then p(y) is the probability density function of the received symbol: usually the sent symbol distorted by the channel plus random noise. Finally p(x,y) is the joint probability between sent and received signals and

p(y|x) is the probability of observing y given transmission of x. Fig. 1.4 shows a simple schematic of an arbitrary channel defined by the conditional probability p(y|x), the amount of information that can be transported in this channel depends on this conditional probability as well as on the choice and distribution of the input symbols.

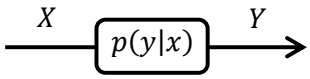

Fig. 1.4: General channel.

For a transmission over a Gaussian complex channel (see Fig. 1.5), Y corresponds to the received signal in the complex plane corrupted by noise in the form Y=X+Z, where Z has zero mean Gaussian distribution per dimension (in-phase Z_I and quadrature Z_Q) with variance $N_0/2$, with N_0 (noise power spectral density) being a function of SNR as $SNR=E_s/N_0$, and E_s is the average symbol energy ($\mathbb{E}(X^2)$).

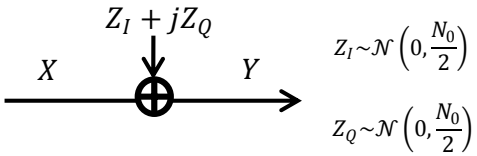

Fig. 1.5: Gaussian complex channel.

The conditional probability density function for the Gaussian channel is simply:

$$p(y|x) = \frac{1}{\pi N_0} e^{\frac{-|y-x|^2}{N_0}} \tag{1.25}$$

Furthermore, the mutual information can be estimated using Monte Carlo simulation as follows:

$$\begin{aligned} \hat{I}(X;Y) &= \lim_{K\to\infty} \left(\frac{1}{K} \sum_{k=1}^{K} log_2 \left(\frac{p(y_k|x_k)}{p(y_k)} \right) \right) \\ &= \left(\frac{1}{K} \sum_{k=1}^{K} log_2 \left(\frac{p(y_k|x_k)}{\sum_{m=1}^{M} p(y_k|x^{(m)}) p(x^{(m)})} \right) \right) \end{aligned} \tag{1.26}$$

where the sent signal can take M values $[x^{(1)}, x^{(2)}, \dots, x^{(M)}]$ with probabilities $[p(x^{(1)}), p(x^{(2)}), \dots, p(x^{(M)})]$. Additionally, K is the number of symbols in the Monte Carlo simulation, x_k is one random sample from the sent signal distribution. For the Gaussian channel, $y_k = x_k + z_k$ with z_k being one random sample of the normal distribution with variance $N_0/2$ per dimension. When K is sufficient large, the Monte Carlo simulation converges to the real mutual information.

Using the Monte Carlo method, Fig. 1.6 shows the mutual information as a function of the signal-to-noise ratio for the equiprobable QAM formats depicted in Fig. 1.1, also known as constellation constrained capacity. We included the Shannon limit ($\log_2(1+SNR)$) which defines the upperbound on mutual information over the Gaussian channel which can be achieved when the distribution of sent symbols is also Gaussian [11]. We observe that each curve saturates at $\log_2(M)$ and for low SNR, there is a negligible penalty compared to the Shannon limit coming from the usage of finite equipropable alphabet.

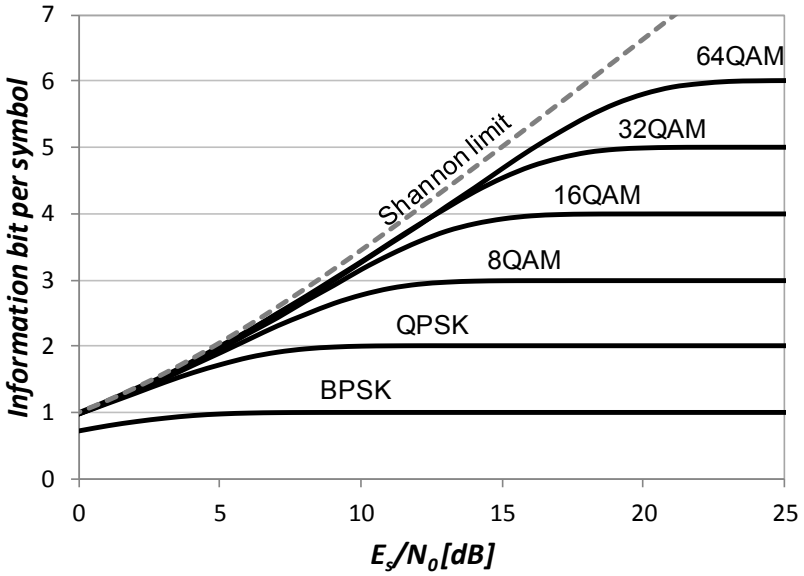

Fig. 1.6: Mutual information over the Gaussian channel for BPSK, QPSK and 8/16/32/64QAM.

The mutual information can also be calculated after performing hard-decision. Fig. 1.7 shows the schematic of the hard-decision Gaussian channel. After receiving y (corrupted by noise), we select $\hat{x}$ as the symbol from the alphabet that maximizes the probability density function of observing y (maximum likelihood detector). Now we have a new random variable $\hat{X}$ representing the distribution of symbols after decision. We can then calculate the mutual information $(X;\hat{X})$.

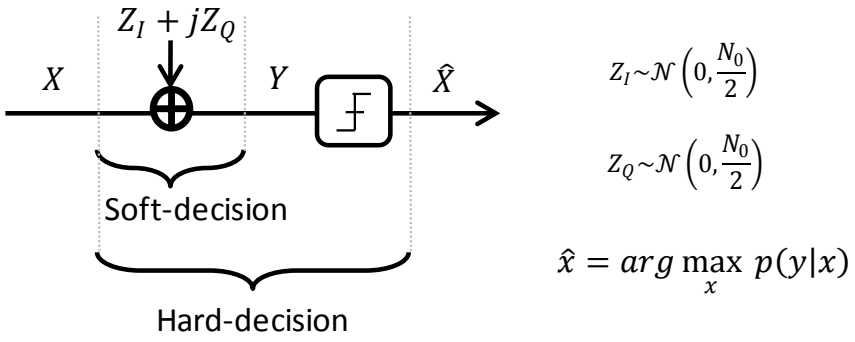

Fig. 1.7: Gaussian channel with hard-decision.

Then in Fig. 1.8, we show both $I(X;Y)$ (referred as soft-decision mutual information) and $I(X;\hat{X})$ (hard-decision mutual information) for QPSK modulation.

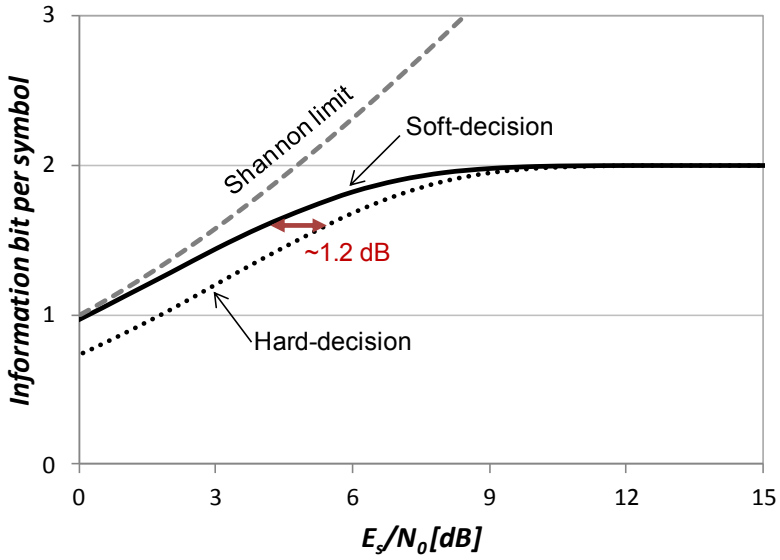

Fig. 1.8: Hard-decision vs. soft-decision for QPSK.

We observe that, performing hard-decision reduces the maximum achievable information rate, therefore systems designed to process *hard* information (decided symbols or bits) requires more power than systems that can take advantage of the *soft* information to achieve the same information rate. A general rule of thumb for maximizing performance can be expressed as: never make hard decisions, instead deliver to the next stage probabilities of possible decisions [8].

Furthermore, we can calculate the bit-wise mutual information, which is interesting to quantify the achievable information rate of multi-level modulation decoded with bit-wise soft-decision. Bit-wise decoding is attractive to reduce decoder complexity in practical receivers. The bit-wise mutual information is sometimes referred as generalized mutual information (GMI) or even BICM mutual information

(related to bit-interleaved coded modulation schemes). The generalized mutual information is simply:

$$GMI(X;Y) = \sum_{i=1}^{log_2 M} I(b_i;Y) \tag{1.27}$$

where for each bit b_i we calculate the shared information between the received signal and the transmitted bit, followed by a sum over all $\log_2(M)$ bits. Compared to mutual information, there is a loss of information since the generalized mutual information can be developed as:

$$GMI(X;Y) = I(b_1;Y) + I(b_2;Y) + \cdots + I\left(b_{log_2 M};Y\right) \tag{1.28}$$

and the mutual information as

$$I(X;Y) = I(b_1;Y) + I(b_2;Y|b_1) + \cdots + I\left(b_{log_2 M};Y|b_1, b_2 \ldots b_{log_2 M-1}\right) \tag{1.29}$$

And since the following inequalities hold:

$$I(b_2;Y) \leq I(b_2;Y|b_1) \tag{1.30}$$

$$I\left(b_{log_2 M};Y\right) \leq I\left(b_{log_2 M};Y|b_1, b_2 \ldots b_{log_2 M-1}\right) \tag{1.31}$$

then it is clear that:

$$GMI(X;Y) \leq I(X;Y) \tag{1.32}$$

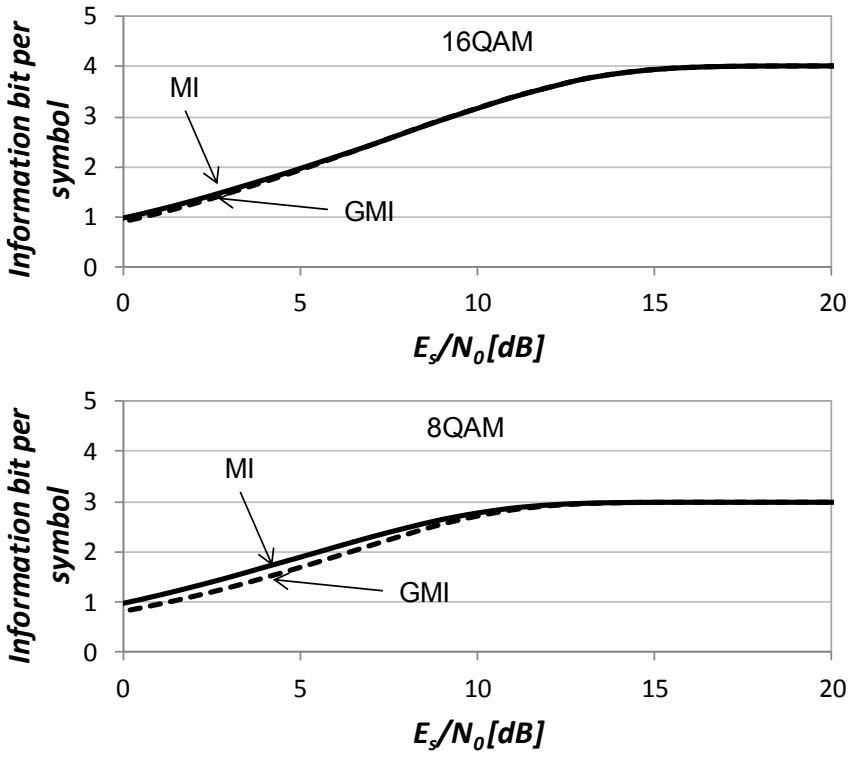

Fig. 1.9: Mutual information (MI) vs. generalized mutual information (GMI) for 8QAM and 16QAM.

In summary, performing bit-wise soft-decision reduces the mutual information available at the decoder which results in lower achievable information rate. To observe the information rate loss due to bit-wise processing, Fig. 1.9 depicts the comparison between mutual information and generalized mutual information for two formats: 8QAM and 16QAM. We observe that when using 8QAM, there is a higher loss of information compared to 16QAM. This comes from the difference in mapping between the formats. Gray mapping (such as the one of 16QAM) is known to maximize the GMI over the Gaussian channel and there is a small loss coming from bit-wise processing for 16QAM. On the other hand, the bit-wise processing of 8QAM without Gray mapping results in higher penalty coming from the non-Gray mapping.

1.3. *Channel coding*

The mutual information defines an upper bound on information rate for a given channel using a specific symbol alphabet, however it does not tell us how to achieve this upper bound. This is the goal of channel coding also known as forward error correction (FEC). Channel coding is based on adding redundant information to a bit sequence. At the receiver, after transmission over a noisy channel, the receiver

decoder exploits redundancy to try to recover the sent data. For block codes, we send a codeword of N bits, where K bits represent the data and the remaining N-K bits the redundancy. The amount of redundancy can be quantified by two metrics: the code rate or the overhead. The code rate is defined as:

$$r = \frac{K}{N} \tag{1.33}$$

and the overhead as:

$$OH = \frac{100(N-K)}{K}\ [\%] \tag{1.34}$$

Note that K and N may also represent number of symbols for non-binary codes. For example, the first error correcting code to have achieved widespread use in optical communications systems was the Reed-Solomon code [12] named RS(255,239), with N=255 and K=239 resulting in overhead of 6.7%. These codes used non-binary symbols from an alphabet of length 256 (2^8), therefore after conversion to bits we find that each codeword has a total length of 2040 bits. The RS(255,239) code can correct up to 8 symbol errors and was very popular due to its low implementation complexity based on hard-decision decoding.

With the increase of computational power reserved to channel coding, more powerful codes based on longer blocks and product code concatenation gained a lot of attention. The main idea of concatenated product codes [13], [14] is the use of two low complexity component codes and an interleaver to achieve very long codewords which can then be decoded with reasonable complexity. The sequence of data bits is first encoded by a simple component code and then several coded blocks are interleaved before being encoded by another simple component code. The decoding is usually done iteratively, where each component code is decoded alternately and after each iteration performance improves until saturation. Most of the codes defined in ITU G.975.1 (specification of error correction codes for optical communications [15]) are based on concatenated product codes and typical block length is around 500.000 bits with overhead around 7% and hard-decision. One popular implementation is the one defined in Appendix I.9 of G.975.1 where each component code is a BCH code. This code has a pre-FEC BER threshold of $3.8 \cdot 10^{-3}$ to obtain a post-FEC BER below 10^{-15}.

With the advent of coherent detection and high resolution analog-to-digital converters, soft-decision has become attractive to provide even better performance compared to the previously mentioned codes based on hard-decision. For example,

low density parity check (LDPC) codes belong to a class of block codes first proposed by Gallager [16] which when paired with soft-decision iterative decoding can provide performance very close to the Shannon limit of the Gaussian channel. One undesired property of LDPC codes is the error floor: the fact that beyond a given SNR, the BER does not drop as rapidly as in the waterfall region. To tackle this problem, soft-decision LPDC are often used as an inner code to reduce the BER to a level usually between 10^{-3} and 10^{-5}, followed by a small overhead hard-decision code to further reduce the BER to a level typically below 10^{-15}. The use of LDPC with overhead around 20% became very popular for ultra-long-haul optical communication systems and it is currently used in commercial products. However, there is still room for improvement and a straightforward way to further increase channel coding performance of block codes is to increase the block size. Unfortunately, a block length beyond 30000 bits becomes very challenging for real-time applications at bitrates beyond 100 Gb/s (typical in long-haul optical communication systems). Nevertheless, a new class of codes referred as spatially coupled (SC-) LDPC can enable virtually arbitrarily long codewords that can be decoded with a simple decoder. Although this class of codes was introduced more than a decade ago, their outstanding properties have only been fully realized a few years ago, when Lentmaier et al. noticed that the estimated decoding performance of a certain class of terminated LDPC convolutional codes with a simple message passing decoder is close to the optimal *MAP* threshold of the underlying code ensemble [17]. Additionally, these codes have outstanding performance in the error floor region [18]. In this thesis, the outstanding performance of spatially-coupled LDPC codes has been used to obtain extra performance gain in record ultra-long-haul experiments (Chapter 4). In next section, we briefly describe LDPC codes and the spatially-coupled LDPC codes. For a exhaustive description of these codes, please refer to [17], [19], [5].

1.3.1 Low density parity check codes

To introduce low-density parity check codes, we start with a toy example. We use the Hamming code (7,4) which is a short block code as an example [20]. This code is defined by the generator matrix:

$$\mathbf{G} = \begin{bmatrix} 1 & 0 & 0 & 0 & 1 & 1 & 0 \\ 0 & 1 & 0 & 0 & 1 & 0 & 1 \\ 0 & 0 & 1 & 0 & 0 & 1 & 1 \\ 0 & 0 & 0 & 1 & 1 & 1 & 1 \end{bmatrix} \tag{1.35}$$

To generate the 7-bit long code word $\mathbf{x}=[x_0,x_1,x_2,x_3,x_4,x_5,x_6]$ from 4 data bits $\mathbf{d}=[d_0,d_1,d_2,d_3]$ we simply perform matrix multiplication using binary logic:

$$\mathbf{x} = \mathbf{dG} \tag{1.36}$$

This encoder structure defines three parity check equations also based on binary logic:

$$x_0 + x_1 + x_3 + x_4 = 0 \tag{1.37}$$

$$x_0 + x_2 + x_3 + x_5 = 0 \tag{1.38}$$

$$x_1 + x_2 + x_3 + x_6 = 0 \tag{1.39}$$

This set of equations can be synthesized in matrix notation:

$$\mathbf{H}\mathbf{x}^T = \mathbf{0} \tag{1.40}$$

$$\begin{bmatrix} 1 & 1 & 0 & 1 & 1 & 0 & 0 \\ 1 & 0 & 1 & 1 & 0 & 1 & 0 \\ 0 & 1 & 1 & 1 & 0 & 0 & 1 \end{bmatrix} \mathbf{x}^T = \begin{bmatrix} 0 \\ 0 \\ 0 \end{bmatrix} \tag{1.41}$$

where **H** is the parity check matrix. In this particular case, the percentage of "1"s in the matrix is around 62%, however for LDPC codes this percentage is much lower (usually below 1%) so we refer to these parity check matrices as *low-density*. Additionally, in practical codes the block length is much longer (usually beyond 1000 bits). Nevertheless, this toy example is useful to understand some key concepts of LDPC codes. These codes are usually described by their variable node degree and check node degree. The number of "1"s per row defines the check node degree which in our example is 4. Then, the number of "1"s per column defines the variable node degree which in our example is not constant, so we use instead the variable node degree profile. The degree profile indicates the percentage of nodes of certain degree. The Hamming exemplary code has variable node degree profile: 3/7 of columns have degree 1, 3/7 degree 2 and 1/7 degree 3. Codes with both constant check node degree and constant variable node degree are called *regular*. On the other hand, codes with non-constant variable node degree and/or non-constant check node degree are called *irregular* LDPC. The Hamming code example is irregular.

At the receiver, we have a noisy observation of the code word:

$$\mathbf{y} = \mathbf{x} + \mathbf{n} = \mathbf{dG} + \mathbf{n} \tag{1.42}$$

where $\mathbf{n}=[n_0,n_1,\ldots,n_{N-1}]^T$ is a vector of complex zero mean Gaussian independent noise. An optimal maximum a posteriori (MAP) decoder selects the estimated code word that maximizes the probability:

$$\hat{\mathbf{x}}_{MAP} = arg\max_{\mathbf{x}} p(\mathbf{x}|\mathbf{y}) = arg\max_{\mathbf{x}} p(\mathbf{y}|\mathbf{x})\, p(\mathbf{x}) \tag{1.43}$$

Since we suppose each code word is equiprobable, we can simply maximize the likelihood and obtain the maximum likelihood (ML) estimator:

$$\hat{\mathbf{x}}_{ML} = arg\max_{\mathbf{x}} p(\mathbf{y}|\mathbf{x}) \tag{1.44}$$

For long codewords, MAP and ML estimation are intractable problems, so practical LDPC use sub-optimal decoding with reasonable complexity which exploits the underlying structure of LDPC codes (sparse graph [21]). LDPC decoding is usually based on belief propagation (also known as sum-product algorithm [22], [23]). This algorithm performs exact inference on loop-free graphs (trees) by calculating marginal distribution of unobserved nodes (data in the case of channel coding). However, LDPC codes graph structure is not free of loops (acyclic) so belief propagation does not perform exact inference and it is suboptimal. Belief propagation in graphs with loops is also known as “loopy” belief propagation and iterations are used until the algorithm converges. Nevertheless, the performance penalty of LDPC decoding under belief propagation can be very low and LDPC codes are very popular and are present in several standards.

1.3.2 Spatially coupled LDPC

One goal of spatially-coupled LDPC codes, is to provide very long codewords. This is done simply by connecting neighboring blocks. For example, if we want to couple every block of the Hamming code (7,4) without changing the degree distribution, we could simply rewrite the parity check equations as:

$$x_0^{(i)} + x_1^{(i-1)} + x_3^{(i)} + x_4^{(i)} = 0 \tag{1.45}$$

$$x_0^{(i)} + x_2^{(i)} + x_3^{(i-1)} + x_5^{(i)} = 0 \tag{1.46}$$

$$x_1^{(i)} + x_2^{(i)} + x_3^{(i)} + x_6^{(i-1)} = 0 \tag{1.47}$$

We define the exponent i as the block number, and now for each parity equation we included one variable that depends on the previous block (i-1). So now we decompose the parity check matrix in two sub-matrices:

$$\mathbf{H}_0 = \begin{bmatrix} 1 & 0 & 0 & 1 & 1 & 0 & 0 \\ 1 & 0 & 1 & 0 & 0 & 1 & 0 \\ 0 & 1 & 1 & 1 & 0 & 0 & 0 \end{bmatrix} \tag{1.48}$$

$$\mathbf{H}_1 = \begin{bmatrix} 0 & 1 & 0 & 0 & 0 & 0 & 0 \\ 0 & 0 & 0 & 1 & 0 & 0 & 0 \\ 0 & 0 & 0 & 0 & 0 & 0 & 1 \end{bmatrix} \tag{1.49}$$

And the previous $\mathbf{H}$ parity check matrix for the uncoupled case is simply $\mathbf{H}_0 + \mathbf{H}_1$. The number of previous blocks connected defines one design parameter referred as *syndrome former memory*, which here is 1. Here we showed a deterministic connection between blocks, however these constructions are difficult to analyze so random connection has also been proposed [19]. Now the equivalent parity check matrix of the infinitely long spatially coupled code is:

$$\mathbf{H}_{SC} = \begin{bmatrix} \ddots & & & & & & \\ \ddots & \mathbf{H}_0 & & & & & \\ & \mathbf{H}_1 & \mathbf{H}_0 & & & & \\ & & \mathbf{H}_1 & \mathbf{H}_0 & & & \\ & & & \mathbf{H}_1 & \ddots & & \\ & & & & \ddots & & \end{bmatrix} \tag{1.50}$$

If we now count the number of “1”s and per row and per column, we obtain the same degrees as the underlying code. However, this infinitely long code is not practical and we need to terminate it. There are two options for termination. The first one referred as *tail-biting* which preserves the check and variable node degree:

$$\mathbf{H}_{SC}^{[TB]} = \begin{bmatrix} \mathbf{H}_1 & \mathbf{H}_0 & & & & \\ & \mathbf{H}_1 & \mathbf{H}_0 & & & \\ & & \mathbf{H}_1 & \mathbf{H}_0 & & \\ & & & \mathbf{H}_1 & \mathbf{H}_0 & \\ \mathbf{H}_0 & & & & \mathbf{H}_1 & \end{bmatrix} \tag{1.51}$$

The second one is *terminated*, as follows:

$$\mathbf{H}_{SC}^{[Ter]} = \begin{bmatrix} \mathbf{H}_0 & & & & & \\ \mathbf{H}_1 & \mathbf{H}_0 & & & & \\ & \mathbf{H}_1 & \mathbf{H}_0 & & & \\ & & \mathbf{H}_1 & \mathbf{H}_0 & & \\ & & & \mathbf{H}_1 & \mathbf{H}_0 & \\ & & & & \mathbf{H}_1 & \end{bmatrix} \tag{1.52}$$

One potential disadvantage of the *terminated* approach is the fact that it has one extra row compared to the tail-biting method which causes rate loss (higher overhead). However, if we increase the sub-matrix repetition (make the equivalent matrix very large) the rate loss becomes smaller. This small extra overhead can also be attractive since, the extra parity bits are present on the codeword edges. Therefore, the edge bits are more protected than the center bits so when we start the

iterative decoding, the first bits to be decoded are the ones in the edge and the information propagates to the central bits (decoding wave). Furthermore, since the decoding happens only close to this wave we can design simple decoders referred here as windowed decoders [24], [25]. The windowed decoder has a window size that defines how many sub-blocks it is decoding. For example, assuming the terminated example, the total parity check equation is written as:

$$\mathbf{H}_{SC}^{[Ter]}\mathbf{x}^T = \begin{bmatrix} \mathbf{H}_0 & & & & & \\ \mathbf{H}_1 & \mathbf{H}_0 & & & & \\ & \mathbf{H}_1 & \mathbf{H}_0 & & & \\ & & \mathbf{H}_1 & \mathbf{H}_0 & & \\ & & & \mathbf{H}_1 & \mathbf{H}_0 & \\ & & & & \mathbf{H}_1 & \end{bmatrix} \begin{bmatrix} \mathbf{x}^{(0)} \\ \mathbf{x}^{(1)} \\ \mathbf{x}^{(2)} \\ \mathbf{x}^{(3)} \\ \mathbf{x}^{(4)} \end{bmatrix} = \mathbf{0} \tag{1.53}$$

where $\mathbf{x}^{(i)}$ are the codewords for each block i. Without windowed decoder, decoding would be performed over the whole matrix $\mathbf{H}_{SC}^{[Ter]}$. However, reduced complexity can be achieved by exploiting the sub-matrix repetition structure and the decoding wave behavior (from the edges to the center). Therefore, a windowed decoder would start with decoding some blocks in the edge (number of blocks related to the window size), and then as edge blocks are decoded the window slides toward the matrix center. This technique of terminated SC-LDPC with windowed decoder will be used in Chapters 3 and 4 as a code of choice in transmission experiments.

1.3.3 Net coding gain

To compare different codes in transmission systems, the most useful performance metric is the net coding gain. This metric tells what is the difference (in dB) of required signal to noise ratio (SNR) between coded transmission compared to uncoded transmission while accounting for the extra overhead to achieve a given performance. For example, if we use uncoded QPSK and the target performance BER equals to 10^{-15}, we know that the required SNR is 18 dB. Let us assume that we have an arbitrary binary code where 50% of the codeword is reserved for redundancy bits (code rate equals to 0.5) and we measure 10 dB as the required SNR to achieve 10^{-15} BER after decoding. Then, the coding gain at 10^{-15} BER is simply 8 dB (18 dB – 10 dB). However remember that to transmit the same amount of information with the coded transmission, we need to increase its symbol rate by 100% (3 dB). So accounting for this extra required power to increase the symbol rate, we obtain the net coding gain at 10^{-15} BER of 5 dB (8 dB – 3 dB). In this example, the SNR threshold is 10 dB equivalent to a pre-FEC BER of $7 \cdot 10^{-4}$ or Q^2-factor threshold of 10 dB that ensures post-FEC performance below 10^{-15}.

For binary codes, an upper bound of the maximum net coding gain can be calculated as a function of the code rate as follows:

$$NCG_{max}(r, BER_{thr}) = \underbrace{SNR_{BER=BER_{thr}}[dB]}_{\substack{\text{required SNR} \\ \text{for BER=BER}_{\text{thr}}}} - \underbrace{SNR_{I(X;Y)=r}[dB]}_{\substack{\text{required SNR for} \\ \text{mut.inf.=r}}} + \underbrace{10\log_{10} r}_{\substack{\text{acounting for reduction} \\ \text{in information rate}}} \quad (1.54)$$

Therefore, we can calculate the net coding gain upper bound for two decoding approaches: hard-decision ($I(X;\hat{X})$) and soft-decision ($I(X;Y)$). Table 1.2 summarizes required SNR values as well as maximum net coding gains for hard-decision and soft-decision.

r	OH	$SNR_{BER=10^{-15}}$	$SNR_{(X;\hat{X})=r}$	$SNR_{I(X;Y)=r}$	$10\,log_{10}\,r$	NCG_{max} Hard-dec.	NCG_{max} Soft-dec.
0.934	7%	18 dB	7.6 dB	6.5 dB	-0.3 dB	10.1 dB	11.2 dB
0.833	20%	18 dB	5.9 dB	4.6 dB	-0.79 dB	11.31 dB	12.61 dB
0.8	25%	18 dB	5.4 dB	4.1 dB	-0.96 dB	11.64 dB	12.94 dB
0.5	100%	18 dB	1.8 dB	0.2 dB	-3 dB	13.2 dB	14.8 dB

Tab. 1.2: Symbol rates with corresponding FEC overheads and Q² thresholds

Fig. 1.10 depicts the net coding gain (NCG) as a function of the overhead for binary codes. Solid and dashed lines represent the maximum net coding gain of an ideal soft-decision (SD) and hard-decision (HD) error correcting codes respectively. We also show NCG of implementations of several codes employed in long-haul optical communications. The first generation based on 7% hard-decision FEC is represented by squares. Empty square represents the first code to achieve widespread use in optical communications due to its very low implementation complexity: RS(255,259) with around 6.2 dB of NCG. Then, with the same overhead, the filled square represents the concatenated hard-decision 7% code in the ITU standard [15] (Appendix I.9). At around 9 dB of NCG, this FEC is present in many commercial products thanks to its high coding gain with reasonable decoding complexity. Subsequently, the next generation of codes exploited the soft information available at coherent receivers and 20% SD-FEC were introduced and are now present in commercial long-haul high performance applications. One example of

these new soft-decision codes based on LDPC is represented by a circle [26] with around 11 dB of NCG. There is still room to reduce the gap to the limit and achieve higher NCG by increasing the overhead and/or using more powerful codes such as ones based on spatial coupling. This family of codes has very interesting properties (described in previous paragraphs). For example, 25% SD-FEC based on SC-LDPC [27] has around 1dB advantage over 20% LDPC-based SD-FEC as depicted in the figure (diamond) and it is closer to the SD-NCG limit. Those codes based on spatial coupling are attractive candidates to boost performance of next-generation optical communications systems.

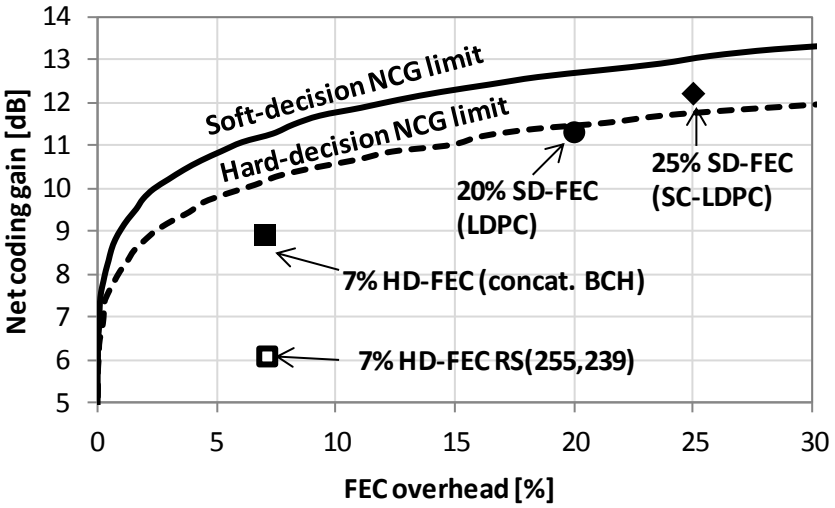

Fig. 1.10: Net coding gain at 10^{-15} BER.

1.4. ***Summary***

In this chapter we reviewed basic concepts of digital communications and channel coding and we introduced some tools that will be used in the next chapters: pulse shaping, modulation formats, (generalized) mutual information, FEC overhead, etc. In Chapter 2, we describe the optical communications systems based on coherent detection and we show that its equivalent channel model can be well approximated by the Gaussian channel model, therefore all the tools presented here can be applied to optimize its performance.

In this chapter, we also reviewed the evolution of error correction codes for optical communications. We focused and we briefly described the concept of spatially-coupled LDPC codes. Again, a more detailed description of this class of

codes can be found in [5], [17], [19]. SC-LDPC codes will be used in several experiments described in Chapters 3 and 4.

Chapter 2. Coherent optical communications

This chapter deals with several aspects of long-haul transmission systems based on wavelength division multiplexing and coherent detection. Coherent detection in combination with digital signal processing recently became the *de facto* standard for long-haul high capacity systems. Not only a coherent receiver has better sensitivity than a quadratic receiver, but also when in combination with high resolution analog-to-digital converters it is capable to reconstruct in the digital domain (with high fidelity) the optical field at the receiver. Hence, this enabled the use of signal processing algorithms to compensate fiber transmission linear impairments and to mitigate nonlinear impairments as well as fully exploit the four dimensions of the optical field (in-phase and quadrature of two orthogonal polarizations). Additionally, the introduction of high resolution high speed digital-to-analog converters at the transmitter gave designers a whole new degree of freedom. Now it is possible to modulate the 4-dimensional optical field with an arbitrary waveform in an optical bandwidth beyond 50 GHz. For example, the transmitted signal can now be shaped using digital filters resulting in increased spectral utilization through Nyquist pulse shaping. We can also use the arbitrary waveform functionality to adapt the modulation format for each transmission scenario using arbitrary constellations resulting in optimized performance. Finally, with the exponential increase of number of transistors in an integrated circuit, we have more and more available computational power to be used in signal processing algorithms and channel coding implementations resulting in several possibilities for performance increase.

This chapter is divided into 5 sections. First, Section 2.1 gives a general description of the three main blocks of long-haul high-capacity communication systems: transmitter, channel and receiver. In Section 2.2, we focus on modeling the optical channel in the linear regime. Fiber attenuation, amplifier additive noise, chromatic dispersion and polarization dependent effects are described. Next, in Section 2.3, receiver signal processing algorithms that mitigate linear impairments are detailed. In Section 2.4, we include non-linear effects in the model assuming that non-linear interference can be approximated as excess additive Gaussian noise. Finally, in the last section we summarize the chapter main concepts.

2.1. *System overview*

Fig. 2.1 shows a typical long-haul optical communication system with optical amplification and wavelength division multiplexing (WDM). In WDM, the light emitted by multiple (N_{ch}) laser sources at different wavelengths (λ_n) are modulated independently and simultaneously propagated over the same fiber. Therefore, we have N_{ch} independent transmitters (TX) which can be referred as channels. The signals coming from each transmitter are then combined using a multiplexer (MUX) before transmission. The transmission link is made of N_{span} spans of single mode fiber (SMF) separated by optical amplifiers that compensate for span loss. Erbium doped fiber amplifiers [28] (EDFA) operating on the C-band are the most widely used optical amplifiers. A typical C-band EDFA amplifier bandwidth is around 32 nm (centered at 1545 nm), therefore roughly 80 channels can be simultaneously amplified by a single EDFA considering 50 GHz channel spacing. After transmission, channels are separated by a demultiplexer before being detected by N_{ch} coherent receivers.

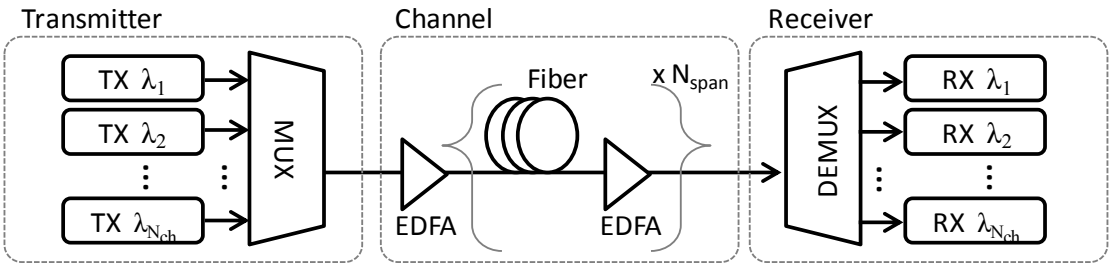

Fig. 2.1: Three main communication systems components: transmitter, channel and receiver.

To maximize the spectral efficiency, all physical dimensions available must be exploited by each transmitter. The main function of an optical transmitter is to convert an electrical signal into the optical domain. Here, we focus on transmitters that can independently modulate the amplitude and phase of the two optical polarizations of

the optical field over a large electrical bandwidth. For long-haul applications, this is typically achieved by cascading a laser source with Mach-Zehnder modulators (MZM) and a polarization beam combiner (PBC) as shown in Fig. 2.2.

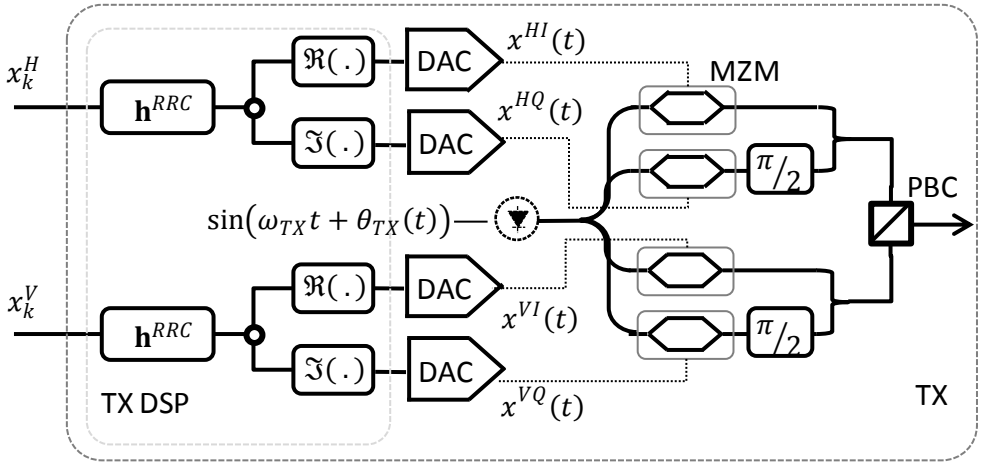

Fig. 2.2: Transmitter modulated in-phase and quadrature component of two orthogonal polarizations based on Mach-Zehnder modulator (MZM).

The goal of the optical transmitter is to transmit at every instant *k*, two complex symbols x_k^H and x_k^V in the horizontal and vertical polarizations, respectively. The electrical waveforms containing data to be transmitted are generated by four synchronized digital-to-analog converters (DAC). At the output of each DAC, we have 4 electrical waveforms:

$$x^{HI}(t) = \sum_{k=-\infty}^{\infty} \Re(x_k^H) h^{RRC}(t - k/R) \tag{2.1}$$

$$x^{HQ}(t) = \sum_{k=-\infty}^{\infty} \Im(x_k^H) h^{RRC}(t - k/R) \tag{2.2}$$

$$x^{VI}(t) = \sum_{k=-\infty}^{\infty} \Re(x_k^V) h^{RRC}(t - k/R) \tag{2.3}$$

$$x^{VQ}(t) = \sum_{k=-\infty}^{\infty} \Im(x_k^V) h^{RRC}(t - k/R) \tag{2.4}$$

where $h^{RRC}(t)$ is the impulse response of the root-raised cosine filter and R is the symbol rate. Roll-off factor of RRC filters and the symbol rate define the signal occupied bandwidth. To modulate each polarization, we use external modulators with a nested structure, comprising two MZM in parallel with π/2 shift between their outputs. The light from the laser with central frequency $f_{TX}=\omega_{TX}/2\pi$ is first split in two copies. Each copy is sent into a distinct modulator driven with different electrical data. Finally, a PBC recombines the output of both modulators onto two polarizations

of the polarization division multiplexed channel. Then the WDM multiplex, comprising N_{ch} channels is amplified before being transmitted. The channel spacing choice depends on several parameters: the channel occupied bandwidth, the precision of the central frequency of the signal carrier, etc. We can obtain the information spectral efficiency as the ratio between the bitrate per channel and channel spacing. Typical channel spacing is 50 GHz, but a finer granularity grid of multiples of 12.5 GHz become increasingly popular to provide better flexibility to optimize spectral efficiency.

2.2. *Linear model*

In this section, the principal transmission linear impairments for long-haul transmissions are briefly described and modeled. Here we discuss fiber attenuation, impact of amplifier noise in signal-to-noise ratio, chromatic dispersion and polarization mode dispersion.

Fiber attenuation is one of the main impairments limiting optical communication systems. When an optical signal propagates through an optical fiber its power is attenuated due to absorption and scattering loss. The power at the output of a fiber span (P_{out} [dBm]) as a function of the input power (P_{in} [dBm]) can be simply written as:

$$P_{out} = P_{in} - L\,\alpha \tag{2.5}$$

where *L* is the span length typically in [km] and α is the fiber attenuation typically in [dB/km]. The attenuation suffered by the propagating signal depends on the wavelength. The C-band (around 1550 nm) is the fiber window where the minimum of attenuation is located. The attenuation value in the C-band is usually around 0.2 dB/km for standard fibers, and can be as low as 0.148 dB/km for enhanced fibers.

To compensate for span loss, long-haul optical systems incorporate periodic optical amplifiers. C-band Erbium doped fiber amplifiers are the most widely used nowadays as they operate in the lowest fiber attenuation window. These amplifiers amplify the weak input signal from the previous span and launch it again into the next span at high power. However, EDFAs also introduce additive noise through amplified spontaneous emission (ASE) which degrades the optical signal-to-noise ratio (OSNR). The OSNR is defined as the ratio between the power of the signal and the power of the noise in a reference bandwidth, i.e. 12.5 GHz. The OSNR degradation can be measured by the amplifier noise factor (*F*) which is the linear ratio between the linear SNR at the input (SNR_{in}) and at the output (SNR_{out}) of the amplifier. The noise factor can be written as [29]:

$$F = \frac{SNR_{in}}{SNR_{out}} \tag{2.6}$$

The noise factor is usually expressed in [dB] and it is then referred as noise figure (NF) given by $10 \cdot \log_{10}(F)$. In practice, C-band EDFAs have a NF between 4 and 6 dB and have an output power as high as 20 dBm.

Assuming a homogeneous transmission link with N_{span} spans, L km of fiber per span and fiber attenuation α, we can quantify the impact of the ASE noise into the OSNR after transmission [30]. Considering large span loss, P_{in} defined as the channel power at the input of each span (amplifier output) in [dBm], and P_{out} defined as the channel power at the span output also in [dBm], we can use the following formula that approximates the OSNR in [dB]:

$$\begin{aligned} OSNR &\approx 10\log_{10}\left(\frac{P_{out}}{Fhf_0B_{ref}N_{span}}\right) = \\ &= P_{in} - L \cdot \alpha - NF - 10\log_{10} hf_0B_{ref} - 10\log_{10} N_{span} \end{aligned} \tag{2.7}$$

where B_{ref} is the reference bandwidth, f_0 is the signal frequency (around 193.95 THz corresponding to C-band) and h is the Planck constant. We observe that the OSNR decreases logarithmically with the number of spans (distance). In contrast, we can improve the OSNR by reducing span loss (i.e. fiber with lower attenuation), by reducing amplifier noise figure or by increasing the channel launch power at the input of the span (P_{in}). However, as we will see in Section 2.4, nonlinear impairments increase with amplifiers output power so this power cannot be indefinitely increased.

Another fiber linear impairment is chromatic dispersion which refers to the wavelength dependency of the fiber refractive index. This generates pulse broadening in the time domain, thus inducing inter-symbol interference. From a fiber optic transmission system point of view, we can model the chromatic dispersion by the dispersion factor D expressed in [ps/(nm·km)][31]. The dispersion factor represents the differential group delay between two spectral lines separated by 1 nm after 1 km transmission. This factor depends on the wavelength λ:

$$D = -\frac{2\pi c}{\lambda^2}\beta_2 \tag{2.8}$$

where c is the speed of light. The dispersion D is related to β_2 which is the second derivative of the propagation constant and is commonly referred as the group dispersion velocity. Standard single mode fibers (SSMF) have dispersion coefficient of 17 ps/(nm·km) which generates significant pulse broadening after long-haul transmission distances. To mitigate this impairment, dispersion compensation fibers (DCF) with negative dispersion coefficient were introduced. The most widely used

DCF has a dispersion around -170 ps/(nm·km). These fibers were very useful in "dispersion-managed" systems which consisted on interleaving fibers with positive and negative slope to have accumulated dispersion at the end of transmission close to 0 ps/(nm·km). For recent coherent systems, DCFs are not anymore necessary since dispersion can be compensated using receiver signal processing through digital filters, thus enabling simpler system design.

Finally, the last linear impairment we treat in this section is polarization mode dispersion. This signal distortion arises from fiber birefringence which is the dependence of the refractive index on the signal polarization. PMD is usually modeled as a concatenation of infinitesimal randomly coupled birefringent sections. Using this model, we can write the equivalent PMD channel frequency transfer function:

$$\begin{bmatrix} y^H(f) \\ y^V(f) \end{bmatrix} = \begin{bmatrix} H^{HH}(f) & H^{VH}(f) \\ H^{HV}(f) & H^{VV}(f) \end{bmatrix} \begin{bmatrix} x^H(f) \\ x^V(f) \end{bmatrix} \tag{2.9}$$

where $x^H(f)$ and $x^V(f)$ are the fiber input signals in the frequency domain corresponding to the signals in horizontal and vertical polarizations, respectively. $y^H(f)$ and $y^V(f)$ are the output signals after transmission over a fiber with PMD. The channel transfer function [32] can be modeled by the concatenation of *P* birefringent sections:

$$\begin{bmatrix} H^{HH}(f) & H^{VH}(f) \\ H^{HV}(f) & H^{VV}(f) \end{bmatrix} = \prod_{p=1}^{P} \begin{bmatrix} e^{j\frac{\varphi_p + 2\pi f \tau_p}{2}} & 0 \\ 0 & e^{-j\frac{\varphi_p + 2\pi f \tau_p}{2}} \end{bmatrix} \begin{bmatrix} \cos\gamma_p & \sin\gamma_p \\ -\sin\gamma_p & \cos\gamma_p \end{bmatrix} \tag{2.10}$$

where φ_p is the phase difference between fast and slow axis, τ_p is the differential group delay between the fast and slow axes and γ_p is the polarization rotation of the pth birefringent section. Despite the stochastic nature of PMD, the fact that it can be modeled as a time-varying butterfly filter is useful to get insight in how to design the receiver signal processing to make it capable to mitigate it.

To conclude this section, we present in Fig. 2.3 the simplified model of the optical transmission channel in the linear regime. On the left hand side of this figure, we can observe the channel we want to model consisting of N_{span} spans of single mode fiber separated by optical amplifiers. On the right hand side, the simplified model consisting in splitting the optical field in two orthogonal components (polarizations) is depicted. First we have the impairments that can be modeled as filters: chromatic dispersion (CD) which can be seen as two polarization-independent filters and then PMD which can be modeled by a time-varying butterfly filter. Finally, we have additive noise which depends on: number of spans, span loss, amplifier noise figure and amplifier output power (see Eq. *2.7*).

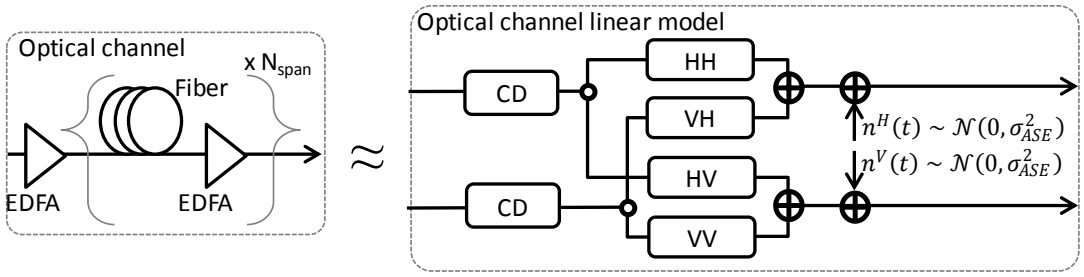

Fig. 2.3: Left: Optical transmission link. Right: linear modeling using linear filters and additive noise.

2.3. ***Receiver and signal processing***

At the receiver, each channel is sent to a coherent receiver, followed by signal processing to recover the transmitted data. Fig. 2.4 shows a typical example of a coherent receiver with polarization diversity and signal processing [33]. Such a receiver can detect both the in-phase and quadrature components of the two arbitrary, but orthogonal, polarizations states to convert the full optical field into the electrical domain (a total of four signals). This receiver is made of a polarization beam splitter (PBS), followed by two 90°-hybrids and a local oscillator. First a PBS splits up the received signal into two arbitrary, but orthogonal polarization components. Each of the polarization components is mixed with the output of the local oscillator laser. Here we use intradyne detection as the central frequency of the local oscillator is slightly different from the signal central frequency ($\omega_{LO} \approx \omega_{TX}$). This frequency (and phase) mismatch is later recovered using signal processing.

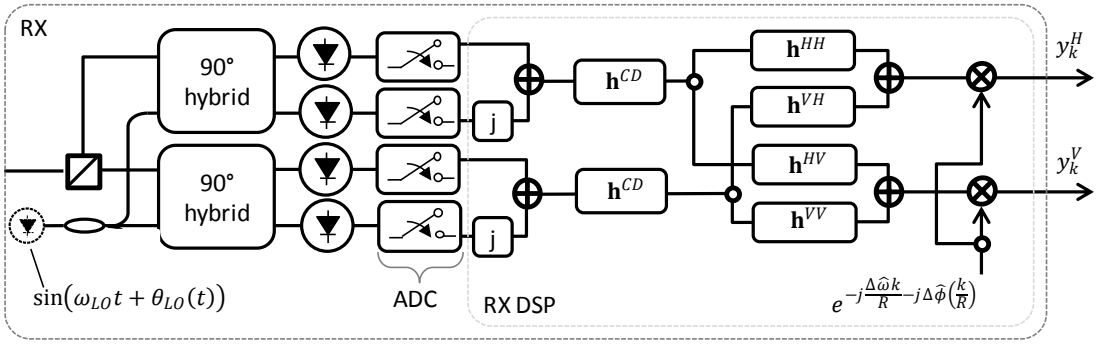

Fig. 2.4: Coherent receiver with polarization diversity and signal processing.

At each output of 90°-hybrids, we have the sum of the projection of the received signal into one polarization with the local oscillator (with different relative phases 0 or $\pi/2$). These four signals supply four single-ended photodiodes and the photocurrent of each photodiode (I_{HI}, I_{HQ}, I_{VI} and I_{VQ}) contains: a direct term proportional to the power of the received signal and local oscillator (direct detection

terms $|E_H|^2$, $|E_V|^2$ and $|E_{LO}|^2$), plus a product term corresponding to the down-converted signal components as in the following equation [34]:

$$\begin{bmatrix} I_{HI} \\ I_{HQ} \\ I_{VI} \\ I_{VQ} \end{bmatrix} = \begin{bmatrix} 1/2 & 0 & 0 & 0 & 1/4 & 0 & 1/8 \\ 0 & 1/2 & 0 & 0 & 1/4 & 0 & 1/8 \\ 0 & 0 & 1/2 & 0 & 0 & 1/4 & 1/8 \\ 0 & 0 & 0 & 1/2 & 0 & 1/4 & 1/8 \end{bmatrix} \begin{bmatrix} \Re\{E_H E_{LO}^*\} \\ \Im\{E_H E_{LO}^*\} \\ \Re\{E_V E_{LO}^*\} \\ \Im\{E_V E_{LO}^*\} \\ |E_H|^2 \\ |E_V|^2 \\ |E_{LO}|^2 \end{bmatrix}. \quad (2.11)$$

The four product terms ($\Re\{E_H E_{LO}^*\}$, $\Im\{E_H E_{LO}^*\}$, $\Re\{E_V E_{LO}^*\}$ and $\Im\{E_V E_{LO}^*\}$) correspond to the in-phase and quadrature components along both polarizations, a direct map of the down-converted optical field in the electrical domain (our signals of interest). These four signals can be then finally extracted by filtering out the direct detection terms. Note that the local oscillator direct detection component ($|E_{LO}|^2$) is constant and can be easily suppressed, however the signal direct detection components ($|E_H|^2$ and $|E_V|^2$) are time-varying. To limit the impact of signal direct detection components, we can set the local oscillator power to be much higher than the signal power resulting in negligible impact of direct detection term (for example, $|E_H|^2 \ll \Re\{E_H E_{LO}^*\}$). Another possibility is using the four extra outputs of 90°-hybrids to supply four additional photodiodes. We can then obtain the following photocurrents:

$$\begin{bmatrix} \bar{I}_{HI} \\ \bar{I}_{HQ} \\ \bar{I}_{VI} \\ \bar{I}_{VQ} \end{bmatrix} = \begin{bmatrix} -1/2 & 0 & 0 & 0 & 1/4 & 0 & 1/8 \\ 0 & -1/2 & 0 & 0 & 1/4 & 0 & 1/8 \\ 0 & 0 & -1/2 & 0 & 0 & 1/4 & 1/8 \\ 0 & 0 & 0 & -1/2 & 0 & 1/4 & 1/8 \end{bmatrix} \begin{bmatrix} \Re\{E_H E_{LO}^*\} \\ \Im\{E_H E_{LO}^*\} \\ \Re\{E_V E_{LO}^*\} \\ \Im\{E_V E_{LO}^*\} \\ |E_H|^2 \\ |E_V|^2 \\ |E_{LO}|^2 \end{bmatrix}. \quad (2.12)$$

Finally we can subtract the outputs to obtain:

$$\begin{bmatrix} I_{HI} \\ I_{HQ} \\ I_{VI} \\ I_{VQ} \end{bmatrix} - \begin{bmatrix} \bar{I}_{HI} \\ \bar{I}_{HQ} \\ \bar{I}_{VI} \\ \bar{I}_{VQ} \end{bmatrix} = \begin{bmatrix} \Re\{E_H E_{LO}^*\} \\ \Im\{E_H E_{LO}^*\} \\ \Re\{E_V E_{LO}^*\} \\ \Im\{E_V E_{LO}^*\} \end{bmatrix}. \quad (2.13)$$

We refer to this approach as coherent detector with polarization diversity and balanced photodiodes. This approach is the one used in the experimental results described for the rest of this thesis. Afterwards, the four signals are digitized using analog-to-digital converters operating approximately at 2 samples per symbol. After sampling, we have the four components at 2 samples per symbol. Note that there is normally a small mismatch between the reference clock of the transmitter DAC and

the receiver ADC, therefore it is necessary to implement timing recovery algorithms to continuously track this clock mismatch in real time implementations to guarantee that the receiver signal is precisely at 2 samples per symbol. These algorithms are usually based on the Gardner timing error estimator [35]. For laboratory purposes, we usually deal with oscilloscope recorded waveforms that are post-processed using off-line algorithms. First, the oscilloscope sampling rate is usually not twice the symbol rate, therefore we need to resample the recorded waveform to emulate an ADC operating at 2 samples per symbol. Second, these waveforms are time-limited, typically less than 1 ms due to oscilloscopes limited memory, therefore the impact of clock mismatch cannot be properly quantified in such short waveforms. That is the reason why in this thesis we do not use timing recovery algorithms, even though they are a critical block in real-time implementations.

Assuming perfect sampling, signal processing algorithms have to deal with three main impairments to be able to recover the transmitted data. First it has to compensate the transmission link accumulated dispersion. As we have seen in the previous section, chromatic dispersion can be modeled by a filtering function that is polarization-independent. Therefore this distortion can be compensated by two digital filters ($\mathbf{h}^{CD}$) which are explained in sub-section 2.3.1. Then, we can deal with polarization-dependent effects such as PMD and polarization rotation. As we have seen in previous section, these effects can be modeled as a butterfly filter. To deal with these time-variant impairments we use an adaptive equalizer in a butterfly structure ($\mathbf{h}^{HH}$, $\mathbf{h}^{HV}$, $\mathbf{h}^{VH}$ and $\mathbf{h}^{VV}$ in Fig. 2.4). This equalizer can also perform the matched filter function and find the optimal sampling instant. The butterfly equalizer implementation is discussed in sub-section 2.3.2. After adaptive equalization, we can now operate at just 1 sample per symbol. The remaining impairments to compensate arise from the use of intradyne detection, which means that the lasers used as signal carrier and local oscillator are different and thus have slightly different central frequency and instantaneous phase. We can split this problem in two: first we estimate and compensate the difference between the central frequency of the carrier signal and local oscillator ($\Delta\omega = \omega_{LO} - \omega_{TX}$), then we estimate and compensate the remaining time-varying instantaneous phase. The frequency estimator is described in sub-section 2.3.3 and the phase estimator in sub-section 2.3.4.

Finally, we obtain two signals y_k^H and y_k^V (see Fig. 2.2) corresponding to noise-corrupted versions of the sent symbols x_k^H and x_k^V (see Fig. 2.4). In the linear regime, and even after signal processing, the distribution of noise of (y_k^H-x_k^H) and (y_k^V-x_k^V) can be accurately modeled a zero-mean independent complex Gaussian distribution with variance dominated by ASE noise (see Eq. *2.7*). Therefore, all the

tools described in Chapter 1 can be applied, including arbitrary modulation formats and channel coding making the transmitter shown in Fig. 2.2 and the receiver in Fig. 2.4 very flexible blocks.

2.3.1 CD compensation

Now we describe the compensating algorithms, starting with chromatic dispersion compensation. Prior to the advent of coherent optical systems with receiver enhanced signal processing, chromatic dispersion was compensated using dispersion compensating fiber (DCF). An alternative to DCF is electronically compensating the chromatic dispersion using digital signal processing resulting in simplified link design. Therefore, digital chromatic dispersion compensation is an essential block in the receiver signal processing. The chromatic dispersion after propagation can be modeled by the frequency domain transfer function:

$$G(\omega) = e^{-j\frac{DL\lambda^2}{4\pi c}\omega^2} \tag{2.14}$$

where *D* is the dispersion coefficient, *L* is the transmission distance, λ is the wavelength of the WDM channel and *c* is the speed of light. This is an all-pass filter that can be inverted to compensate the dispersion. This compensating block is normally implemented using finite impulse response filters where the length of the truncated impulse response depends on the amount of accumulated dispersion (*D* times *L*) and the bandwidth of the signal. Assuming sufficiently large number of taps and sampling rate of 2 samples per symbol, the filter coefficients can be written as:

$$h_k^{CD} = \sqrt{\frac{jcT^2}{D\lambda^2 L}} e^{-j\frac{\pi cT^2}{DL\lambda^2}k^2} \tag{2.15}$$

Using matrix notation the compensated signals y_k^H and y_k^V can be calculated by:

$$y_k^H = \mathbf{h}^{CD}\mathbf{x}_k^H \tag{2.16}$$

$$y_k^V = \mathbf{h}^{CD}\mathbf{x}_k^V \tag{2.17}$$

where $\mathbf{h}^{CD} = [h_{k-N}^{CD}, \ldots, h_k^{CD}, \ldots, h_{k+N}^{CD}]$ and the input vectors $\mathbf{x}_k^H = [x_{k-N}^H, \ldots, x_k^H, \ldots, x_{k+N}^H]^T$ and $\mathbf{x}_k^V = [x_{k-N}^V, \ldots, x_k^V, \ldots, x_{k+N}^V]^T$ are the input signals at 2 samples per symbol coming from the horizontal and vertical polarizations respectively. Note that the impulse response of chromatic dispersion filters can be quite long. For example, considering 6000 km long transoceanic transmission link with 20 ps/(nm·km) and signal symbol rate equal to 37.5 GBd (0.3 nm), we obtain accumulated dispersion of 36000 ps (more than 1000 symbol periods). Therefore, these filters are usually more

efficiently implemented in the frequency domain using overlap-and-save methods and fast Fourier transforms (FFT).

2.3.2 Adaptive equalization

This signal processing block named here adaptive equalizer deals with time varying linear impairments. Among these impairments, we highlight polarization dependent impairments such as polarization rotation which can be modeled by a Jones matrix and polarization mode dispersion (PMD) which can be modeled as frequency dependent Jones matrix [36]. To successfully compensate these impairments, a butterfly equalizer structure is necessary such as the one showed in Fig. 2.5 to deal with mixing between orthogonal polarizations. In addition to polarization dependent impairments, this adaptive equalizer can also be used to implement the matched filter, find the optimal sampling instant and compensate residual chromatic dispersion. It can also mitigate eventual low pass filtering impairments coming from transmitter components, add-drop nodes or receiver components.

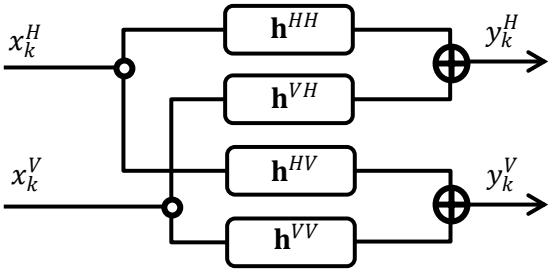

Fig. 2.5: Equalizer with butterfly structure.

We first define x_k^H and x_k^V as the sampled signals at the input of the equalizer (after CD compensation) coming from horizontal and vertical polarization respectively. We also define $\mathbf{x}_k^H$ and $\mathbf{x}_k^V$ as 2N+1 long vectors ($\mathbf{x}_k^H$ = $[x_{k-N}^H, \dots, x_k^H, \dots, x_{k+N}^H]^\mathsf{T}$ and $\mathbf{x}_k^V$ = $[x_{k-N}^V, \dots, x_k^V, \dots, x_{k+N}^V]^\mathsf{T}$ to simplify notation). The two equalizer outputs are y_k^H and y_k^V and the time-varying equalizer filters are $\mathbf{h}_k^{HH}$, $\mathbf{h}_k^{HV}$, $\mathbf{h}_k^{VH}$ and $\mathbf{h}_k^{VV}$, with $\mathbf{h}_k^{HH}$=$[h_{k,-N}^{HH}, \dots, h_{k,0}^{HH}, \dots, h_{k,N}^{HH}]^\mathsf{T}$ and so on. Finally, the transfer function equalizer with butterfly structure is:

$$y_k^H = \sum_{n=-N}^{N} x_{k+n}^H h_{k,n}^{HH} + x_{k+n}^V h_{k,n}^{VH} \tag{2.18}$$

$$y_k^V = \sum_{n=-N}^{N} x_{k+n}^H h_{k,n}^{HV} + x_{k+n}^V h_{k,n}^{VV}\,. \tag{2.19}$$

And using matrix notation:

$$\begin{bmatrix} y_k^H \\ y_k^V \end{bmatrix} = \begin{bmatrix} (\mathbf{h}_k^{HH})^T & (\mathbf{h}_k^{VH})^T \\ (\mathbf{h}_k^{HV})^T & (\mathbf{h}_k^{VV})^T \end{bmatrix} \begin{bmatrix} \mathbf{x}_k^H \\ \mathbf{x}_k^V \end{bmatrix}. \tag{2.20}$$

So assuming this structure, the problem of adaptive equalization is finding the equalizers $\mathbf{h}_k^{HH}$, $\mathbf{h}_k^{HV}$, $\mathbf{h}_k^{VH}$ and $\mathbf{h}_k^{VV}$ as a function of time (k). Note that for this particular description the input is sampled at 2 samples per symbol, so we can restrict the equalizer calculation for every 2 samples (2k). This estimation of equalizer coefficients can be done using data-aided or blind algorithms, however blind solutions are normally favored to reduce training sequence overhead. A common blind approach for constant amplitude signals is using the constant modulus algorithm that tries to minimize $\left(\varepsilon_k^H\right)^2 = \left(1 - \left|y_k^H\right|^2\right)^2$ and $\left(\varepsilon_k^V\right)^2 = \left(1 - \left|y_k^V\right|^2\right)^2$. This technique is particularly interesting since it is tolerant to frequency detuning as well as phase noise distortions which do not affect the amplitude information. Assuming equalizer input signals at 2 samples per symbol, equalizer coefficients $\mathbf{h}_k^{HH}$ and $\mathbf{h}_k^{VH}$ (resp. $\mathbf{h}_k^{HV}$ and $\mathbf{h}_k^{VV}$) can be estimated after observing a block of received symbols of size 2M+1 by performing the following minimization procedure.

$$\mathbf{h}_k^{HH}, \mathbf{h}_k^{VH} = \arg \min_{\mathbf{h}^{HH}, \mathbf{h}^{VH}} \sum_{m=-M}^{M} \left(\varepsilon_{k+2m}^H\right)^2 \tag{2.21}$$

$$\mathbf{h}_k^{HH}, \mathbf{h}_k^{VH} = arg \min_{\mathbf{h}^{HH}, \mathbf{h}^{VH}} \sum_{m=-M}^{M} \left(1 - \left| [(\mathbf{h}^{HH})^T \quad (\mathbf{h}^{VH})^T] \begin{bmatrix} \mathbf{x}_{k+2m}^H \\ \mathbf{x}_{k+2m}^V \end{bmatrix} \right|^2 \right)^2 \tag{2.22}$$

To avoid storage of a whole signal block, we can also perform the minimization in a symbol-by-symbol basis using stochastic gradient descent. Using μ as the parameter to control the speed of the convergence and tracking, the equalizer update can be written as [36]:

$$\mathbf{h}_{2k+2}^{HH} := \mathbf{h}_{2k}^{HH} - \frac{\mu}{4} \frac{d\left(\varepsilon_{2k}^H\right)^2}{d\mathbf{h}_{2k}^{HH}} = \mathbf{h}_{2k}^{HH} + \mu \cdot \varepsilon_{2k}^H \cdot y_{2k}^H \cdot (\mathbf{x}_{2k}^H)^* \tag{2.23}$$

$$\mathbf{h}_{2k+2}^{HV} := \mathbf{h}_{2k}^{HV} - \frac{\mu}{4} \frac{d\left(\varepsilon_{2k}^V\right)^2}{d\mathbf{h}_{2k}^{HV}} = \mathbf{h}_{2k}^{HV} + \mu \cdot \varepsilon_{2k}^V \cdot y_{2k}^V \cdot (\mathbf{x}_{2k}^H)^* \tag{2.24}$$

$$\mathbf{h}_{2k+2}^{VH} := \mathbf{h}_{2k}^{VH} - \frac{\mu}{4} \frac{d\left(\varepsilon_{2k}^H\right)^2}{d\mathbf{h}_{2k}^{VH}} = \mathbf{h}_{2k}^{VH} + \mu \cdot \varepsilon_{2k}^H \cdot y_{2k}^H \cdot (\mathbf{x}_{2k}^V)^* \tag{2.25}$$

$$\mathbf{h}_{2k+2}^{VV} := \mathbf{h}_{2k}^{VV} - \frac{\mu}{4} \frac{d\left(\varepsilon_{2k}^V\right)^2}{d\mathbf{h}_{2k}^{VV}} = \mathbf{h}_{2k}^{VV} + \mu \cdot \varepsilon_{2k}^V \cdot y_{2k}^V \cdot (\mathbf{x}_{2k}^V)^* \tag{2.26}$$

Even though this approach is designed for constant amplitude signals such as QPSK, it can be extended to multi-amplitude constellations by slightly changing the

errors functions ε_k^H and ε_k^V. For example, 16QAM has three amplitudes proportional to $r_0 = \sqrt{2}$, $r_1 = \sqrt{10}$ and $r_2 = \sqrt{18}$, corresponding to the inner, middle and outer constellation rings , respectively. The error function can be then modified to:

$$\varepsilon_k^H = (\hat{r})^2 - \left|y_k^H\right|^2 \tag{2.27}$$

$$\varepsilon_k^V = (\hat{r})^2 - \left|y_k^V\right|^2 \tag{2.28}$$

where $\hat{r}$ represents the closest ring to the received symbol. With this modified error function, we can do a block minimization as in Eq. *2.21* or use the stochastic gradient method. This is known as the radius-directed equalizer [37].

Finally, since subsequent DSP blocks can work with only 1 sample per symbol, we need to down-sample the signal which can be done jointly with adaptive equalization. For example in the case of 2 samples per symbol equalizer input signal, we can simply perform equalization every 2 samples. Then after adaptive equalization, the 1 sample per symbol signal is only corrupted by frequency and phase distortions coming from different relative frequency and phase between signal carrier and local oscillator.

2.3.3 Carrier frequency estimation

As previously mentioned, the lasers used as signal carrier and local oscillator are different and thus have slightly different central frequency and instantaneous phase. We can also assume that for estimation purposes that the phase component varies slowly over time. Additionally, we can split estimation and compensation problems in 2 steps. A coarse estimation to find the frequency offset, followed by a fine estimation to estimate a slowly varying phase and residual frequency offset. The problem of frequency estimation can be modeled by the following equation:

$$y_k = x_k \cdot e^{j\omega k + j\phi} + n_k, \tag{2.29}$$

where x_k is the sent complex symbol defined by one of the constellation points, ω is the unknown frequency we want to estimate, ϕ is an unknown phase, n_k is complex white Gaussian noise with variance $N_0/2$ per dimension and y_k is the observed corrupted signal at 1 sample per symbol. The frequency ω relates to the difference in central frequency Δf between signal and local oscillator lasers by the formula $\omega = 2\pi\Delta f/R$. To simplify the problem, we can first assume the sent symbols are always of constant amplitude, so the problem becomes:

$$y_k = e^{j\omega k + j\phi} + n_k. \tag{2.30}$$

The maximum likelihood frequency estimation after N observations and assuming complete knowledge of unknown phase ϕ can be written as:

$$\hat{\omega} = arg \max_{\omega} p(\, y_0, \ldots, \, y_k, \ldots \, y_{N-1} | \omega, \phi), \tag{2.31}$$

where $\hat{\omega}$ is the estimated frequency and $p(\, y_0, \ldots, \, y_k, \ldots \, y_{N-1} | \omega, \phi)$ is the probability of receiving N symbols, given prior knowledge of the frequency ω and the phase ϕ. Since the noise vector distribution is independent Gaussian with zero mean, we can develop the joint the probability as:

$$p(\, y_0, \ldots, \, y_k, \ldots \, y_{N-1} | \omega, \phi) = \prod_{k=0}^{N-1} \frac{1}{\pi N_0} e^{\frac{-\left| y_{k+n} - e^{j\omega k + j\phi} \right|^2}{N_0}}. \tag{2.32}$$

Then taking the log (which does not affect the maximization) and disconsidering all the terms that do not depend on ϕ and ω, we obtain:

$$\log\big(p(\, y_0, \ldots, \, y_k, \ldots \, y_{N-1} | \omega, \phi)\big) \propto C_1 - \sum_{k=0}^{N-1} \left| y_k - e^{j\omega k + j\phi} \right|^2, \tag{2.33}$$

where C_1 is a constant that does not depend on ϕ and ω, so it does not affect the maximization either. We can then develop the squared distance term to obtain:

$$\sum_{k=0}^{N-1} \left| y_k - e^{j\omega k + j\phi} \right|^2 = \sum_{k=0}^{N-1} |y_k|^2 - 2\Re(y_k e^{-j\omega k - j\phi}) + \left| e^{j\omega k + j\phi} \right|^2. \tag{2.34}$$

Since $|y_k|^2$ has no impact on the maximization and $\left| e^{j\omega k + j\phi} \right|^2 = 1$, we can include these terms in another constant term (C_2). We finally obtain:

$$\log\big(p(\, y_0, \ldots, \, y_k, \ldots \, y_{N-1} | \omega, \phi)\big) \propto C_2 + \Re\left(\sum_{k=0}^{N-1} y_k e^{-j\omega k - j\phi} \right). \tag{2.35}$$

Therefore, if we know the phase ϕ, $\hat{\omega}$ can be found by maximizing:

$$\hat{\omega} = arg \max_{\omega} \Re\left(\sum_{k=0}^{N-1} y_k e^{-j\omega k - j\phi} \right). \tag{2.36}$$

Since this phase is unknown, the maximization can be simplified to (please refer to [38] for a complete development):

$$\hat{\omega} = arg \max_{\omega} \left| \sum_{k=0}^{N-1} y_k e^{-j\omega k} \right| \tag{2.37}$$

This maximization cannot be performed analytically, however we can test a large number of frequencies, evaluating $\left| \sum_{k=0}^{N-1} y_k e^{-j\omega k} \right|$ and choosing the frequency

that maximizes this metric. Note that when N is a power of two, testing frequencies equally spaced between 0 and 2π can be efficiently calculated using the fast Fourier transform.

However, this frequency estimator represents the case where we do not send any data. Fortunately, even in the presence of data we can transform the problem defined in Eq. *2.29* to the problem in Eq. *2.30*. For example, assuming that the symbol x_k belongs to the QPSK constellation, x_k can take 4 values {1,-1,j,-j}. By simply taking the fourth power of x_k, we can remove data dependency [39] ($(x_k)^4 = 1$):

$$(y_k)^4 = (x_k \cdot e^{j\omega k + j\phi} + n_k)^4 = e^{j4\omega k + j4\phi} + (n_k)^4 + d_k. \tag{2.38}$$

The 4th-power signal has an exponential frequency component with a frequency 4 times higher than the original one, additive Gaussian noise with higher variance than the original noise and a final term d_k representing all the cross products. Therefore, the problem of estimating the frequency can be reduced to:

$$\widehat{\omega} = \frac{arg\max_{\omega} \left| \sum_{k=0}^{N-1} (y_k)^S e^{-j\omega k} \right|}{S}, \tag{2.39}$$

where S is the rotational symmetry of the constellation (S=2 for BPSK, S=4 for QPSK, S=8 for 8PSK). For the rest of this thesis, I will refer to this method as the Sth-power periodogram method. Note that this method can also be used with constellations such as 16QAM, because 8 points (4 from the inner ring plus 4 from the outer ring) have equally spaced phases (S=4).

Note that $\widehat{\omega}$ can have values between $-\pi/S$ and π/S, so this algorithm is limited to the cases where $-R/(2S) < \Delta f < R/(2S)$ since $\omega = 2\pi\Delta f/R$. For example using 32 GBd QPSK signal, the 4th-power periodogram has tolerance to a frequency offset between -4 GHz and 4 GHz. This value is larger than the sum of the uncertainty of central frequency of two typical laser sources designed for long-haul transmission (± 1.5 GHz per laser resulting in (± 3 GHz).

2.3.4 Carrier phase estimation

Afterwards, we should compensate the remaining phase and possible residual frequency offset. This estimation problem can be modeled by the following equation:

$$y_k = x_k \cdot e^{j\theta_k} + n_k, \tag{2.40}$$

where x_k is the sent complex symbol defined by one of the constellation points, θ_k is the unknown phase we want to estimate, n_k is complex white Gaussian noise with

variance $N_0/2$ per dimension and y_k is the received symbol corrupted by phase noise and additive noise. As a first step, we simplify the problem and we consider that θ_k does not vary over time. Thus we set $\theta_k=\theta$ for all k and the maximum likelihood estimation after observing 2N+1 received symbols and assuming complete knowledge of sent symbols can be written as:

$$\hat{\theta} = arg\max_{\theta} p(\, y_{k-N}, \dots, \, y_k, \dots \, y_{k+N} | \theta). \tag{2.41}$$

where $\hat{\theta}$ is the estimated phase and $p(\, y_{k-N}, \dots, \, y_k, \dots \, y_{k+N} | \theta)$ is the probability of receiving 2N+1 symbols, given prior knowledge of the phase θ. Since the noise vector distribution is independent Gaussian with zero mean, we can develop the joint probability density function as:

$$\hat{\theta} = arg\max_{\theta} \prod_{n=-N}^{N} \frac{1}{\pi N_0} e^{\frac{-\left|y_{k+n} - x_{k+n} e^{j\theta}\right|^2}{N_0}}. \tag{2.42}$$

Then taking the log (which does not affect the maximization) and disconsidering all the terms that do not depend on θ, we obtain:

$$\hat{\theta} = arg\min_{\theta} \sum_{n=-N}^{N} \left|y_{k+n} - x_{k+n} e^{j\theta}\right|^2 = arg\min_{\theta} \sum_{n=-N}^{N} \left|y_{k+n} e^{-j\theta} - x_{k+n}\right|^2. \tag{2.43}$$

This sum of squared distances is minimized by the estimated phase:

$$\hat{\theta} = \angle\left(\sum_{n=-N}^{N} (y_{k+n})^* x_{k+n} \right). \tag{2.44}$$

If we assume the phase does not vary over time, increasing the averaging (N) always results in better estimation, however this assumption is not correct. The behavior of this phase can be more accurately described by a Wiener process in which $\theta_{k+1} = \theta_k + b_k$, where b_k has Gaussian distribution with zero mean and variance 2πW/R (W is the sum of linewidths of signal and local oscillator lasers and R is the symbol rate [40]). Nevertheless, we can still use the same estimator given that the averaging length (N) is optimized to reduce estimation average error. If N is too small, we can track fast variations of the phase θ_k however the additive noise is not sufficiently averaged. If N is too large, we can better average the additive noise, however we risk including phases that are not sufficiently correlated in the estimation process.

Up to here, we considered the case where we know the sent symbols x_n. However, it is interesting to estimate the carrier phase without knowledge of the transmitted data. One simple way to remove data dependency is replacing sent

symbols in Eq. *2.43* by decided symbols (closest constellation point). The new estimated phase $\hat{\theta}_{NDA}$ derived from non data-aided estimation is:

$$\hat{\theta}_{NDA} = arg\min_{\theta} \sum_{n=-N}^{N} \left| y_{k+n}e^{-j\theta} - D(y_{k+n}e^{-j\theta}) \right|^2, \quad (2.45)$$

where D(.) represents the decision operation which returns the closest constellation point. Note that this approach has two problems. The first one is that this function cannot be minimized analytically as in Eq. *2.44*. In addition, there is typically more than one phase that minimizes this sum of squared distances depending on the rotational symmetry (S) of the constellation. For example, for QPSK, 16QAM and 64QAM, the function to be minimized has four minima. To tackle these two problems, we can test equally spaced candidate phases, evaluate the metric $\sum_{n=-N}^{N} \left| y_{k+n}e^{-j\theta} - D(y_{k+n}e^{-j\theta}) \right|^2$, and choose the phase that minimizes this metric. The metric has ambiguities over the range 0 to 2π, since:

$$\left| y_{k+n}e^{-j\theta} - D(y_{k+n}e^{-j\theta}) \right|^2 = \left| y_{k+n}e^{-j\left(\theta+\frac{2\pi}{S}\right)} - D\left(y_{k+n}e^{-j\left(\theta+\frac{2\pi}{S}\right)}\right) \right|^2, \quad (2.46)$$

therefore we can test phases between 0 and $2\pi/S$, and then apply a phase unwrapper that can deal with discontinuities. This algorithm, which tests equally spaced phases between 0 and $2\pi/S$, chooses the phase that minimizes $\sum_{n=-N}^{N} \left| y_{k+n}e^{-j\theta} - D(y_{k+n}e^{-j\theta}) \right|^2$ followed by a phase unwrapper was proposed in [41] and it will be named in this thesis as blind phase search (BPS) algorithm.

Assuming the use of the blind phase search algorithm, there is still an absolute phase ambiguity that can be modeled by writing the received symbol y_k after carrier phase estimation as:

$$y_k = x_k \cdot e^{2\pi s/S} + n_k, \quad (2.47)$$

where y_k is the received symbol, x_k the sent symbol, n_k additive white Gaussian noise, the exponential term represents the unknown phase which depends on the ambiguity (symmetry) S of the constellation and s an unknown integer. This phase represented by s can be estimated by sending K known pilot symbols using the following minimization:

$$\hat{s} = arg\min_{s} \left| \sum_{k=1}^{K} \left(y_k - x_k \cdot e^{\frac{2\pi s}{S}} \right) \right|^2, \quad (2.48)$$

which can be solved with:

$$\hat{s} = round\left(\frac{\angle\left(\sum_{k=1}^{K}(y_k \cdot x_k^*)\right) \cdot S}{2\pi}\right) \tag{2.49}$$

The probability of $\hat{s}$ being different of the actual s is equivalent to calculating the symbol error rate of S-PSK signal. Therefore the probability can be approximated by the following equation in the low symbol error rate regime [2]:

$$p(\hat{s} \neq s) \approx 2Q\left(\sqrt{\frac{2KE_s}{N_0}} \cdot sin\left(\frac{\pi}{S}\right)\right). \tag{2.50}$$

So a typical carrier frequency and phase recovery scheme can be divided in three blocks detailed in Fig. 2.6. First, we blindly estimate the frequency ω using the Sth power periodogram described in section 2.3.3. Then, a time-varying phase θ_k is estimated using the blind phase search algorithm. Since there is still one final phase ambiguity between the phase of the transmitter and receiver, pilots are introduced regularly in order to estimate this phase. For example, this phase ambiguity (s in Eq. *2.47*) is a quadrant ambiguity for constellations with symmetry 4 (QPSK, 16QAM, 64QAM). After these three blocks, the receiver is successfully locked in phase with the transmitter.

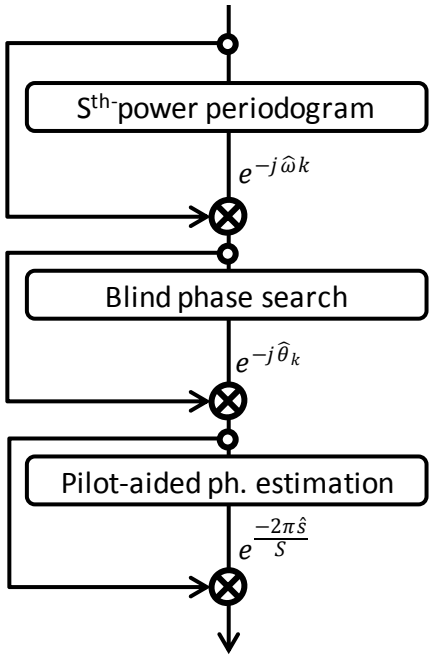

Fig. 2.6: Carrier frequency and phase estimation using three block scheme.

Finally, assuming perfect compensation of all linear effects, the signal-to-noise ratio (SNR) at the receiver after carrier phase estimation can be calculated as:

$$SNR_{RX} = \frac{P_{in}}{P_{ASE}} \tag{2.51}$$

where P_{ASE} is the power of additive noise and can be approximated using Eq. *2.7*. Setting the noise reference bandwidth (B_{ref}) equal to the channel symbol rate *R,* we obtain:

$$P_{ASE} \approx L \cdot \alpha + NF + 10\log_{10} hf_0 R + 10\log_{10} N_{span} \quad (2.52)$$

This model is very flexible since we can include other imperfections and model them as an additional Gaussian noise which degrades the SNR at the receiver. Examples of imperfections include: limited resolution of DAC, ADC or signal processing algorithms, bad calibration of opto-electronic components (i.e. skew), failing to complete compensate linear impairments by receiver algorithms, etc.

2.4. *Gaussian model for propagation over uncompensated links*

So far we have argued that design simplicity is the main reason for using transmission links without dispersion compensation fiber, since chromatic dispersion can be compensated electronically using digital filters as described in Section 2.3.1. However, uncompensated links have two additional advantages: increased transmission reach compared to dispersion-compensated links in some cases and simple analytical model of performance as a function of systems parameters.

For example, in [42], experimental reach of 16x100 Gb/s WDM system based on PDM-QPSK was 2417 km over an uncompensated link and 1335 km over a dispersion managed link. The uncompensated link was made of 38x63.6 km-long spans of SSMF resulting in 1036 ps/nm of dispersion per span. The accumulated dispersion was compensated using digital filters at the receiver. The dispersion-managed link was made of 21 spans of 63.6 km-long SSMF plus 21 distributed dispersion compensation units with -1165 ps/nm resulting in residual dispersion of -128 ps/nm per span. Then, the accumulated residual dispersion was compensated using digital filters. The performance advantage is also validated by all current transmission records which are based on uncompensated links.

2.4.1 Nonlinear interference

Additionally, simple and accurate modeling of system performance of uncompensated links is another advantage of these systems. These highly dispersive links have very interesting propagation properties. Firstly, for each WDM channel, the distribution of each component of the electrical field rapidly approaches a statistically-independent zero-mean Gaussian distribution for PDM-MQAM.

Secondly, the noise distribution after signal processing (carrier phase estimation) can also be very well approximated by an additive Gaussian noise both in linear and nonlinear propagation regimes [43], [44]. This noise can be also divided in two components, one coming from amplifiers corresponding to amplified spontaneous emission and the other coming from non-linear interference with variance proportional to the cube of the fiber input power. Therefore, the performance of a WDM system made of an uncompensated fiber link with EDFA amplification, polarization multiplexed QAM, coherent detection and signal processing can be measured in effective signal-to-noise ratio (SNR_{NLI}) as:

$$SNR_{NLI} = \frac{P_{in}}{P_{ASE} + \gamma_{NLI} P_{in}^3} \tag{2.53}$$

where P_{in} is the linear power per channel at the input of each span and γ_{NLI} is a non-linear coefficient that can be calculated with analytical models. P_{ASE} is the power of the additive noise coming from amplifiers.

Over the past few years, several analytical models have been proposed to calculate non-linear interference noise coefficient γ_{NLI} as a function of system parameters. Some of these models are the frequency domain Gaussian noise model (GNM) [45], the time domain enhanced GNM (EGNM) [46], and the time-domain perturbative approach [47]. Such models have proven to accurately predict system performance.

Using the time-domain perturbative approach, we calculated γ_{NLI} for an exemplary ultra-long-haul transmission system. We consider a system where there are 60 channels spaced by 66.7 GHz in the C-band. Each channel operates at 64 GBd and uses PDM-16QAM. We consider the use of 120 55 km-long spans of ultra-large effective area (A_{eff} = 150 μm^2) silica fiber with attenuation of 0.16 dB/km. This fiber has dispersion factor of 20.6 ps/(nm·km) and non-linear index $n_2 = 2.3 \cdot 10^{-20}$ m^2/W. We consider here the use of EDFA-based amplification after every span and an amplifier noise figure of 5 dB. This exemplary transmission link nicely represents high-performance ultra-long haul systems, which rely on premium fiber (the fiber parameters here are the ones of Corning Vascade EX3000 fiber). The expected transmission distances are beyond 6000 km, corresponding to transatlantic distances. Fig. 2.7 presents the analytical SNR_{RX} and effective SNR_{NLI} assuming Gaussian distribution of non-linear interference as a function of total power injected in each fiber span ($P_{in} \cdot N_{ch}$).

This figure shows that if the optical transmission link behaved only linearly, we could indefinitely increase the amplifiers output power to achieve the desired OSNR after transmission (proportional to SNR_{RX}). However, as we increase the

launch power in the fiber beyond a certain threshold, referred to as non-linear threshold (NLT), Kerr effect-derived interference becomes dominant and performance is degraded with the increasing power (using the SNR_{NLI} metric). The NLT is thus the power corresponding to the maximum performance and represents the trade-off between the performance degradation coming from two different impairments: ASE noise and non-linear interference induced by the Kerr effect. The performance metric SNR_{NLI} is widely used to accurately predict performance of ultra long-haul systems as a function of system parameters.

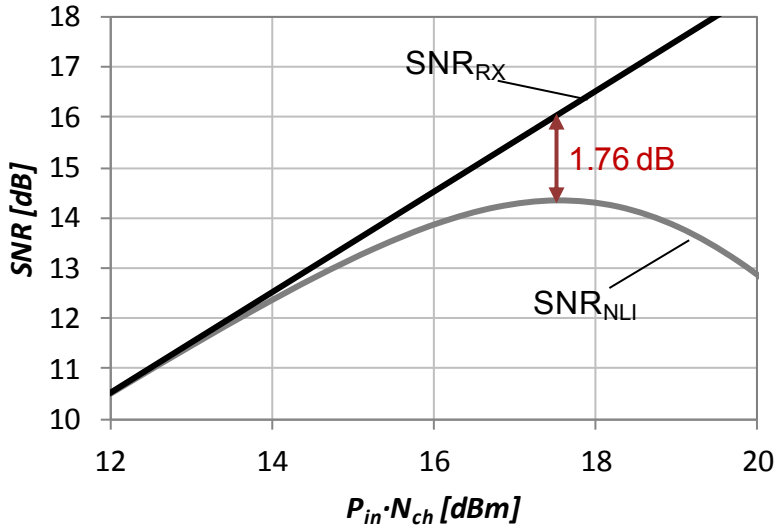

Fig. 2.7: Predicted SNR_{RX} and SNR_{NLI} for 6600 km long uncompensated transmission link.

In addition, the non-linear interference noise coefficient γ_{NLI} can be decomposed into two components: one term coming from non-linear interference generated by the channel under detection itself (intra–channel nonlinear interference [48]) and a remaining term that models interference that depends on neighboring channels. The interference coming from the channel under detection can be potentially compensated using intra-channel non-linear compensation (IC/NLC) algorithms. So assuming perfect non-linear interference mitigation, we can derive another performance metric that models a system with a receiver (or transmitter) that can compensate (or pre-compensate) intra-channel non-linear interference. The new predicted receiver SNR can be written as:

$$SNR_{IC/NLC} = \frac{P_{in}}{P_{ASE} + (\gamma_{NLI} - \gamma_{IC/NLC})P_{in}^3} \tag{2.54}$$

where $\gamma_{IC/NLC}$ is the coefficient modeling the variance of the interference generated by intra-channel nonlinear effects. Fig. 2.8 shows the evolution of the new performance predictor ($SNR_{IC/NLC}$) as a function of total fiber input power.

We observe in this figure that we can potentially increase performance if we partially mitigate interference generated by the Kerr effect. In this example, the non-linear threshold can be increased by 1 dB and the effective SNR at the receiver can be potentially 0.9 dB higher.

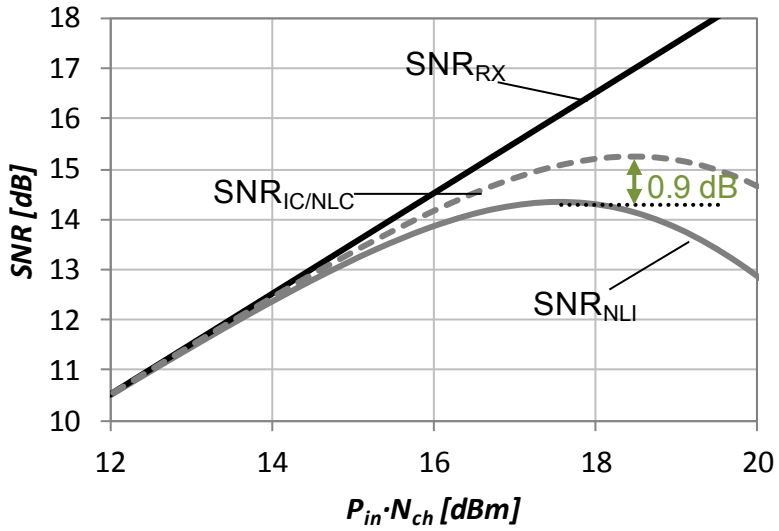

Fig. 2.8: Predicted SNR_{RX}, SNR_{NLI} and $SNR_{IC/NLC}$ for 6600 km long uncompensated transmission link.

2.4.2 Nonlinear compensation

To mitigate intra-channel non-linear effects, several algorithms can be used. Those algorithms are based on the deterministic nature of nonlinearities. One popular algorithm used to mitigate nonlinearities is called digital backpropagation. This algorithm can be implemented either at the transmitter [49] or at the receiver [50]. At the transmitter, we need to synthesize a signal which after transmission over the nonlinear medium corresponds to the target waveform we want to transmit. This can be done by propagating the signal “backwards” from the receiver to the transmitter. The backpropagation can be done digitally using for example the split-step Fourier method. This method commonly used for numerical simulations of optical field propagation in WDM systems approximates the nonlinear Schrodinger equation that describes the transmission over a fiber optic link by modeling the propagation as a series of alternating linear and nonlinear elements.

The same technique can be used at the receiver where we propagate backwards the received signal, from the receiver to transmitter. Fig. 2.9 shows the

schematic of digital backpropagation using split step Fourier transform at the receiver. This block replaces the chromatic dispersion digital filter since it compensates both linear and nonlinear distortions.

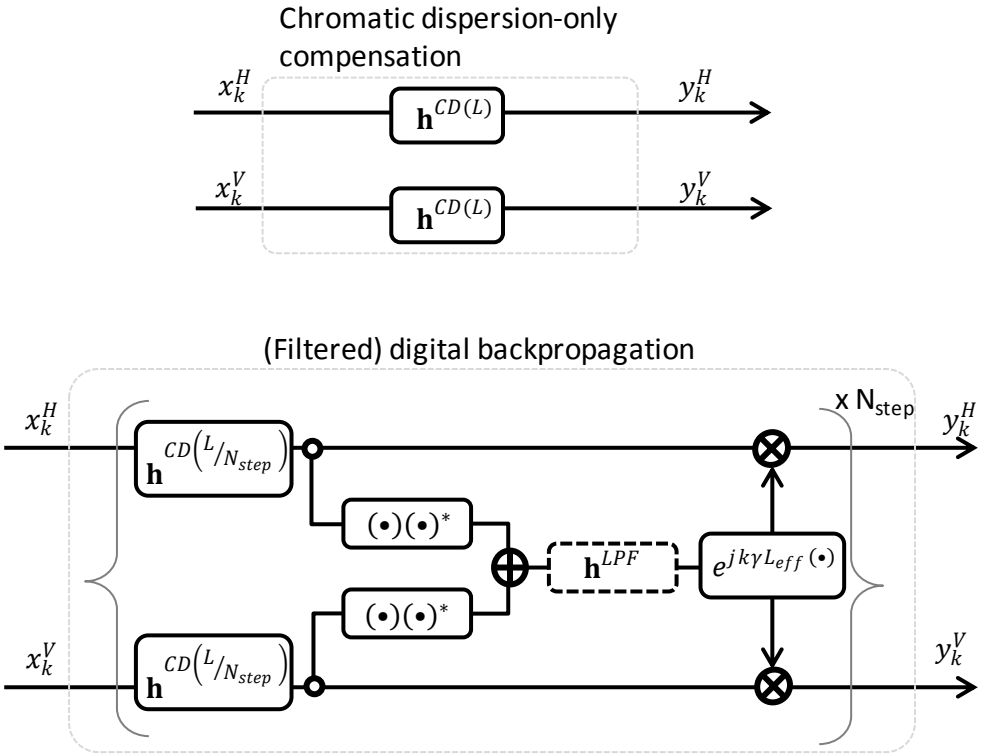

Fig. 2.9: Chromatic dispersion compensation and filtered digital backpropagation.

Contrary to linear-only compensation where chromatic dispersion is compensated for the whole transmission link of length L in one step (using digital filter $\mathbf{h}^{CD(L)}$ calculated using Eq. *4.26*), in digital backpropagation chromatic dispersion and intra-channel nonlinearities compensation is divided in several steps (N_{step}). Each step is divided in two sections: the linear and nonlinear sections. In the linear section, accumulated chromatic dispersion of a small fiber section (length L/N_{step}) is compensated using a digital filter ($\mathbf{h}^{CD(L/N_{step})}$). The nonlinear section consists in applying a phase shift proportional to the instantaneous power. The magnitude of this phase shift also depends on a scaling factor ($k\gamma L_{eff}$), which includes the fiber nonlinear parameter (γ), the step effective length (L_{eff}) and a compensation factor (k). Please refer to [50] for more details. In addition, an optional block consisting of a low pass filter ($\mathbf{h}^{LPF}$) may be included to smooth the instantaneous power before applying the phase shift. The main interest of this filter is reducing the number of steps required for achieving a given performance gain, thus reducing the algorithm implementation complexity. When this low pass filter is present, we refer to the algorithm as filtered digital backpropagation. A complete

description of the algorithm, with detailed discussion of each parameter as well as performance evaluation can be found in [51]. Although this algorithm seems up to now too complex for practical implementation, it is an interesting tool that provides a potential performance that can be achieved by nonlinear compensation algorithms. Lower complexity alternatives based on perturbative theory have been proposed [52], but they are not covered in this thesis.

2.5. *Summary*

This chapter dealt with the main blocks of long-haul transmission systems based on wavelength division multiplexing and coherent detection. We have seen that current optical transmitters are capable of generating arbitrary optical signals to transmit information. Using coherent receivers we can map the optical field into electrical domain with a high fidelity. This enables not only very high flexibility in the transmitted waveform, but also the possibility to compensate for potential channel distortions using signal processing at the receiver (or transmitter).

Afterwards, we modeled the transmission channel including signal processing as two parallel Gaussian channels in the linear regime as well as in the nonlinear regime. This greatly simplifies system design since all the tools described in Chapter 1 can be used for our channel of interest. Based on this model, as well as digital communications and information theory tools previously described, in Chapter 3 we investigate modulation formats optimization for optical transmission. Then in Chapter 4, we use the system concepts described here, state-of-the-art equipment and algorithms to experimentally demonstrate spectrally-efficient high symbol rate systems.

Chapter 3. Modulation format optimization

In this chapter, modulation format design for optical communication systems is investigated. An extensive review of advanced modulation formats can be found in [53], however the review focus on low spectral efficiency formats and signal generation using low-resolution digital-to-analog converters combined with optical components to produce a wide variety of pulse shapes. For example, many of first coherent systems used 2-level electrical driving signal to attack an external modulator to generate non-return-to-zero (NRZ) optical signals. The introduction of a pulse carver added some flexibility and allowed return-to-zero (RZ) pulse shaping, which was attractive to increase the tolerance against fiber non-linearities. Some of these techniques were used in the first-generation of 100 Gb/s coherent transponders that were based on PDM-QPSK.

However, with the advent of high-speed high-resolution DAC, generation of higher spectral efficiency signals became possible by combining high order modulation formats with arbitrary pulse shaping using transmitter digital filters. Nowadays, many systems rely on high-resolution DAC to generate QAM formats with pulse shaping based on root-raised-cosine filter with roll-off factor close to 0 to minimize signal occupation. For example, some commercially available transponders already offer 200 Gb/s single-carrier solutions based on PDM-16QAM.

Nevertheless, the full potential of high-resolution I/Q transmitter with polarization diversity has not yet been fully explored. Performance of current systems which are based on single-carrier, squared-QAM and root-raised-cosine pulse

shaping may be improved by using the following techniques which are briefly described in this introduction: constellation optimization, multi-carrier modulation, multi-dimensional modulation formats, time-interleaved hybrid modulation and constellation shaping.

Constellation optimization corresponds to choosing the best constellation in a given scenario. Traditional metrics to compare constellations are minimum Euclidean distance, noise sensitivity, power efficiency and constellation constrained capacity. A very complete review of modulation formats based on 2-dimensional constellations for optical communications can be found in [54], where different formats are compared in terms of constellation constrained capacity. However, other criteria have to be also considered when choosing the modulation format. For example, the interaction between the modulation format and several system blocks such as adaptive equalizer, carrier frequency and phase estimation, transmission link and FEC decoder.

Multi-dimensional modulation formats have also attracted a lot of attention from the optical communications research community. 4-dimensional modulation formats were proposed to exploit the natural 4 dimensions in the optical field: in-phase and quadrature from two orthogonal polarizations. As opposed to PDM squared-QAM formats that are a subset of the cubic lattice, the proposed modulation formats 8-SPQAM (also called PS-QPSK) and 128-SPQAM are a subset of the D_4 lattice which is the optimal lattice in 4 dimensions resulting in better power efficiency [55]. 4D modulation formats were also proposed to improve the transponder bitrate flexibility by filling the gap between traditional QAM formats. In [56], 32-SPQAM was proposed as a way to provide an intermediate bitrate of 125 Gb/s, which is midway between 100 Gb/s and 150 Gb/s that were implemented using the same symbol rate with PDM-QPSK and PDM-8QAM, respectively. Note that, if we also include the time dimension, arbitrary N-dimension can be achieved at the expense of increased complexity due to high dimensionality. Nevertheless, some interesting propositions investigated modulation beyond 4 dimensions to exploit signal properties other than power efficiency or flexibility. For example using 6 dimensions, a modulation format without phase ambiguity was proposed to deal with cycle slips, which is a challenging impairment in some dispersion-managed systems [57]. In another example which used 8 dimensions, a modulation format tolerant to some transmission non-linearities was also proposed [58]. These demonstrate that multi-dimensional modulation can be used in optical communications to tackle different challenges such as: power efficiency, flexibility, phase noise tolerance and transmission non-linearities.

Another possibility to improve performance of current systems is the use of time-interleaved modulation formats. These formats are attractive to fine tune the spectral efficiency of optical systems to deal with constraints of available bandwidth and FEC overhead. Using this concept, 3200 km transmission was achieved using single-carrier 400 Gb/s signals based on time division multiplexing between 32QAM and 64QAM [59]. These formats have also been used to enable higher transponder flexibility by improving on spectral efficiency granularity and adding bandwidth flexibility. Improving the granularity of spectral efficiency can be achieved by mixing two different modulation formats with different spectral efficiencies so that the resulting signal has an intermediate one. With this technique, we are not limited to integer number of bits per symbol as typical formats thus adding flexibility in bitrate choice resulting in better resource utilization. For example, Hybrid-QPSK/8QAM was proposed to provide an intermediate bitrate [56] of 125 Gb/s, which is midway between 100 Gb/s and 150 Gb/s that were implemented using the same symbol rate with PDM-QPSK and PDM-8QAM, respectively (as previously mentioned). Additionally, bandwidth flexibility can be achieved by providing the same bitrate with different symbol rates. For example 200 Gb/s signals can be generated using 32 GBd, 38 GBd and 43 GBd associated with 16QAM, Hybrid-8QAM/16QAM and 8QAM respectively [60]. Such a flexibility allows signal adaptation for different filtering scenarios, thus maximizing capacity and/or reach in a system.

Although multi-carrier solutions are not the subject of this thesis, it has been widely studied in recent years. Orthogonal frequency division multiplexing (OFDM) [61], Nyquist frequency division multiplexing [62], multi-carrier offset QAM [63] are some examples of multi-carrier solutions that attracted some attention in optical communications literature. One of the advantages of these solutions is its high tolerance to frequency selective channels. Multi-carrier systems have also attractive properties related to mitigation of some transmission nonlinear effects [64]. For example, the inclusion of pilots in OFDM was also studied as a way to compensate non-linearities by exploiting the non-linear phase correlation between neighboring sub-carriers [65].

Finally, an alternative technique that is not covered in this chapter but worth mentioning that can improve the performance compared to current deployed systems is constellation shaping. Shaping can be achieved by making the sent constellation probability distribution approach the Gaussian distribution to increase capacity for a given SNR compared to a more uniform transmitted signal distribution. This can be implemented in several ways and shaping propositions for optical communications include superposition coding [66], probabilistic shaping [67] and shaped iterative polar modulation [68]. Although all these techniques present some performance

advantages compared to current commercial systems, they also significantly increase the implementation complexity. In this chapter, we investigate modulation format design choice considering high-speed optical communications implementation constraints and we focus on constellation optimization, multi-dimensional formats and time-interleaved hybrid formats. We start by investigating 8QAM formats, specially the impact of constellation choice on carrier recovery algorithms [69]. Then, several 8QAM constellations are compared in terms of generalized mutual information [70]. Afterwards, two solutions providing 2.5 bits per symbol per polarization, the first one based on 4D-modulation and the second on time-interleaved hybrid modulation are compared [56]. Finally, the use of 4D modulation in intensity modulation and direct detection systems based on 4PAM is investigated [71].

3.1. *8QAM constellations for long-haul optical communications*

Polarization division multiplexed (PDM-) quadrature phase-shift keying (QPSK) modulation has been the industry standard for providing single-carrier 100 Gb/s services over submarine distances. To answer ever-growing capacity demand of optical networks, solutions providing spectral efficiency greater than PDM-QPSK are of particular interest. Spectral efficiency can be increased by using high-order modulation formats, generally with quadrature amplitude modulation (QAM). Among candidate modulation formats, 8QAM has been widely studied to provide 50% capacity increase compared to QPSK systems [72]. Star-8QAM [73], [74] is one of the most used 8QAM constellations, but alternatives such as Circular-8QAM [9], 8PSK or Rect-8QAM have been also investigated [54]. When choosing a constellation, we are usually interested in the best sensitivity to noise. However, the constellation sensitivity depends on several factors such as the type of error correction code used as well as the constellation tolerance to phase noise. When accounting for these factors, the constellation with the highest minimum Euclidean distance may not be the one with the best sensitivity. In this section, I first investigate the impact of the constellation choice on carrier frequency and phase estimation algorithms. To illustrate the design choices, I experimentally compare [69] two constellations previously proposed in the literature, namely Circular-8QAM and Star-8QAM. Afterwards, the impact of the overhead of BICM-based FEC in constellation choice is evaluated. Experimental validation [70] is done by comparing two constellations, namely Rect-8QAM and Star-8QAM.

3.1.1 Circular-8QAM vs. Star-8QAM: Sensitivity and phase estimation

Star-8QAM has been widely used in optical communications. Unlike QPSK and 16QAM, for which square constellations and Gray mapping can be used, Star-8QAM is not compliant with Gray mapping. Several alternative 8QAM constellations have been proposed to improve noise tolerance of 8QAM modulation upon that of the Star-8QAM. Particularly, an alternative constellation named Circular-8QAM with appropriate bit mapping (quasi-Gray) has been recently shown [9] to outperform traditional Star-8QAM by 0.7 dB of optical signal to noise ratio (OSNR) at BER of $3.8 \cdot 10^{-3}$ and 28 GBd, this corresponds to the FEC limit of HD-FEC with 7% overhead [15]. Here, I extend this comparison by investigating the tolerance of the Circular-8QAM and Star-8QAM constellations against phase noise and frequency detuning. Moreover, using a standard single mode fiber (SSMF-) based transmission link without inline dispersion compensation, the non linear performance of both constellations is compared.

The constellations and corresponding bit-mappings are depicted in Fig. 3.1 (right). Theoretical performance using Monte Carlo simulation is also shown in Fig. 3.1 (additive white Gaussian noise is the only signal imperfection considered). This figure shows that Circular-8QAM provides 0.5 dB theoretical better sensitivity than Star-8QAM at $3.8 \cdot 10^{-3}$ BER, however this sensitivity gain is reduced for higher FEC BER limits (for example 10^{-2} typical for SD-FEC with 20% overhead). This result can be explained by slightly higher minimum Euclidean distance for Circular-8QAM as well as better bit-mapping. Note that Gray mapping is not possible for these constellations, however Circular-8QAM has an attractive property: the distance between neighbor symbols belonging to the ring (minimum Euclidean distance) is shorter than the distance between the central symbol and the others, therefore symbol errors are dominated by mistaking a symbol from the ring with its ring closest neighbors. The ring symbols can be easily bit-mapped in quasi-Gray fashion (among 7 ring neighbor transitions, 6 generate only 1 bit error and the remaining transition 2 bit errors). Another way for optimizing bit-mapping is fixing a signal-to-noise ratio and perform bit-mapping exhaustive search (i.e. testing all 8 factorial combinations) and select the mapping that minimizes the bit error rate. The bit-mappings shown in Fig. 3.1 and used in simulation and experiment were optimized for 10 dB of signal-to-noise ratio, corresponding roughly to SD-FEC limit of operation.

These analytical results assume perfect receiver knowledge of the absolute phase of the received signal in order to perform direct decoding (as opposed to differential decoding). Assuming the use of blind carrier phase estimation such as

blind phase search, there is a residual phase ambiguity after carrier phase compensation that can be compensated for by the introduction of pilot symbols (see section 2.3.4). Considering that we use pilot symbols with the same power for Star-8QAM and Circular-8QAM, to achieve the same absolute phase estimation performance in both cases we need more pilot symbols when using Circular-8QAM compared to Star-8QAM. These pilot symbols must be inserted frequently, since the absolute phase may vary over time due to cycle slips generated by un-wrapper block in carrier phase compensation stage. Therefore Circular-8QAM needs extra overhead reserved to pilots which negatively impact its noise sensitivity.

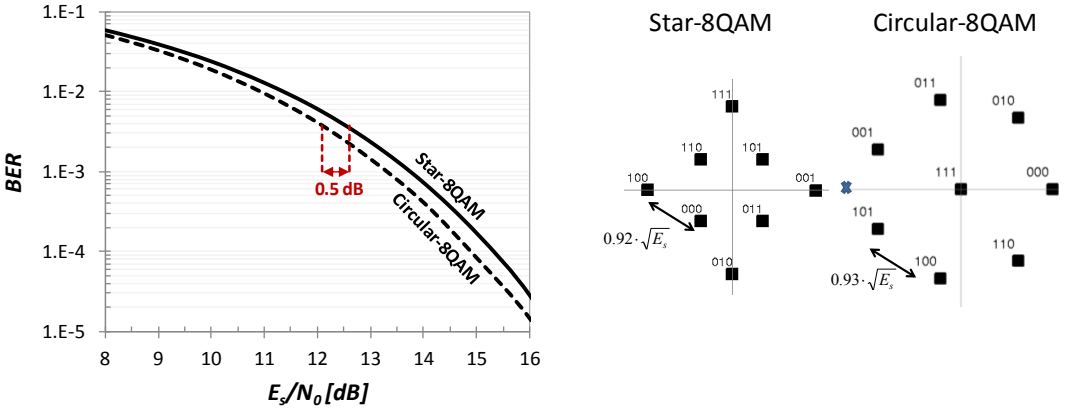

Fig. 3.1: Noise sensitivity (left).Star-8QAM and Circular-8QAM constellations and bit-mappings (right).

To quantify the difference between the required number of pilot symbols between constellations, we define K_{star} as the number of pilot symbols for Star-8QAM and K_{circ} the number of pilot symbols for Circular-8QAM. Using Eq. *2.50* from section 2.3.4 (approximation of symbol error probability of M-PSK), we can calculate the absolute phase estimation performance as a function of the SNR, rotational symmetry (S=4 for Star-8QAM and S=7 for Circular-8QAM) and number of pilots (K). To achieve the same estimation performance, we need to solve the following equation:

$$\sqrt{\frac{2K_{star}E_s}{N_0}} \cdot sin\left(\frac{\pi}{4}\right) = \sqrt{\frac{2K_{circ}E_s}{N_0}} \cdot sin\left(\frac{\pi}{7}\right). \tag{3.1}$$

We observe that the ratio between the number of pilots required by both constellations is given by:

$$\frac{K_{circ}}{K_{star}} = \left(\frac{sin\left(\frac{\pi}{4}\right)}{sin\left(\frac{\pi}{7}\right)}\right)^2 \approx 2.7 \tag{3.2}$$

Therefore, Circular-8QAM requires around 3 times more pilots for absolute phase estimation than Star-8QAM. Additionally, the ambiguity S impacts not only the blind carrier phase estimation block but also the blind carrier frequency estimation block. The popular carrier frequency estimation algorithm S^{th}-power periodogram can estimate frequencies from –R/(2S) up to R/(2S), where R is the symbol rate and S the constellation rotational symmetry (see section 2.3.3). Hence, Circular-8QAM is less tolerant than Star-8QAM to a offset between carrier and local oscillator by a factor of 7/4 which either increase requirements on accuracy of central frequency of signal and local oscillator lasers or require an extra algorithm with detuning tolerance beyond the one of S^{th}-power periodogram.

To experimentally validate these theoretical results as well as investigate the transmission performance of these two modulation formats, an experiment was performed. The symbol rate used is 41.6 GBd over a 50GHz grid and 20% overhead SD-FEC with 6 dBQ^2 threshold is assumed. Therefore both modulation formats are compared at the same information bitrate, 200 Gb/s, and the same spectral efficiency of 4 b/s/Hz. The experimental test-bed is depicted in Fig. 3.2 (a) and consists of one narrow line-width laser under test at 1545.72 nm, plus 63 loading channels spaced by 50 GHz. Pilot symbols are inserted according to a structure made of frames and sub-frames as depicted in Fig. 3.2 (b). For each frame we first insert a sequence that will be used for frame synchronization, then for each 400 symbol sub-frame we insert K pilot symbols that will be used for absolute phase estimation in the receiver. The number of pilots per sub-frame is flexible and slightly increases the symbol rate to ensure 200 Gb/s information rate. The resulting symbol sequences are oversampled to match the DAC sampling rate (65 GS/s) and pulse shaped using a root-raised cosine function with roll-off of 0.1.

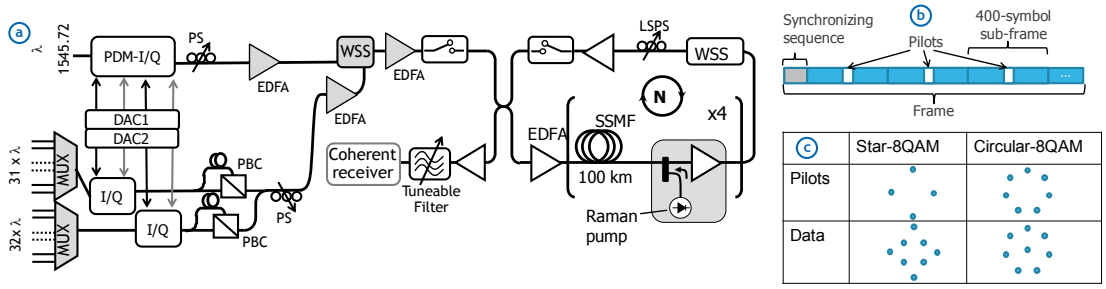

Fig. 3.2: a) WDM experimental setup. b) Frame structure used for pilot insertion. c) Constellations used for pilots and data symbols.

Loading channels separated into odd and even sets of channels, modulated independently with the same 8QAM format as the test channel using separate I/Q modulators, followed by polarization multiplexing emulation and polarization scrambling. The channel sets are spectrally combined through a wavelength

selective switch (WSS). The resulting multiplex is boosted through an erbium doped fiber amplifier (EDFA) and sent into the re-circulating loop consisting of four 100km-long spans of SSMF. No dispersion-compensating fiber is used here. Hybrid Raman-EDFA optical repeaters compensate fiber loss.

At the receiver side, the channel under test is selected by a tunable filter and sent into a polarization-diversity coherent mixer feeding four balanced photodiodes. Their electrical signals are sampled at 80GS/s by a real-time digital oscilloscope having a 33-GHz electrical bandwidth [1]. The offline digital signal processing performed on the stored waveform includes first chromatic dispersion compensation, then polarization de-multiplexing is realized using a 25-tap T/2 spaced butterfly equalizer with blind adaptation based on a multi-modulus algorithm. Frequency recovery is done using 4^{th} and 7^{th} power periodogram for the Star-8QAM and Circular-8QAM respectively. Phase recovery is done using blind phase search (BPS) algorithm for both constellations. For the Star-8QAM, BPS can be directly used by testing equally-spaced phases between [–π/4, π/4]. Since Circular-8QAM has a different constellation rotational symmetry (7), the test phases are in the range [-π/7, π/7]. The phase un-wrapper is modified to take the different constellation symmetries into account. After phase recovery, we synchronize the received sequence by doing a complex correlation with the frame synchronization sequence, followed by absolute phase estimation of each sub-frame by comparing the phase of the emitted and received pilot symbols. Each sub-frame is then multiplied by the estimated phase to enable the use of direct decoding. Decision is then done using the minimum distance and bit-error rate (BER) is counted and then converted to Q^2-factor.

We first investigated the impact of the different symmetry of these constellations onto the performance of pilot phase estimation. Fig. 3.3 (a) compares the distribution of normalized estimated pilot phase of the two modulation formats as a function of the number of pilots (K) at 14 dB of OSNR (measured at 0.1 nm), corresponding to $\hat{s}$ before rounding (Eq. *2.49* from section 2.3.4) Star-8QAM and Circular-8QAM respectively. Triangles show the phase distribution obtained for the Star-8QAM with 0.5% pilots (2 pilots per sub-frame). Diamonds and squares depict the distribution of phase for the Circular 8QAM with 0.5% and 1.5% pilots

[1] This setup based on recirculating loop and offline signal processing will be used in the rest of the thesis with a few changes that will be mentioned, so to improve readability later setup descriptions will be shorter. The main parameters that change are: fiber type (SSMF or large effective area pure-silica fiber), span length, optical amplification (EDFA-only or hybrid EDFA/Raman), number of channels, channel spacing, receiver parameters (80 GS/s with 33 GHz electrical bandwidth or 160 GS/s with 62.5 GHz electrical bandwidth).

respectively. Note that phase estimation error occurs when the modulus of normalized phase is bigger than 0.5 (shaded region in this figure). This figure shows that with the same amount of pilots (0.5%), the Star-8QAM exhibits a narrower normalized phase distribution than the Circular-8QAM, leading to less phase estimation errors. This figure also demonstrates that Circular-8QAM requires roughly three times more pilots than the Star-8QAM in order to achieve similar phase estimation performance as predicted by Eq. *3.2*. Thus, we consider for all the following results K=6 pilots (1.5%) for the Circular-8QAM and K=2 pilots (0.5%) for the Star-8QAM. Note that such an increase on pilot overhead corresponds to a symbol rate increase of 0.4 GBd, having negligible impact on OSNR sensitivity (0.04dB). Furthermore, in Fig. 3.3 (b), we investigated the impact of the frequency detuning in the performance of both formats at the same OSNR of 14 dB (at 0.1 nm). We can see in this figure that the Star-8QAM is more tolerant to the frequency detuning than the circular 8QAM, with a tolerance of ±5.2 GHz compared to ±3 GHz. The difference in tolerance with respect to frequency detuning is in line with theoretical expectations previously described.

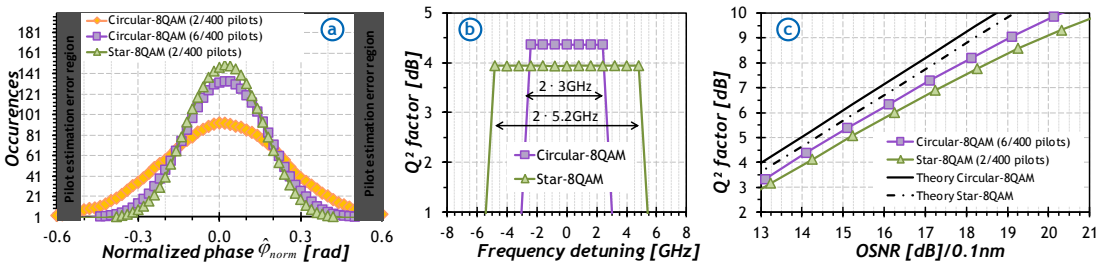

Fig. 3.3: a) Fitted distribution of normalized phases over 2600 sub-frames for both formats and for different number of pilots per sub-frame, b) frequency detuning tolerance and c) back-to-back performance results.

Afterwards, back-to-back performance versus the OSNR of the two studied formats is shown in Fig. 3.3 (c). We included as a reference theoretical performance of each modulation format under additive white Gaussian noise. The back-to-back performance of the Star-8QAM and Circular-8QAM are approximately 1 dB away from theory at 6 dB of Q^2-factor (corresponding to the limit of the 20% SD-FEC under consideration). Moreover, the Circular-8QAM format requires 0.4 dB at 6 dBQ^2 less power than the traditional Star-8QAM, which is in line with results obtained by Nölle et al [9].

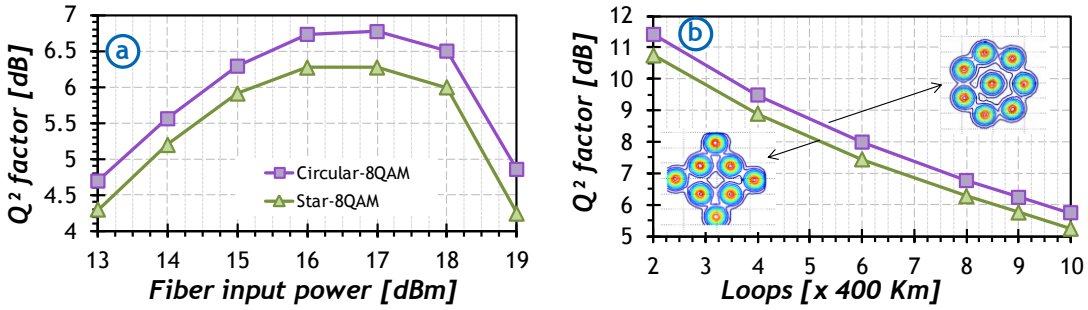

Fig. 3.4: Performance of the two solutions versus a) the launched power after 3200 km and b) distance.

Subsequently, we launched the 200 Gb/s channels into the loop. Fig. 3.4 (a) presents the performance measured by the Q^2-factor as a function of the fiber input power after 3200 km. This figure indicates the optimum launch power, which is approximately the same for the two examined formats, demonstrating similar non-linear tolerance for both of them. Then, we set the launch power to the optimum value of 17 dBm and we measured the Q^2-factor as a function of distance. Fig. 3.4 (b) shows the measured performance of each modulation format versus the number of loop round trips. This figure confirms that the performance advantage of the circular format observed in back-to-back holds even after long distance transmission, making it a promising constellation for increasing the distance of long-haul dispersion unmanaged systems, despite needing a higher pilot overhead for absolute phase estimation and the lower tolerance to frequency detuning.

This result highlights that the extra penalties due to its lower tolerance to phase impairments are not sufficiently high to overcome Circular-8QAM theoretical advantage. The fact that lasers with stable phases are widely available and that we can use very high symbol rates (positive impact on phase impairment tolerance) limit the implementation penalty of Circular-8QAM. Furthermore, at first sight we could expect that Circular-8QAM might have an extra penalty after transmission due to its high power fluctuation (transitions to and from the symbol in the center). However since we operate in a highly dispersive regime (transmission link without inline compensation), the transmitted signal rapidly becomes Gaussian thus reducing the impact of symbol transitions. Additionally, uncompensated links do not add fast phase shifts which would degrade Circular-8QAM performance. Therefore, Circular-8QAM might provide an attractive solution for systems using 3 bits per symbol per polarization modulation formats. However, a complete comparison should also take into account the impact of realistic channel coding techniques, which is discussed in next section.

3.1.2 8QAM constellations: Sensitivity vs BICM-based FEC overhead

A more complete comparison between 8QAM modulation formats should not only consider BER sensitivity and phase noise tolerance, but also other performance metrics. For example, minimum Euclidean distance and constellation constrained capacity are other metrics often used to compare the performance of different constellations [54], however these two metrics do not fully account for realistic channel coding implementation which is an essential system block. Current optical communications systems usually rely on pragmatic bit-interleaved coded modulation (BICM) channel coding schemes [75] which are advantageous since low complexity binary codes are used as opposed to non-binary ones which are inherently more complex. To further reduce complexity, iterative demapper is usually avoided to reduce the number of decoder iterations. Fig. 3.5 depicts a typical BICM setting, where the binary output of the encoder is interleaved prior to be modulated. Such a setting advantageously offers a convenient trade-off between performance and hardware implementation complexity compared to iterative demapping solutions.

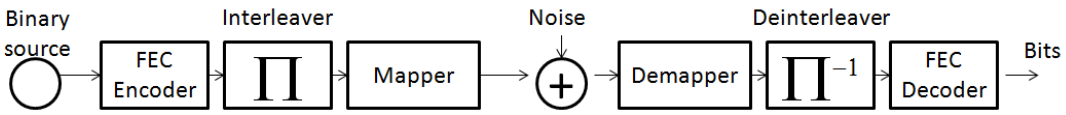

Fig. 3.5: BICM setup without iterative demapping.

When employing BICM without iterative de-mapper, there is a significant impact of labeling on performance which cannot be quantified if we restrict the analysis to minimum Euclidean distance and constellation constrained capacity. To quantify the labeling impact on maximum achievable capacity of BICM systems without iterative de-mapper, the generalized mutual information can be used [76]. In this section, I compare different 8QAM constellations in terms of generalized mutual information and I show which constellation should be used to maximize capacity as a function of signal-to-noise ratio. These results were first shown in [70].

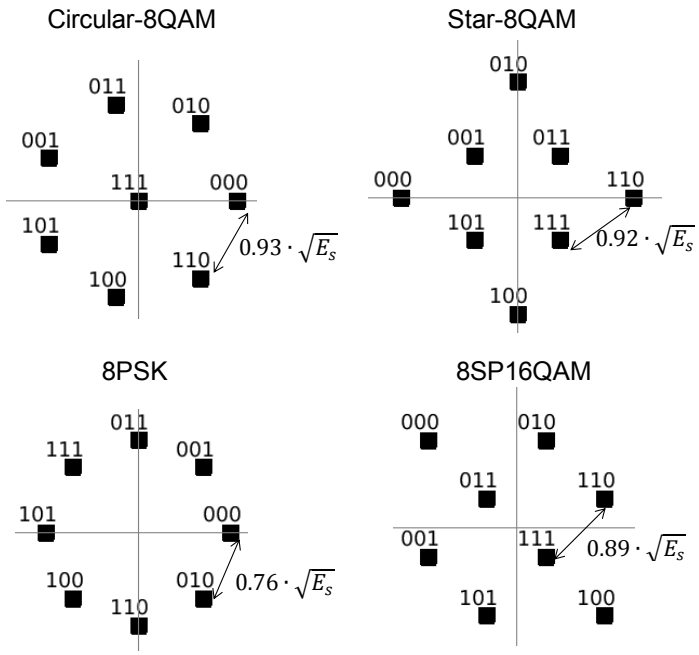

Fig. 3.6: Modulation formats. Non-Gray mapping (Star-8QAM and Circular-8QAM) and Gray mapping (8PSK)

First, we define the constellations and mappings of the studied solutions. Fig. 3.6 and Fig. 3.7 shows the four studied constellations: three of them cannot have Gray mapping (Star-8QAM, Circular-8QAM and 8SP16QAM) and the remaining ones have straightforward Gray mapping (8PSK and Rect-8QAM). Contrary to 8PSK, Rect-8QAM has different average power on in-phase (I) and quadrature (Q) component, thus requiring I/Q power ratio (PR in Fig. 3.7) adjustment for performance optimization. We also included the recently proposed Hybrid-QPSK/16QAM solution [77]. However, Rect-8QAM is theoretically equivalent to Hybrid-QPSK/16QAM as shown in Fig. 3.7. The hybrid approach is based on interleaving QPSK and 16QAM symbols to achieve the same average number of bits-per-symbol as 8QAM. Every 6-bit block, 2 bits will modulate a QPSK symbol in an even time slot and the remaining 4 will modulate a 16QAM symbol in an odd time slot, leading to an average of 3 bits per time slot. It can also be seen as 6 bits to be transported in four dimensions: two time slots with two dimensions per time slot. Each dimension is coded in the following way: I_{even} (2-PAM, 1 bit), Q_{even} (2-PAM, 1 bit), I_{odd} (4-PAM, 2 bits) and Q_{odd} (4-PAM, 2 bits). Simply switching Q_{even} with I_{odd}, a Rect-8QAM constellation is obtained in both time slots. From now on, only Rect-8QAM will be used, but the results can also apply to the hybrid format.

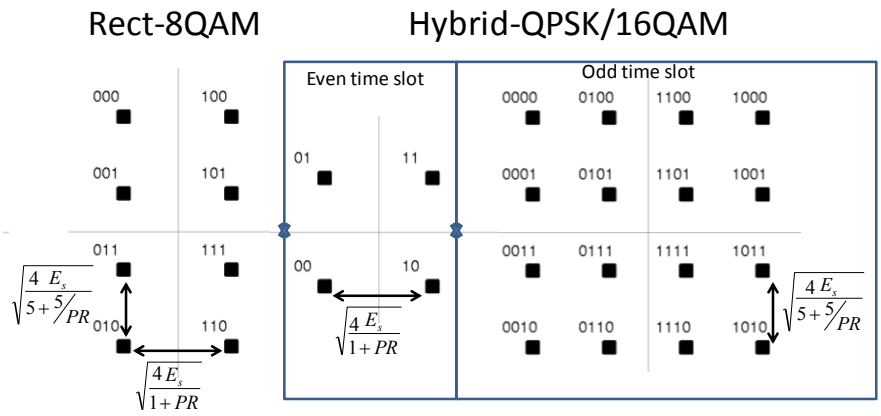

Fig. 3.7: Modulation formats. Gray mapping (Rect-8QAM and Hybrid-QPSK/16QAM).

In Fig. 3.6 and Fig. 3.7, we also included the Euclidean distance to the closest neighbor as a function of the square root of the average symbol energy (E_s). Circular-8QAM appears as the most power efficient of the studied solutions with Euclidean distance equal to $0.93 \cdot E_s^{1/2}$ followed by Star-8QAM with $0.92 \cdot E_s^{1/2}$, 8SP16QAM with $0.89 \cdot E_s^{1/2}$, Rect-8QAM with $0.82 \cdot E_s^{1/2}$ (by choosing 7dB as power ratio) and 8PSK with $0.76 \cdot E_s^{1/2}$. To compare the possible 8QAM constellations beyond minimum Euclidean distance, we can use two additional metrics: the constellation constrained capacity (derived from mutual information defined in section 1.2.3) as a reference upper bound, representing the maximum number of information bits per symbol that we can be transported using an optimal soft-decision error correction code for a given signal-to-noise ratio (SNR); and, the bit-wise constellation constrained capacity (derived from generalized mutual information also defined in section 1.2.3), that is more realistic by considering the use of an optimal soft-decision BICM error correction code (Fig. 3.5).

Now, we compare the constellation constrained capacity (MI) and bit-wise constellation constrained capacity (GMI) for each format. Fig. 3.8 now shows the MI (solid lines) and GMI (dashed lines) for each format versus SNR per bit (E_b/N_0). We used the straightforward Gray bit mapping for Rect-8QAM and 8PSK. Then, the bit mapping of Circular-8QAM, 8SP16QAM and Star-8QAM were optimized to maximize the GMI at signal-to-noise ratio of 7.5 dB among the 40320 (8!) possible label combinations. Considering only the MI curves for constrained capacity, Circular-8QAM is found to be the best constellation among the studied formats owing to its highest minimum Euclidean distance (2a – solid line).

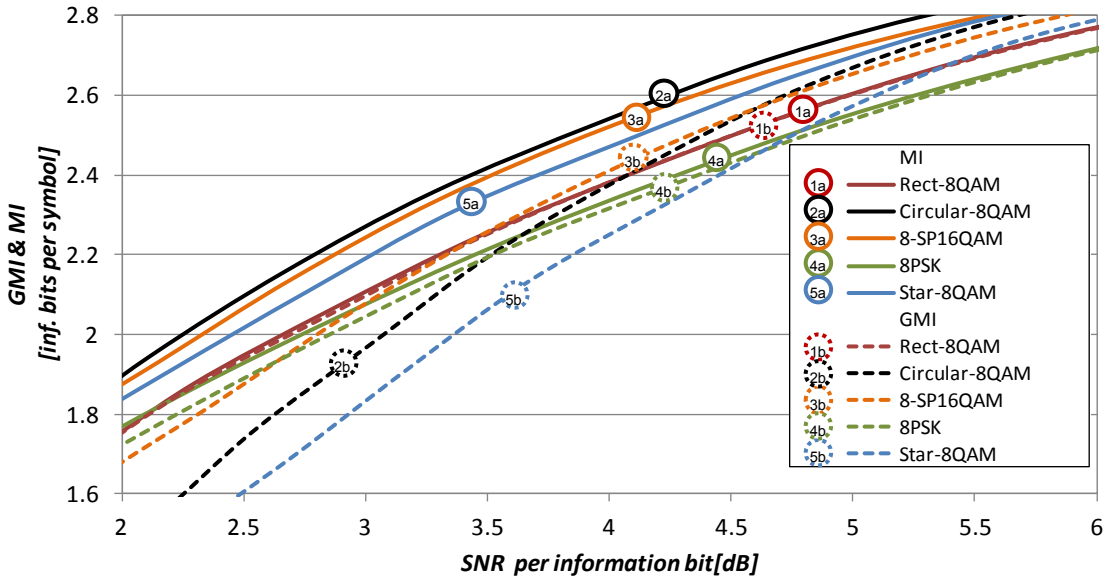

Fig. 3.8: Mutual information (a, solid) and generalized mutual information (b, dashed).

Note that to improve the performance of Rect-8QAM, we optimized the power ratio between the quadrature and in-phase signal to maximize the GMI for each SNR as shown in Fig. 3.9.

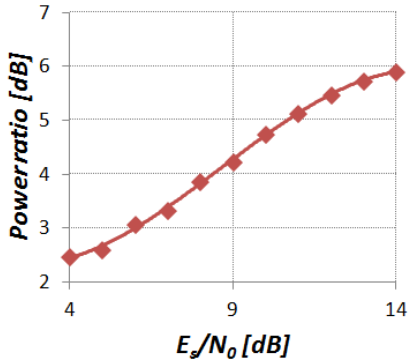

Fig. 3.9: Optimization of power ratio between quadrature and in-phase components of Rect-8QAM constellation as a function of signal-to-noise ratio to maximize the generalized mutual information.

Then, we compare the penalty coming from the BICM setting, the difference between MI and GMI for each format in Fig. 3.10. We observe that penalty is negligible for high SNR but it increases for low SNR. Additionally, this penalty can reach more than 0.15 information bit/symbol for two of the non Gray-mapped formats (Circular- and Star-8QAM), while being much smaller (<0.05 inf. bit/symbol) for formats with Gray mapping (Rect-8QAM and 8PSK). 8SP16QAM has an intermediate penalty of around 0.1 inf. bit/symbol for low SNR.

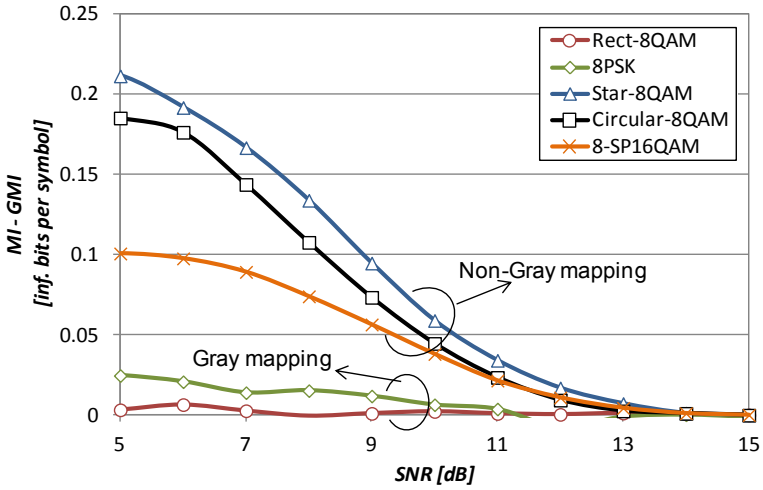

Fig. 3.10: Achievable information rate loss with respect to constellation constrained capacity due to bit-wise processing (MI minus GMI for each format).

Then, we compare the tested formats using the GMI as performance metric. To improve clarity, Fig. 3.11 shows the results expressed in GMI penalty of each tested format with respect to the MI of Circular-8QAM (best constellation using MI metric). Three distinct regions with a different optimal format are observed. When GMI is higher than 2.6, corresponding to high code rate region, Circular-8QAM provides an advantage over the other formats (minimize GMI penalty). For GMI between 2.3 and 2.6, 8SP16QAM is the best format. For GMI below 2.3, Rect-8QAM outperforms Circular-8QAM, Star-8QAM and 8SP16QAM thus highlighting the key role of Gray mapping in the low code rate region. As low code rate FEC (high overhead) may be required to further increase transmission reach in long haul transmission systems, this result demonstrates the high interest of Gray-mapped formats for BICM implementations even though they are outperformed by other formats when considering the constellation constrained capacity or minimum Euclidean distance as performance metric. This may be of particular interest for systems carrying an odd number of bits per 2D-symbol where Gray-mapped square-like constellations are not available.

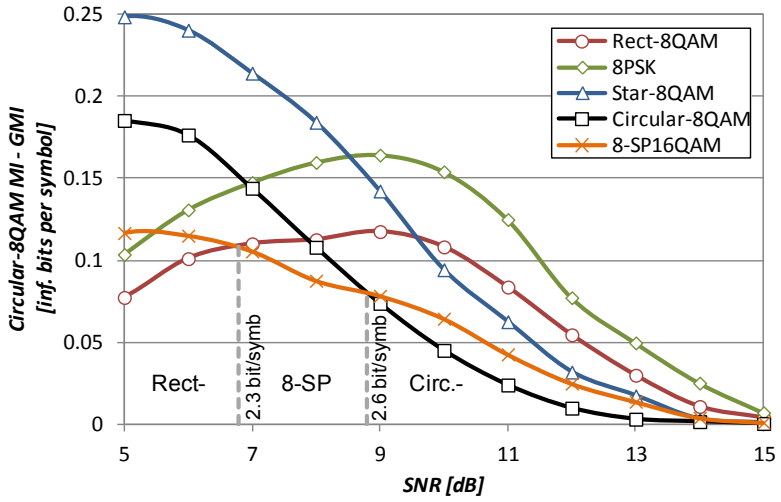

Fig. 3.11: Achievable information rate loss with respect to Circular-8QAM constellation constrained capacity for each format with bit-wise processing (Circular-8QAM MI minus GMI for each format).

To demonstrate the impact of the coding scheme in format comparison, we generated and tested Star-8QAM and Rect-8QAM using a high-speed DAC in a back-to back configuration. A 41.6 Gbaud signal with root-raised-cosine pulse shaping and roll-off factor of 0.1 was generated with the same setup described in last section (3.1.2). Fig. 3.12 (left) shows the estimated GMI as a function of optical SNR (OSNR) for both formats. Diamonds and triangles represent Rect-8QAM and Star-8QAM respectively. Theoretical expectations are included as solid and dashed curves without markers for Rect- and Star-8QAM, respectively. For OSNR higher than 15 dB, both formats can transport roughly the same number of bits. However for lower OSNR, Rect-8QAM outperforms Star-8QAM by 0.4 dB. Fig. 3.12 (right) shows the post-FEC BER as a function of the OSNR in the waterfall region for a BICM-SC-LDPC FEC implementation [8] using two different code rates r (0.65 and 0.85). With r = 0.85, both formats have similar FEC OSNR limit, but with r = 0.65 Rect-8QAM has 0.4 dB OSNR advantage with both theoretical and experimental curves shown in Fig. 3.12 (left). Theoretical results were validated by back-to-back experiment with dual-rate BICM FEC and it is also shown that GMI can be accurately used to predict modulation format sensitivity difference after FEC. These results may be of particular interest for systems relying on low code rate BICM FEC implementations without iterative demapping. Note that, for other FEC implementations the GMI may not be the best metric for performance prediction. For example, for soft-decision non-binary FEC implementation defined over a finite (Galois) field GF(2^3), the correct metric would be the mutual information [78], however these non-binary codes have higher implementation complexity.

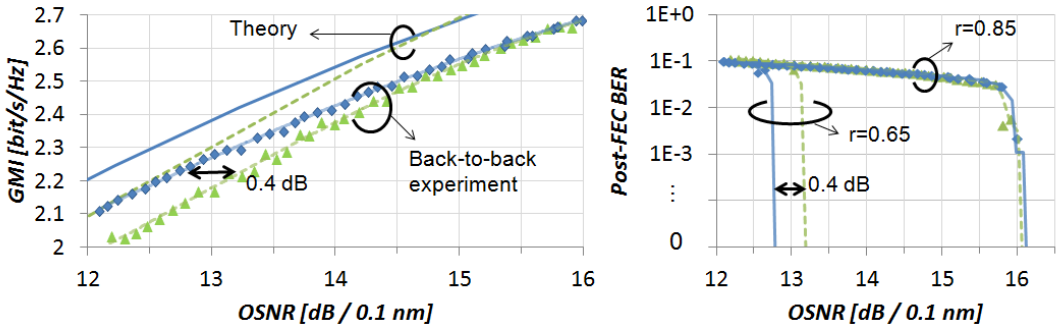

Fig. 3.12: GMI (left) and post-FEC BER (right) using two code rates for experimental Star-8QAM (triangles) and Rect-8QAM (diamonds)

3.2. *Time-interleaved hybrid modulation vs 4D-modulation*

In this section, time-interleaved hybrid formats and 4D-modulation formats are investigated. Both these solutions can be used to fine tune the optical system spectral efficiency thanks to more degrees of freedom compared to classical M-QAM systems. First, in section 3.2.1 and 3.2.2, time-interleaved modulation formats and 4D-modulation formats are briefly described, respectively. Particularly, it is shown that both solutions can provide intermediate spectral efficiency between traditional M-QAM formats. Such a flexibility will likely be one of main the requirements of future optical communication systems to improve resource utilization. In section 3.2.4, an experimental comparison at 2.5 bits per symbol per polarization is performed to validate these ideas. Note that, 2.5 bits per symbol per polarization cannot be implemented using classical M-QAM solutions. Finally, in section 3.2.5, we show that 4D modulation formats can also be used improve receiver power sensitivity in short reach intensity modulation direct detection systems based on 4PAM modulation.

3.2.1 Time-interleaved hybrid modulation

The main idea of hybrid modulation formats is interleaving symbols from two different constellations in time or polarization to achieve an intermediate number of bits compared to the cases where we use only one of the constellations. The exact number of bits per symbol of a hybrid signal depends on the proportion of symbols from each constellation and the sensitivity depends on the percentage of total power reserved for each constellation. To calculate the performance of hybrid signals, it is necessary to calculate the signal-to-noise ratio experienced by each constellation. For the general case where we interleave two constellations (namely A and B), the signal-to-noise ratio of the hybrid signal can be written as:

$$SNR = \frac{E_s}{N_0} = \frac{p \cdot E_s^A + (1-p) \cdot E_s^B}{N_0} \tag{3.3}$$

where E_s^A is the average symbol energy of the interleaved constellation A used with ratio p (0<p<1) and E_s^B is the average symbol energy of the remaining interleaved constellation B with the ratio (1-p). The ratio p can be achieved by creating blocks of symbols. For example, for p=0.4, we can use a block of length 5 where two symbols belong to constellation A and three symbols to constellation B. So to evaluate the SNR experienced by each constellation we obtain:

$$SNR^A = \frac{E_s^A}{N_0} = \frac{SNR}{p + (1-p) \cdot PR}, SNR^B = \frac{E_s^B}{N_0} = \frac{SNR}{{}^{p}/_{PR} + (1-p)} \tag{3.4}$$

where we define the power ratio (PR) between constellations as.

$$PR = \frac{E_s^B}{E_s^A} \tag{3.5}$$

The PR should be optimized either to maximize performance or to comply with digital signal processing limitations. A pragmatic solution to maximize performance is to minimize the bit error rate (BER). The BER of hybrid modulation formats can be simply calculated as:

$$BER = \frac{p \cdot BER^A \cdot bps^A + (1-p) \cdot BER^B \cdot bps^B}{bps^A + bps^B} \tag{3.6}$$

where bps^A and bps^B are the number of bits per symbol of the constellation A and B, respectively. For example, if we want to transport 2.5 uncoded bits per symbol, we could interleave QPSK with 8QAM (bps^A=2 and bps^B=3, respectively) using the ratio p=0.5. That can be easily achieved by sending QPSK in even time slots and 8QAM in odd time slots, which is equivalent of having a block (frame) of size two where each symbol belongs to one constellation.

To evaluate the BER performance of time-interleaved formats, three cases are investigated: Hybrid-BPSK/QPSK, Hybrid-QPSK/8QAM and Hybrid-8QAM/16QAM. For the three scenarios the ratio is set to 50% (p=0.5) representing even/odd interleaving. Power ratio between interleaved constellations is set to 2 dB and the higher-order constellation is always the most powerful among the two interleaved ones. The results are shown in Fig. 3.13 where performance of BPSK, QPSK, 8QAM (Star-) and 16QAM are included. The right table summarizes the formats compared in terms of number of bits per symbol and minimum Euclidean distance. We observe in the figure that the modulation choice is a clear trade-off between capacity and noise sensitivity. Furthermore, hybrid modulation can provide intermediate solutions in terms of noise sensitivity and capacity between the more

common modulation formats, hence improving on the granularity of spectral efficiency and having the potential to be used to make transponders more flexible.

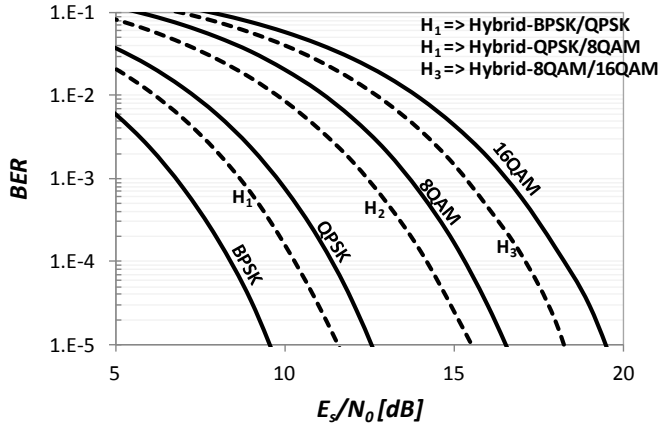

Format	Bits per symbol	d_{min}
BPSK	1	2
Hybrid-BPSK/QPSK	1.5	1.57
QPSK	2	1.41
Hybrid-QPSK/8QAM	2.5	0.99
8QAM	3	0.89
Hybrid-8QAM/16QAM	3.5	0.70
16QAM	4	0.63

Fig. 3.13: BER vs SNR for hybrid modulation formats.

3.2.2 4D-modulation formats

Another way to improve the granularity of spectral efficiency is the use of multi-dimensional modulation. One of the simplest cases of multi-dimensional modulation formats is the case where symbols are defined in the 4D space represented as the in-phase and quadrature component of two orthogonal polarizations. By restricting the modulation order M to a power of 2, we can create constellations with M points in the 4D space resulting in granularity improvement of spectral efficiency. The bit per symbol per polarization granularity of traditional PDM-MQAM systems is 1 bit per symbol per polarization, whereas 4D modulation granularity is improved to 0.5 bit per symbol per polarization. If the time dimension is also considered, arbitrary N dimensional modulation can also be achieved resulting in even finer granularity at the expense of increased complexity.

By setting the modulation order M to a specific value, we need a way to choose the positions of the constellation points in the 4D space. One first optimization would be choosing the positions that maximize the constellation minimum Euclidean distance. It turns out that the problem of finding the M point constellation in N-D space with the largest minimum Euclidean distance is equivalent to the problem of finding the densest packing of M N-dimensional spheres [79] which is a challenging problem to solve analytically. However, numerical methods can be used to find dense constellations generally without guarantees that the packing is the densest [80]. Fortunately, it is known that constellations defined as spherical subsets of densest lattices in a given dimension approach the optimum constellations when M is large. Additionally, the underlying structure of lattices can be leveraged to reduce modulation and demodulation complexity.

A lattice in 4 dimensions that can be easily constructed is the cubic lattice which contains points with integer coordinates in each of the 4 dimensions. The popular modulation formats based on square constellations PDM-QPSK, PDM-16QAM, PDM-64QAM are a cubic subset of the cubic lattice. However, the densest lattice in 4 dimensions is the D_4 lattice, which can be simply defined as all points having integer coordinates in every dimension provided that the sum of every coordinate is an even number. Therefore, a simple way to find dense M-point constellations in 4-dimensions with better power efficiency compared to square QAM constellations is choosing a spherical subset of the D_4 lattice. Since spherical subsets are challenging to implement in practice, a cubic subset of M points of D_4 lattice can also be used with slightly lower power efficiency than the spherical subset resulting in the formats [79]: 8-SP-QAM (or PS-QPSK), 32-SP-QAM, 128-SP-QAM, etc with SP standing for set-partitioning. These formats have been widely studied by the optical community including:[79], [81], [82], [56], [83], [84]. SP formats are attractive for their power efficiency and also for the implementation simplicity since their constellation points are a subset of PDM squared QAM formats. For example, PDM-16QAM has 256 states in the 4D space and 128-SP-QAM can be constructed by simply choosing 128 of these points corresponding to a valid subset of the D_4 lattice.

These modulation formats can be easily constructed by reusing bit-to-symbol mappers designed for the modulation formats QPSK and 16QAM as shown in Fig. 3.14 [82].

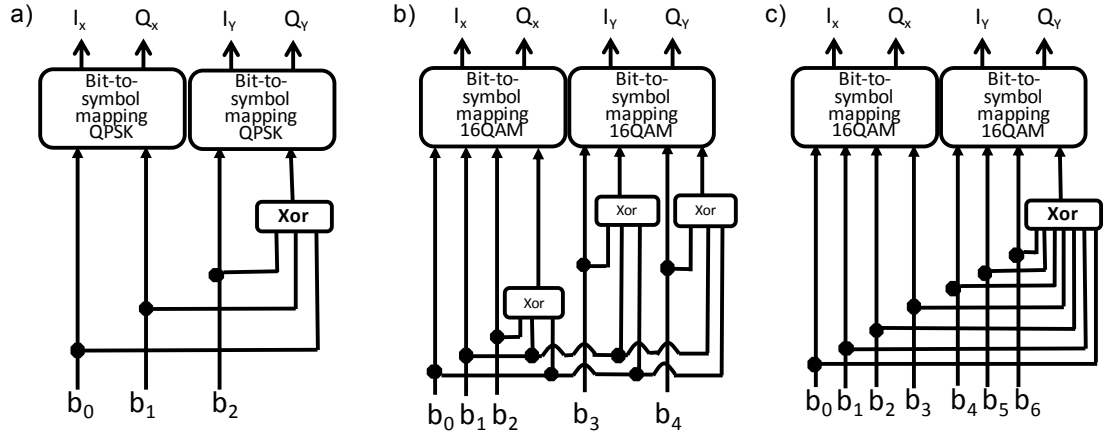

Fig. 3.14: Schematic description bit-to-symbol mapper for PS-QPSK (a), 32-SP-QAM (b) and 128-SP-QAM.

The performance of these formats can be observed in Fig. 3.15 where we calculate the BER as a function of SNR. Performances of BPSK, QPSK, 8QAM and 16QAM are included for reference. Minimum Euclidean distance for each candidate format is also showed in the table and it is interesting to see that 8-SP-QAM (resp. 128-SP-QAM) has the same d_{min} as BPSK (resp. 8QAM) despite transporting more

bits per symbol. This is a result of the use of denser lattice. We can also observe that the BER performance of 4D formats lies in between the performance of typical modulation formats, showing that 4D modulation can also be used to improve transponder granularity in terms of spectral efficiency.

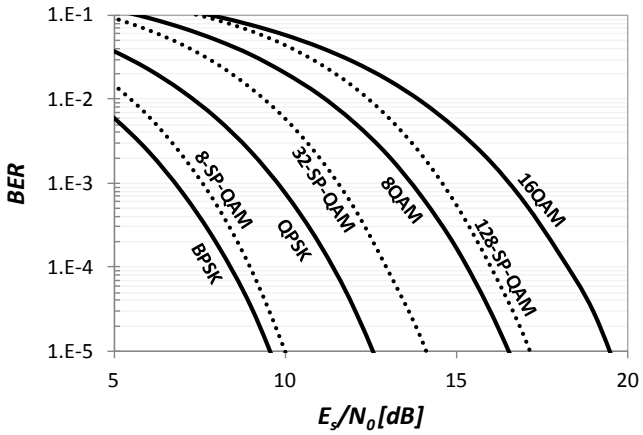

Format	Bits per symbol per pol.	d_{min}
BPSK	1	2
8-SP-QAM	1.5	2
QPSK	2	1.41
32-SP-QAM	2.5	1.26
8QAM	3	0.89
128-SP-QAM	3.5	0.89
16QAM	4	0.63

Fig. 3.15: BER vs SNR for 4D modulation formats with 2D formats as reference.

3.2.3 4D vs. Hybrid using mutual information

As it was shown in Section 3.2.1 and 3.2.2, both hybrid modulation formats and 4D modulation formats can be used to better match spectral efficiency with transmission distance. Such solutions may complement conventional PDM QAM-based solutions to deliver the optimum system capacity for the distance to be covered.

To compare which solution is the most attractive, taking into account FEC implementation is necessary as shown in Section 3.1.2. For example considering pragmatic BICM SD-FEC schemes, the generalized mutual information is the most appropriate metric to quantify the modulation achievable information rate [76], [85]. In this section, we provide one example of comparison between a 4D modulation format and a time-interleaved modulation format at the same number of bits per symbol. Here, we pick the 4D-32SPQAM that carries 2.5 bits/symbol/polarization and Hybrid-QPSK/8QAM that also carries 2.5 bits/symbol/polarization. For the hybrid format, we divide the transmitted sequence in odd and even symbols. At even time slots, QPSK symbols are transmitted and at odd time lots Star-8QAM symbols are transmitted. We set the power ratio to 3.74 dB resulting in QPSK symbols with the same average energy as the inner ring symbols of the 8QAM constellation. This property can be exploited by the receiver DSP to recover the transmitted information more easily as the received signal has only two amplitude levels.

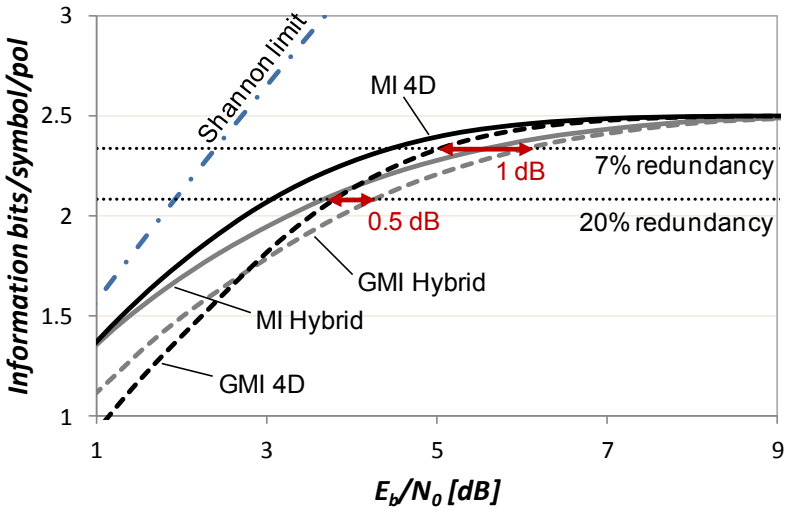

Fig. 3.16: Mutual information and generalized mutual information for Hybrid-QPSK/Star-8QAM with 3.8 dB power ratio and 4D-32SPQAM.

Fig. 3.16 shows the comparison of the two modulation formats in terms of mutual information and generalized mutual information as a function of SNR per information bit, depicted as solid lines and dashed lines, respectively. We observe that both formats saturate at 2.5 bits/symbol/polarization. Then, considering just the mutual information as performance metric, the 4D format outperforms the hybrid solution thanks to its higher Euclidean distance. For the generalized mutual information comparison, we observe a different behavior with respect to the mutual information analysis. At 2.33 information bits per symbol per polarization, equivalent to 7% redundancy reserved to an ideal soft-decision channel coding, the 4D solution requires around 1 dB less SNR compared to the hybrid solution. However, as we increase the redundancy the gap reduces (to 0.5 dB at 20% redundancy) and eventually there is a crossing point and above that the hybrid solution provides the best solution thanks to the labeling. Note that this crossing point may be optimized as a function of the targeted information rate as it depends on several parameters such as considered modulation format, labeling and power ratio. For example, when targeting a low information rate, a more adapted choice of the 8QAM constellation (Rect-8QAM from results obtained in section 3.1.2) would help improving performance of Hybrid solution.

3.2.4 Experimental comparison at 2.5 bit/symbol/pol

Here, both solutions, namely the 4D-32SP16QAM (32SPQAM in last section) and Hybrid-QPSK/8QAM formats, are implemented experimentally and their performance is compared at the same bit rate and spectral efficiency using a

standard single mode fiber (SSMF-) based transmission link. The two different modulation formats were operated at 31.2 GBd over a 33GHz-grid and 20% of error correction code was assumed. Therefore we compare both modulation formats at the same information bit-rate, 125 Gb/s, and the same spectral efficiency of 3.75 b/s/Hz. To generate the 4D-32SP-16QAM format, we use the same setup as the one detailed in section 3.2.2. In short, this format is based on a 4D set-partitioning scheme, consisting in selecting a subset of 32 states out of the 256 possible states from a dual-polarization 16-QAM constellation. This subset is chosen to increase the minimum Euclidean distance and thus the tolerance to noise, while reducing the number of bits per 4D-symbol from 8 to 5. To generate the hybrid format, we combine QPSK and 8QAM symbols with identical Euclidean distance (corresponding to a power ratio of 3.74 dB) to simplify the signal processing at the receiver side since received symbols have only 2 amplitudes. We chose to interleave in time and polarization the QPSK and 8QAM symbols leading to a constant power signal as shown in Fig. 3.17.

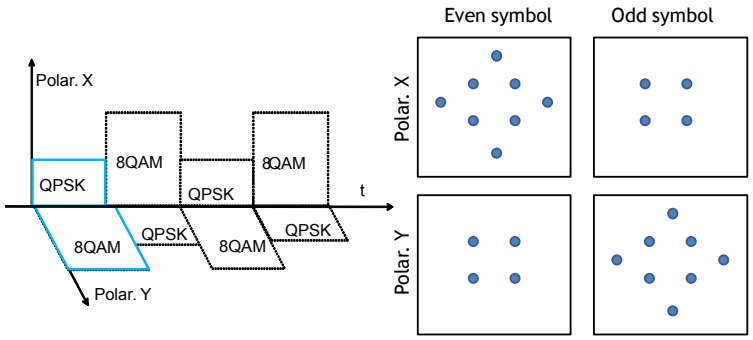

Fig. 3.17: Schematic description of the Hybrid-QPSK/8QAM format.

Our test-bed consists of twelve narrow linewidth lasers spaced by 33 GHz, plus 50 loading channels spaced by 50 GHz and PDM-QPSK modulated at 31.2 GBd. As depicted in Fig. 3.18 (a), the twelve narrow linewidth lasers spaced by 33 GHz are separated into odd and even sets of channels which are modulated independently and interleaved spectrally. The light from these lasers is sent into I-Q modulators driven by a pair of digital-to-analog converters (DAC) operating at 65-GS/s. Polarization multiplexing for the hybrid format is then performed by dividing, decorrelating and recombining the generated data through a polarization beam combiner (PBC) with an approximate 10-ns delay, yielding 156 Gb/s data rate.

The description of the loop as well as the receiver depicted in Fig. 3.18 (b) is the same as the ones described in Section 3.1.1. The digital signal processing includes first a channel skew adjustment. After chromatic dispersion compensation, polarization demultiplexing is realized using a 25-tap T/2 spaced butterfly equalizer with blind adaptation based on a multi-modulus algorithm. Frequency and carrier

phase recovery are then recovered. For the hybrid format, we separate the streams of QPSK and 8QAM symbols before symbol decision and for the 4D format, we use four-dimensional minimum distance detection. The resulting data are finally decoded and bit errors are counted to provide a BER measurement which is later converted to Q^2-factor.

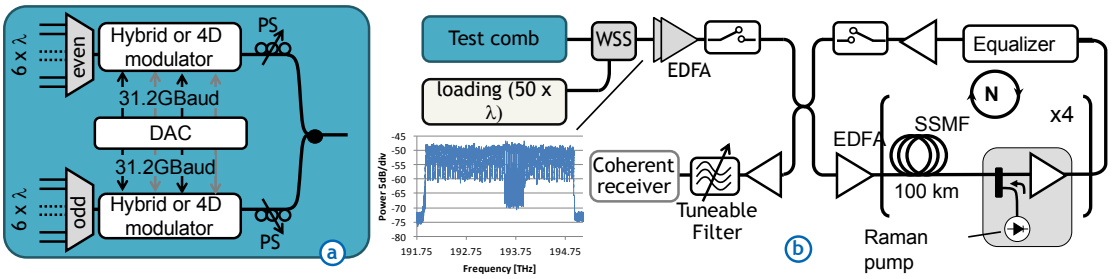

Fig. 3.18 Experimental setup for WDM transmission: (a) modulation scheme for the test comb spaced by 33 GHz with 25-GBd 4D-32SP-16QAM and Hybrid-QPSK/8QAM, (b) Transmitter scheme involving loading channels and recirculating loop.

We first evaluated the back-to-back performance versus the optical signal-to-noise ratio (OSNR) of the two studied formats, 31.2 GBd 4D-32SP-16QAM and Hybrid-QPSK/8QAM. Fig. 3.19 shows the measured Q^2-factor versus OSNR. We included as a reference in this figure theoretical performance of each modulation format under additive white Gaussian noise. The back-to-back performances of the 4D-32SP-16QAM and Hybrid-QPSK/8QAM are approximately 1 dB away from theory at 7 dB of Q^2-factor but this gap increases for higher Q^2-factors especially for the Hybrid-QPSK/8QAM. At 10 dB of Q^2-factor, the hybrid format has an OSNR penalty compared to theory of almost 2 dB while the 4D penalty is about 1.2 dB.

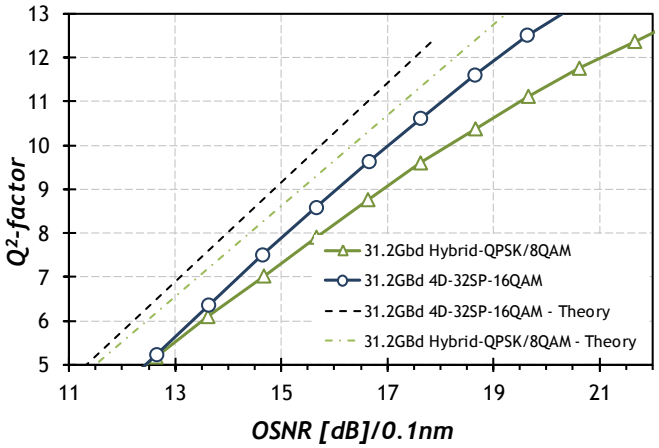

Fig. 3.19: Noise sensitivity of the studied modulation formats

We then launched the 31.2 GBd channels into the loop. Fig. 3.20 presents the performance measured by the Q^2-factor as a function of the launched power after

2400 km and 4800 km. This figure indicates the optimum launching power, which is approximately the same for the two examined formats, demonstrating similar non-linear tolerance for both of them. Fig. 3.20 shows that after 2400 km and 4800 km the difference of Q^2-factor is about 1 dB and 0.5 dB respectively, considering the optimum launching power of 16 dBm. These confirm that both modulation formats have similar performances at long distances (low OSNR), even though the 4D-32SP-16QAM still outperforms the Hybrid-QPSK/8QAM for short distances.

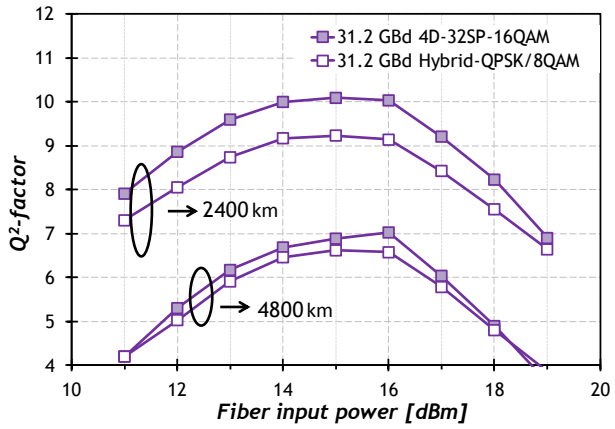

Fig. 3.20: Performance of the two modulation formats as a function of the launched power and distance.

Subsequently, we set the launched power into the fiber to the optimum value and we measured the Q^2-factor for a range of distances. Fig. 3.21 shows the measured performance of each modulation format for various distances spaced by 800 km. We included performance of PDM-QPSK and PDM-8QAM at the same baud-rate to show that both the Hybrid-QPSK/8QAM and the 4D-32SP-16QAM provide an intermediate reach between them. At 8 dB of Q^2-factor, the reach of the 4D-32SP-16QAM is 0.7 dB longer than the Hybrid-QPSK/8QAM. Considering a low Q^2-factor of 6 dB, the correction threshold for the considered 20% overhead soft decision FEC, the 4D-32SP-16QAM still slightly outperforms the Hybrid-QPSK/8QAM. This difference tends to vanish as Q^2-factor decreases, and the hybrid format eventually outperforms the 4D at low Q^2-factor (below 4 dB), thanks to better bit labeling (in line with Section 3.2.3). However when considering FEC limit above 6 dBQ^2, the 4D solution appears as the best-suited solution to provide intermediate reach and SE between the PDM-QPSK and the PDM-8QAM. Hence, at 8 dB of Q^2-factor, the 4D-32SP-16QAM reach is 3 dB longer than the PDM-8QAM while decreasing the SE from 4.5 to 3.75 b/s/Hz, and 2.3 dB shorter than the PDM-QPSK (3 b/s/Hz).

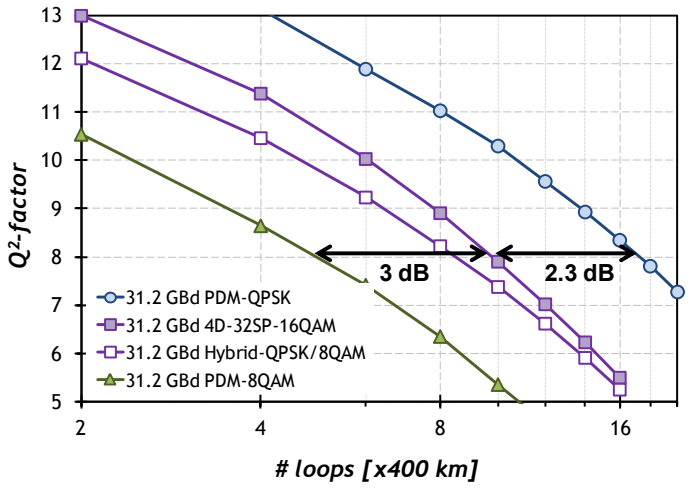

Fig. 3.21: Performance of the four modulation formats as a function of the distance

These results show that transponder flexibility can be achieved using different strategies. Here we focused on the strategy were the symbol rate and FEC overhead are fixed. The remaining degree of freedom that is used is the change of modulation format. Although this strategy is not optimal from a performance perspective, this strategy has some implementation advantages compared to other alternatives such as having several FEC overheads or several symbol rates. Implementing more than one FEC overhead in an integrated circuit is challenging since FEC is already one of the blocks that occupies most chip area. Furthermore, the implementation of several symbol rates in a single transponder also makes the system more complex. The strategy of having several modulation formats with different number of bits per symbol can also be implemented in different ways. Here we presented two of them. The use of 4D modulation formats is one of the alternatives and its main advantage is the better performance of these formats since they are optimized in a higher dimensional space. The other alternative is time-interleaved modulation formats which despite having slightly lower performance provide a simple and flexible way to achieve arbitrary granularity. Multi-dimensional modulation formats, on the other hand, rely on increasing the number of dimensions used to achieve arbitrary granularity which increases slightly implementation complexity. Therefore, the choice between these two alternatives will depend on design goals, mainly a trade-off between implementation complexity, performance and desired spectral efficiency granularity. Furthermore, we should not discard variable symbol rate and FEC overhead solutions that can also be potentially used in future flexible transponders.

3.2.5 4D-coded PAM4 for short-reach applications

In this section, we propose to investigate the use of multi-dimensional coded modulation for short-reach intensity modulated direct-detected systems. High-speed, low-cost and short-reach interfaces capable to cope with the ever-growing bandwidth requirement in data centers to provide 100 Gb/s services and beyond are under active research [86], [87]. Contrary to long-haul systems which rely on coherent detection (used in the rest of this thesis), short reach systems are based on a much simpler architecture based on modulation of only one dimension of the optical field (intensity) and detection using a single photodiode to avoid resorting on multi-wavelengths multiplexing and to reduce the cost-per-bit. Short reach low-cost interfaces also rely on low-complexity and low overhead coding schemes such as hard-decision FEC thus making coded modulation an attractive solution. This class of modulation has been widely studied for long-haul applications [56], [79], [82], [83], [88], but long-haul transponders more and more rely on high-overhead soft-decision FEC to increase transmission reach, thus limiting their applicability in future systems. However, as shown in the previous sections, 4D modulation formats are particularly beneficial at high Q^2-factor operation which is well suited for systems based on low overhead FEC, and can be performed in singly polarized systems using the temporal dimension (i.e. 4 consecutive symbols for 4D modulation).

Among the candidates for short-reach intensity modulated direct-detected systems, 4-ary pulse amplitude modulation (PAM4) is advantageous over discrete multi-tone (DMT)[89] since it is compliant with 2-bit digital-to-analog converters (DAC) thus potentially simplifying the transmitter. Recently the transmission of 56 GBd PAM4 signals over a few kilometers of standard single mode fiber (SSMF) has been successfully demonstrated using a low resolution 2-bit DAC [87]. To improve the power budget of PAM signals for short reach data center intra-connection, one potential approach is to increase the symbol rate beyond 60 GBd to enable stronger FEC with >20% overhead [90]. However such a technique significantly increases the receiver power consumption. An alternative technique to improve the power budget at the expense of low extra computational complexity is thus the use of 4D-coded modulation. Instead of transmitting independent PAM symbols, we define a 4D-coded PAM4 constellation. Using the set partitioning (SP) scheme described in section 3.2.2, coded modulation formats can be derived from the combination of native PAM4 constellations. We consider the 4D-coded PAM4 format defined out of four consecutive PAM4 symbols (for 2D see [91]). When analyzed in the 4D space, this scheme defines an alphabet with a total of 256 (4^4) symbols, from which one subset

of 128 symbols can be selected to provide an increase of the constellation minimum Euclidean by a factor of √2. This results in the 4D-128SP-PAM4 format which will be simply called 4D-coded PAM4 in this thesis. A higher Euclidean distance is achieved at the expense of a lower number of bits per symbol than PAM4 (1.75 bits per symbol compared to 2 bits per symbol, respectively). Therefore to compare both modulation formats at the same bitrate, 4D-coded PAM4 requires 8/7 times higher symbol rate than PAM4.

We aim at comparing both solutions, namely PAM4 and 4D-coded PAM4, to provide 100-Gb/s service using intensity modulation, direct detection and 7% overhead HD-FEC. First, Fig. 3.22 (a) illustrates a diagram of a transceiver based on PAM4. The 104 Gb/s sequence (4-Gb/s protocol overhead) is encoded using a 7%-overhead FEC to generate a 112-Gb/s line-rate signal which is converted to PAM4 gray-mapped electrical signal at 56 GBd by a bit-to-symbol mapper (BtoS) which is physically implemented by a 2-bit DAC. This electrical signal modulates the intensity of a laser before propagation. At the receiver, optical-electrical conversion is performed by a single photodiode and the signal is amplified before being digitized by an analog-to-digital converter (ADC) followed by DSP. The signal processing consists of re-sampling, timing recovery, feed-forward equalization and symbol-by-symbol hard decision. The DSP output bits can be then decoded by a hard-decision FEC.

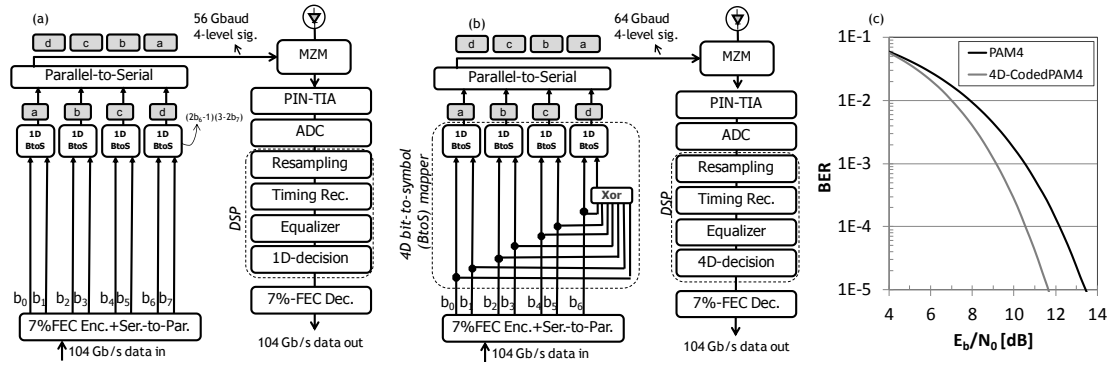

Fig. 3.22: a) IM-DD 112 Gb/s transceiver based on 56 GBd PAM4 and b) 64 GBd 4D-coded PAM4 c). Theoretical performance comparison, PAM4 vs 4D-coded PAM4.

Our proposed solution, 4D-coded PAM4 is depicted in Fig. 3.22 (b). Now, the output of the FEC encoder is converted to electrical signal by a 4D bit-to-symbol mapper, which for every 7 input bits produces 4 correlated output symbols. This function can be easily implemented employing basic digital logic on the same hardware as the one required for the generation of PAM4. For example, the 4D-coded PAM4 format can be obtained by selecting the subset of 128 points with even parity out of the 256-long symbol alphabet of four consecutive gray-mapped PAM4

symbols. To account for a lower number of bits per symbol (1.75), we set the baudrate to 64 GBd (112/1.75) to keep the bitrate constant compared to PAM4. The receiver side is similar up to the equalizer which is now followed by a minimum-distance 4D-demapper which outputs 7 bits for every block of 4 symbols. Finally, in Fig. 3.22 (c) we show the theoretical benefit of 4D-coded PAM4 versus uncoded PAM4. We evaluated the bit error rate (BER) as a function of signal-to-noise ratio per bit (E_b/N_0), a metric that accounts for the different number of bits per symbol of the studied formats. For example, at a BER of 10^{-3}, a SNR improvement of 1.4 dB can be observed and the benefit improves for lower BER.

Next we moved to experimental comparison using the setup depicted Fig. 3.23 (a). We send light from a semiconductor laser at 1545 nm into a 35-GHz-bandwidth Mach-Zehnder modulator (MZM), fed by the two complementary outputs of the 2bit-DAC . At the input of the 2bit-DAC, we inject four pseudo random bit sequences of 2^{15}-1-bit length at 28 or 32 Gbit/s, generated by a pattern generator. Our 2bit-DAC [92] is an in-house chip fabricated with InP heterojunction bipolar transistor process. The 2bit-DAC performs time division multiplexing (TDM) before digital to analog conversion inside two selectors (SEL). Each selector multiplexes two of the four 2bit-DAC inputs, producing PAM2 (i.e. conventional non return to zero) signals at twice the input datarate, i.e. 56 or 64 GBd. Each SEL supplies one of the two encoding bits to the DAC yielding 4-level signals at 56GBd or 64 GBd with up to 4-V_{pp} differential amplitude. Fig. 3.23 (b) shows the electrical eye-diagrams at 56 GBd and 64 GBd.

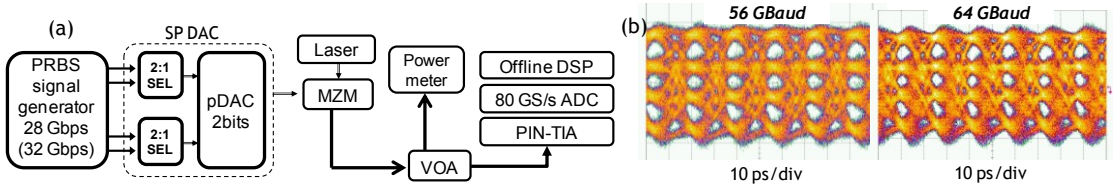

Fig. 3.23: (a) Experimental setup and (b) electrical eye diagrams of 56 GBd and 64 GBd PAM-4.

Before entering the receiver, the signal under test being either 56 GBd or 64 GBd is passed through a variable optical attenuator (VOA) to vary the input power sent to a 40-GHz-bandwidth PIN photodetector with trans-impedance amplifier (PIN-TIA). The received signal is then sampled at 80GS/s by a high-speed oscilloscope with 33 GHz bandwidth. We process the stored waveforms offline using the DSP chain described in Fig. 3.22 (a) and Fig. 3.22 (b). First, we re-sample the signals to perform clock and timing recovery with T/2-spaced samples. Then, T/2-spaced adaptive feed-forward equalization (FFE) with 21 taps is performed. For PAM4 signal, we perform symbol-by-symbol hard-decision and error counting to derive the

BER. Regarding 4D-coded PAM4, since the equalizer output symbols are PBRS-based PAM4 signal (see experimental setup Fig. 3.23 (a)), we included between the equalizer and the 4D-decision block a symbol de-interleaver (assuming a "virtual" interleaver at the transmitter as in [93]). Given the knowledge of the sent symbol sequence, the linear reordering function is calculated to generate an output sequence made of blocks of 4 symbols, in which each block corresponds to a valid equiprobable 4D-coded PAM4 symbol. Note that this interleaver is implemented for the unique purpose of this work and is not required for a practical implementation. Finally, after a 4D decoder using minimum distance detection, we derive the BER.

Fig. 3.24 (a) shows the performance measured in back-to-back for the 112 Gb/s PAM4 (squares) and the 112Gb/s 4D-coded PAM4 (empty triangles). We included for reference the performance of the 128 Gb/s PAM4 signal (filled triangles). Although the 4D coded PAM4 signal suffers from higher bandwidth limitations, observed from uncoded 64 GBd PAM4, it outperforms the uncoded PAM4 signal at BER below 10^{-2}. Then, in Fig. 3.24 (b), we quantify the advantage of the 4D-coded PAM4, measured in improved sensitivity versus BER. The black curve shows the experimental difference between required input power for a fixed BER for PAM4 and 4D-coded PAM4 at the same bitrate (derived from Fig. 3.24 (a)). The grey curve shows the theoretical difference between SNR per bit (derived from Fig. 3.22 (c)). We observe that the lower the BER, the more advantageous is the use of 4D-coded PAM4 as it provides an improved sensitivity of up to 1 dB compared to PAM4. As an example, we analyzed the potential gain of the 4D format for three FEC codes present in ITU recommendation G.975.1, key information of the tested codes is synthesized in the table in Fig. 3.24 (c). Considering a high performance hard-decision FEC such as 2 interleaved BCH code (circles), which has a FEC limit of $4 \cdot 10^{-3}$, the experimental advantage of using the 4D format is only 0.35 dB. On the other hand, by using a short Reed-Solomon with block length of 255 (squares) providing smaller latency and decoding complexity, the improved sensitivity of 4D-coded PAM4 is around 0.8 dB. This demonstrates that the use of multidimensional coded modulation could be attractive to increase power budget of high speed interfaces designed for short reach. The 4D gain is particularly high when associated with low complexity low latency HD-FEC.

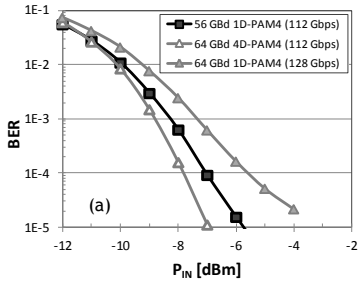

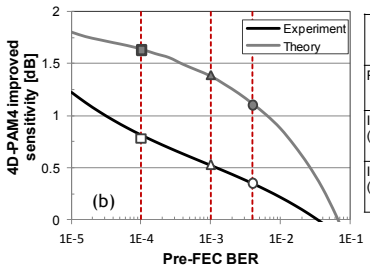

	FEC limit	4D impr. sens. (exp.)	4D impr. sens. (th.)	Block size
RS (255,239)	10^{-4}	0.8 dB	1.65 dB	255
Interleaved RS (2720,2550)	10^{-3}	0.55 dB	1.4 dB	2720
Interleaved BCH (522240,489472)	$4 \cdot 10^{-3}$	0.35 dB	1.1 dB	522240

(c)

Fig. 3.24: a) Back-to-back experimental results b) 4D increased sensitivity vs pre-FEC BER c) Tested FEC codes.

3.3. ***Summary***

In this chapter, modulation format optimization for optical communications was investigated. In section 3.1, 8QAM constellation choice was investigated considering system restrictions such as carrier frequency and phase estimation performance. We showed that although Circular-8QAM has large d_{min}, it has lower tolerance to phase noise compared Star-8QAM resulting in increased overhead reserved for pilots. In addition, Circular-8QAM is less tolerant to frequency detuning than the Star-8QAM, with a tolerance of ±3 GHz compared to ±5.2 GHz at 41.2 GBd. Despite these disadvantages, Circular-8QAM still outperforms Star-8QAM after transmission in a dispersion unmanaged SSMF link with hybrid EDFA/Raman amplification thanks to its quasi-Gray mapping, high d_{min} and limited phase-induced penalties. These phase induced penalties are kept low thanks to: use of stable lasers (linewidth around 200 KHz), dispersion unmanaged link which does not introduce significant nonlinear phase noise compared to dispersion managed links as well as adapted carrier phase recovery algorithms.

Then, we observed that d_{min} is not always the best predictor of performance when we compared candidate 8QAM constellations performance under variable code rate FEC based on pragmatic BICM coding scheme. Since, performance of BICM schemes without iterative demapping is strongly related to labeling, we observed that the most appropriate metric to compare constellations under this scenario is the generalized mutual information. We showed that Rect-8QAM with optimized power ratio between in-phase and quadrature components outperforms the other candidate constellation for low code rates (GMI < 2.3 inf. bits per symbol) despite small d_{min}. Therefore, as systems move to lower code rates looking for increased net coding gains, constellations like Rect-8QAM become more attractive. For the high code rate region, 8SP16QAM (GMI between 2.3 and 2.6 inf. bits per symbol) and Star-8QAM (GMI > 2.6 inf. bits per symbol) provide the best solution.

Subsequently, time-interleaved hybrid formats and 4D modulation formats were investigated in Section 3.2. We introduced these formats to fine tune the spectral efficiency and thus increase transponder flexibility. Particularly, we experimentally showed that 4D modulation (32-SPQAM) outperforms hybrid (Hybrid-QPSK/8QAM) in long-haul transmission thanks to its better power efficiency. Nevertheless, hybrid formats may still be useful, especially when going to even finer granularity due to its implementation simplicity. Note that, Rect-8QAM can be also seen as hybrid modulation (interleaving BPSK with 4PAM) and we showed that this format can be interesting in the low code rate regime. Finally, we showed that multi-dimensional modulation can be potentially attractive not only in the long-haul systems but also in short reach scenarios. We proposed the use of 4D-coded 4PAM to improve power budget in intensity modulation direct-detection systems. These low-cost short-reach 100 Gb/s systems must rely on low-complexity outer FEC schemes, exactly the scenario where 4D-coded PAM format provides its highest gain.

Chapter 4. High symbol rate spectrally-efficient transmission

In this chapter, we focus on high symbol rate transponders. The main motivation to study high symbol rate signals is integration, since more capacity can be delivered by a single transponder. We have observed in the last years a continuous increase in bandwidth of several opto-electronic components including DAC, ADC, driver and modulator. In addition, sampling rates of DAC and ADC have also significantly increased, and, the number of transistors that can be put in the same chip area has been doubling every 18 months for the last decades [94]. Therefore, if the symbol rate was typically around 30 GBd in the first generation of coherent optical communication systems at 100 Gb/s, we are now able to generate high-fidelity multilevel signals at symbol rates higher than 60 GBd as well as detect these signals using high-speed sampling devices and signal processing. That means that considering the same WDM bandwidth, the number of required transponders might be reduced by roughly a factor of two resulting in potential reduction of cost per bit.

As we increase the symbol rate of single-carrier signals, transmitter and receiver become less tolerant to several imperfections. For example, the use of suboptimal hybrids at the coherent receiver results in loss of orthogonality between

in-phase and quadrature components. The use of Gram-Schmidt orthogonalization algorithms have been proposed to compensate this imperfection [95]. Furthermore, timing mismatch (skew) between receiver signal paths also degrades performance. The receiver skew is usually compensated digitally by including interpolators after the ADC [96] or at the timing recovery block [97]. In Section 4.1, we investigate the receiver skew compensation and estimation problem which becomes more critical at very high symbol rates. We propose an architecture based on component-independent chromatic dispersion compensation combined with MIMO 4x2 adaptive equalizer [98], [99]. This architecture enables the compensation and estimation of the skew between ADC sampling channels even in the presence of large values of accumulated dispersion, a typical case in systems without inline dispersion compensation.

Then in Section 4.2, we study 400 Gb/s single-carrier transponder design compatible with transatlantic distance transmission [100]. The design results from complex trade-offs. In this study, we focus on joint optimization of FEC overhead and symbol rate. Using state-of-the-art spatially coupled LDPC, nonlinear compensation and 64 GBd PDM-16QAM, we demonstrate for the first time 400 Gb/s single-carrier transmission over 7200 km [101], [102].

Finally, in Section 4.3 we investigate 1 Tb/s signal generation and detection. To overcome the bandwidth limitations of several transmitter components, we propose the use of a parallel sub-band architecture to generate PDM-32QAM signal at 124 GBd [103], [104].

4.1. *Skew-tolerant blind equalizer and skew estimator*

Since high symbol rate signals are less tolerant to several channel impairments, novel signal processing algorithms become necessary. In this section, one of such algorithms is presented. This work is motivated by the recent high capacity long-haul optical communication system experiments based on high-speed electronics, coherent detection, polarization multiplexing, high-order modulation formats, tight channel spacing and pulse shaping with roll-off close to 0 [72], [105]–[107]. Increasing the symbol rate and modulation order as well as the use of roll-off factor close to zero reduces the transmission robustness to several impairments [108], among which a time misalignment (skew) between the 4 sampling channels in the receiver. Fig. 4.1 shows a simplified schematic of the skew between sampling channels. We suppose that the four signals coming from the coherent receiver are

aligned before the analog-to-digital converter: $s_{HI}(t)$, $s_{HQ}(t)$, $s_{VI}(t)$ and $s_{VQ}(t)$. However, after sampling at $1/T_{ADC}$ samples/s, there are now four unknown delays: τ_1, τ_2, τ_3 and τ_4. These delays (coming from mismatch in fiber and cable lengths) need to be estimated and compensated to ensure correct behavior of subsequent digital signal processing algorithms.

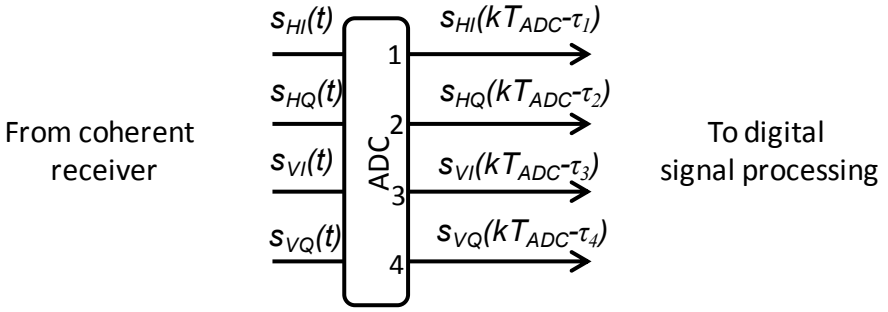

Fig. 4.1: Simplified receiver architecture digital CD compensation and MIMO 2x2 adaptive equalizer.

Recently, an adaptive equalizer that is tolerant to the receiver sampling skew has been proposed [109]. This approach is based on widely linear equalizers first proposed for wireless communications [110]. However this approach does not take into account the effect of chromatic dispersion (CD) compensation prior to the adaptive equalizer, required in long-haul non-dispersion managed systems. Indeed, the CD compensation mixes in-phase (I) and quadrature (Q) components of the signal [111], thus degrading skew compensation performance. To overcome this issue, an architecture that combines independent CD compensation with a complex-valued multiple-input multiple-output (MIMO) 4x2 adaptive equalizer can be used. This technique can relax the time alignment requirements of the receiver sampling channels, since the skew can be compensated electronically thanks to coherent detection and digital signal processing. Additionally, we show that skew estimation can be derived from the converged coefficients of blind MIMO 4x2 adaptive equalizer.

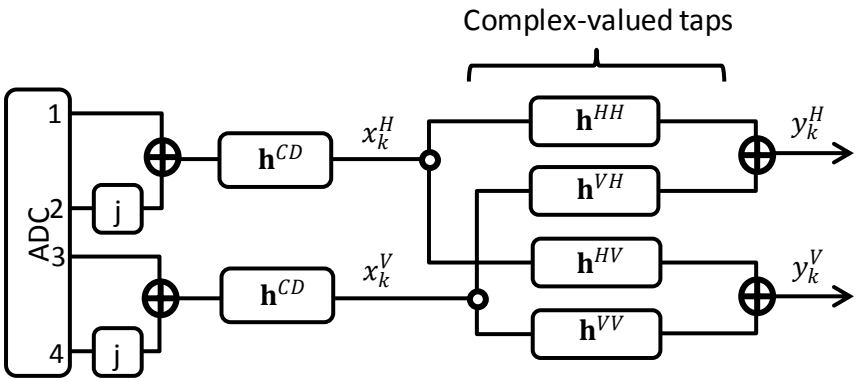

Fig. 4.2: Simplified receiver architecture digital CD compensation and MIMO 2x2 adaptive equalizer.

Fig. 4.2 shows a typical simplified schematic of coherent receivers with polarization diversity and digital signal processing. In this figure, we have first an analog-to-digital converter (ADC) that samples 4 signals corresponding to I and Q components of two orthogonal polarizations of an optical signal. We consider here that the ADC samples at twice the symbol rate and that the only imperfection is a skew between the 4 sampled signals (outputs 1-4 of ADCs in Fig. 4.2).

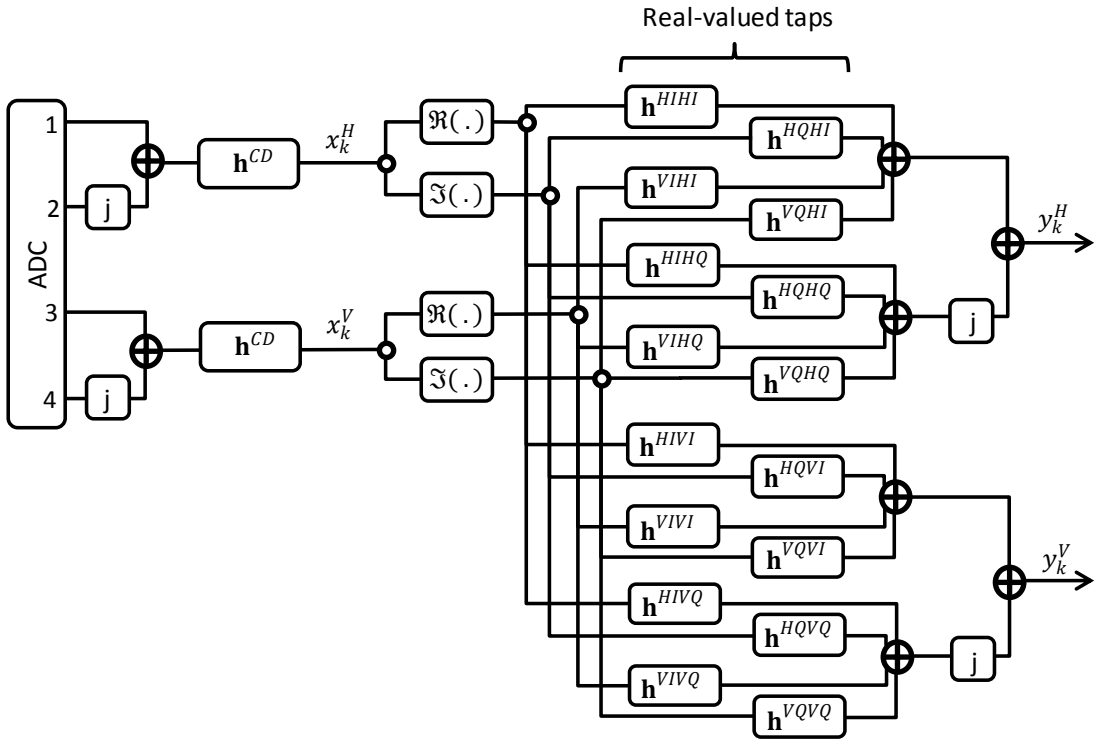

Fig. 4.3: Simplified receiver architecture digital CD compensation and MIMO 4x4 real-valued adaptive equalizer.

Emulation of receiver skew is done by using a digital filter using the frequency response shown in Eq. *4.1*, where τ_k is the skew measured in seconds for each k[th] path of ADC output.

$$H(f) = e^{j2\pi f \tau_k} \tag{4.1}$$

Then we construct the complex envelope of the signal and digital CD compensation is performed using a complex filter for each polarization. Next, a complex-valued MIMO 2x2 adaptive equalizer will de-multiplex the signals coming from orthogonal polarizations and compensate linear impairments such as residual CD and polarization-mode dispersion. Finally, the output signals are down-sampled to 1 sample per symbol and they feed the subsequent algorithms (i.e. carrier frequency and phase estimation).

We first review the matrix representation of the equivalent transfer function of both butterfly equalizers. For the MIMO 2x2 solution, we can write (as described in Section 2.3.2):

$$\begin{bmatrix} y_k^H \\ y_k^V \end{bmatrix} = \begin{bmatrix} (\mathbf{h}_k^{HH})^T & (\mathbf{h}_k^{VH})^T \\ (\mathbf{h}_k^{HV})^T & (\mathbf{h}_k^{VV})^T \end{bmatrix} \begin{bmatrix} \mathbf{x}_k^H \\ \mathbf{x}_k^V \end{bmatrix}. \tag{4.2}$$

where $\mathbf{x}_k^H = [x_{k-N}^H, \ldots, x_k^H, \ldots, x_{k+N}^H]^T$ and $\mathbf{x}_k^V = [x_{k-N}^V, \ldots, x_k^V, \ldots, x_{k+N}^V]^T$ are the sampled signals at the input of the equalizer (typically at 2 samples per symbol). The two equalizer outputs are y_k^H and y_k^V and the equalizer filters are $\mathbf{h}_k^{HH}$, $\mathbf{h}_k^{HV}$, $\mathbf{h}_k^{VH}$ and $\mathbf{h}_k^{VV}$, with $\mathbf{h}_k^{HH}=[h_{k-N}^{HH}, \ldots, h_k^{HH}, \ldots, h_{k+N}^{HH}]^T$ and so on. Note that equalizer coefficients are complex numbers for the MIMO 2x2 solution.

Another alternative, shown Fig. 4.3, employs real-valued MIMO 4x4 adaptive equalizer after CD compensation.in For the MIMO 4x4 solution the equalizer transfer function in matrix notation is:

$$\begin{bmatrix} y_k^H \\ y_k^V \end{bmatrix} = \begin{bmatrix} \mathbf{h}_k^{HIHI} & \mathbf{h}_k^{HIVI} \\ \mathbf{h}_k^{HQHI} & \mathbf{h}_k^{HQVI} \\ \mathbf{h}_k^{VIHI} & \mathbf{h}_k^{VIVI} \\ \mathbf{h}_k^{VQHI} & \mathbf{h}_k^{VQVI} \\ \mathbf{h}_k^{HIHQ} & \mathbf{h}_k^{HIVQ} \\ \mathbf{h}_k^{HQHQ} & \mathbf{h}_k^{HQVQ} \\ \mathbf{h}_k^{VIHQ} & \mathbf{h}_k^{VIVQ} \\ \mathbf{h}_k^{VQHQ} & \mathbf{h}_k^{VQVQ} \end{bmatrix}^T \begin{bmatrix} \Re(\mathbf{x}_k^H) \\ \Im(\mathbf{x}_k^H) \\ \Re(\mathbf{x}_k^V) \\ \Im(\mathbf{x}_k^V) \\ j\Re(\mathbf{x}_k^H) \\ j\Im(\mathbf{x}_k^H) \\ j\Re(\mathbf{x}_k^V) \\ j\Im(\mathbf{x}_k^V) \end{bmatrix}. \tag{4.3}$$

The advantage of this second approach (MIMO 4x4) is the possibility of applying different gain and delay for each of the 4 input channels, thus compensating receiver mismatches between I and Q (i.e. skew) while also de-multiplexing the two

orthogonal polarizations and performing linear equalization. However, since CD compensation filter (complex-valued filter) mixes I and Q components of the signal at the receiver, skew compensation degrades as accumulated dispersion increases. Therefore this approach fails in the case of non dispersion managed systems with large amount of cumulated CD at the receiver.

The mixing can be observed when we develop the CD compensation filter using real arithmetic. Note that these filters have complex coefficients, so to be compatible with real arithmetic hardware implementation, we should write the complex signals in terms of their real and imaginary components. For example, considering only the horizontal polarization, we obtain:

$$\begin{bmatrix} \Re(y_k^H) \\ \Im(y_k^H) \end{bmatrix} = \begin{bmatrix} \Re(\mathbf{h}^{CD}) & -\Im(\mathbf{h}^{CD}) \\ \Im(\mathbf{h}^{CD}) & \Re(\mathbf{h}^{CD}) \end{bmatrix} \begin{bmatrix} \Re(\mathbf{x}_k^H) \\ \Im(\mathbf{x}_k^H) \end{bmatrix} \tag{4.4}$$

Fig. 4.4 then shows how this can be implemented and the butterfly structure shows that each output depends on both inputs (mixing).

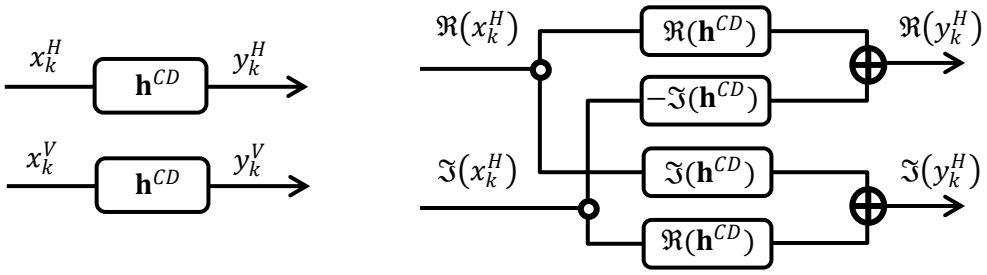

Fig. 4.4: Left: chromatic dispersion compensation of horizontal and vertical polarizations using finite impulse response filters. Right: detail of real arithmetic implementation (horizontal polarization).

To overcome this issue, a third approach is required based on complex-valued MIMO 4x2 adaptive equalizer, detailed in Fig. 4.5. Contrary to the previous equalizer, I and Q are kept independent before and after CD compensation since four separated CD filters are performed, resulting in four complex output signals after the CD compensation block. These four complex signals are inputs of a 4x2 complex MIMO equalizer that can apply different gains and delays for each of the input signals while demultiplexing the orthogonal polarizations. By applying different delays, this equalizer can compensate for time misalignements between the 4 ADC output channels and by doing independent CD compensation, we avoid I and Q mixing that degrades the skew compensation.

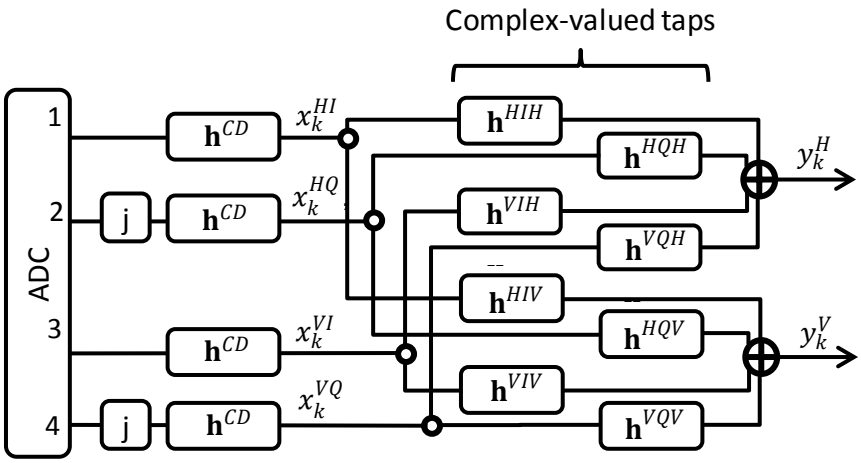

Fig. 4.5: MIMO 4x2 adaptive equalizer preceded by independent CD compensation.

The transfer function of this approach can be written as:

$$\begin{bmatrix} y_k^H \\ y_k^V \end{bmatrix} = \begin{bmatrix} (\mathbf{h}_k^{HIH})^T & (\mathbf{h}_k^{HQH})^T & (\mathbf{h}_k^{VIH})^T & (\mathbf{h}_k^{VQH})^T \\ (\mathbf{h}_k^{HIV})^T & (\mathbf{h}_k^{HQV})^T & (\mathbf{h}_k^{VIV})^T & (\mathbf{h}_k^{VQV})^T \end{bmatrix} \begin{bmatrix} \mathbf{x}_k^{HI} \\ \mathbf{x}_k^{HQ} \\ \mathbf{x}_k^{VI} \\ \mathbf{x}_k^{VQ} \end{bmatrix}. \tag{4.5}$$

The filter updates are done using stochastic gradient descent optimization to find the filters that minimize the constant modulus cost function. Other algorithms can be used, especially for high order modulations where multi-modulus algorithm is a popular option. Considering μ the step size of stochastic gradient descent, y_k^H and y_k^V the demultiplexed signals after the adaptive equalizer, x_k^{HI}, x_k^{HQ}, x_k^{VI} and x_k^{VQ} ($\mathbf{x}_k^{HI} = [x_{k-N}^{HI}, \dots, x_k^{HI}, \dots, x_{k+N}^{HI}]^T$) the four outputs of independent CD compensation and $\mathbf{h}_k^{HIH} = [h_{k,-N}^{HIH}, \dots, h_{k,0}^{HIH}, \dots, x_{k,N}^{HIH}]^T$) equalizer filters that are indexed based on input/output, the filter updates are:

$$\mathbf{h}_{2k+2}^{HIH} := \mathbf{h}_{2k}^{HIH} - \frac{\mu}{4}\frac{d\left(\varepsilon_{2k}^H\right)^2}{d\mathbf{h}_{2k}^{HIH}} = \mathbf{h}_{2k}^{HIH} + \mu \cdot \varepsilon_{2k}^H \cdot y_{2k}^H \cdot (\mathbf{x}_{2k}^{HI})^* \tag{4.6}$$

$$\mathbf{h}_{2k+2}^{HQH} := \mathbf{h}_{2k}^{HQH} - \frac{\mu}{4}\frac{d\left(\varepsilon_{2k}^H\right)^2}{d\mathbf{h}_{2k}^{HQH}} = \mathbf{h}_{2k}^{HQH} + \mu \cdot \varepsilon_{2k}^H \cdot y_{2k}^H \cdot (\mathbf{x}_{2k}^{HQ})^* \tag{4.7}$$

$$\mathbf{h}_{2k+2}^{VIH} := \mathbf{h}_{2k}^{VIH} - \frac{\mu}{4}\frac{d\left(\varepsilon_{2k}^H\right)^2}{d\mathbf{h}_{2k}^{VIH}} = \mathbf{h}_{2k}^{VIH} + \mu \cdot \varepsilon_{2k}^H \cdot y_{2k}^H \cdot (\mathbf{x}_{2k}^{VI})^* \tag{4.8}$$

$$\mathbf{h}_{2k+2}^{VQH} := \mathbf{h}_{2k}^{VQH} - \frac{\mu}{4}\frac{d\left(\varepsilon_{2k}^H\right)^2}{d\mathbf{h}_{2k}^{VQH}} = \mathbf{h}_{2k}^{VQH} + \mu \cdot \varepsilon_{2k}^H \cdot y_{2k}^H \cdot (\mathbf{x}_{2k}^{VQ})^* \tag{4.9}$$

$$\mathbf{h}_{2k+2}^{HIV} := \mathbf{h}_{2k}^{HIV} - \frac{\mu}{4}\frac{d\left(\varepsilon_{2k}^{V}\right)^2}{d\mathbf{h}_{2k}^{HIV}} = \mathbf{h}_{2k}^{HIV} + \mu \cdot \varepsilon_{2k}^{V} \cdot y_{2k}^{V} \cdot (\mathbf{x}_{2k}^{HI})^* \tag{4.10}$$

$$\mathbf{h}_{2k+2}^{HQV} := \mathbf{h}_{2k}^{HQV} - \frac{\mu}{4}\frac{d\left(\varepsilon_{2k}^{V}\right)^2}{d\mathbf{h}_{2k}^{HQV}} = \mathbf{h}_{2k}^{HQV} + \mu \cdot \varepsilon_{2k}^{V} \cdot y_{2k}^{V} \cdot (\mathbf{x}_{2k}^{HQ})^* \tag{4.11}$$

$$\mathbf{h}_{2k+2}^{VIV} := \mathbf{h}_{2k}^{VIV} - \frac{\mu}{4}\frac{d\left(\varepsilon_{2k}^{V}\right)^2}{d\mathbf{h}_{2k}^{VIV}} = \mathbf{h}_{2k}^{VIV} + \mu \cdot \varepsilon_{2k}^{V} \cdot y_{2k}^{V} \cdot (\mathbf{x}_{2k}^{VI})^* \tag{4.12}$$

$$\mathbf{h}_{2k+2}^{VQV} := \mathbf{h}_{2k}^{VQV} - \frac{\mu}{4}\frac{d\left(\varepsilon_{2k}^{V}\right)^2}{d\mathbf{h}_{2k}^{VQV}} = \mathbf{h}_{2k}^{VQV} + \mu \cdot \varepsilon_{2k}^{V} \cdot y_{2k}^{V} \cdot (\mathbf{x}_{2k}^{VQ})^* \tag{4.13}$$

where $\varepsilon_k^H = 1 - \left|y_k^H\right|^2$ and $\varepsilon_k^V = 1 - \left|y_k^V\right|^2$.

In the ideal case, where the only imperfection is the skew between the ADC outputs, the filters coming from the same polarization and also going to the same polarization (for example $\mathbf{h}_k^{VIV}$ *and* $\mathbf{h}_2^{VQV}$) should converge to the same frequency response except for a delay equivalent to the skew in its impulse response. This delay can be seen in the frequency domain as a linear variation of the phase as a function of the frequency and the skew is proportional to the slope of this phase in the band of the signal according to Eq. *4.1*. As we are interested in the difference between the delays of the channels (1/2 and 3/4) in order to estimate the skew, we first calculate the phase difference φ of the frequency response between two filters:

$$\varphi_H(f) = \angle\left(H_{HIV}(f) \cdot H_{HQV}(f)^* + H_{HIH}(f) \cdot H_{HQH}(f)^*\right) \tag{4.14}$$

$$\varphi_V(f) = \angle\left(H_{VIV}(f) \cdot H_{VQV}(f)^* + H_{VIH}(f) \cdot H_{VQH}(f)^*\right) \tag{4.15}$$

where H(f) is the discrete time Fourier transform of $\mathbf{h}_k$ written as:

$$H(f) = \mathcal{F}(\mathbf{h}_k) = \sum_{n=-N}^{N} h_{k,n} e^{-2\pi f \frac{n}{2R}}. \tag{4.16}$$

Where R is the symbol rate (we assume 2 samples per symbol at the input of the equalizer).These phases will converge to

$$\varphi_H(f) \approx \angle\left(e^{j2\pi f\frac{(\tau_1-\tau_2)}{2R}}\right) = 2\pi f\,\frac{(\tau_1-\tau_2)}{2R} \tag{4.17}$$

$$\varphi_V(f) \approx \angle\left(e^{j2\pi f\frac{(\tau_3-\tau_4)}{2R}}\right) = 2\pi f\,\frac{(\tau_3-\tau_4)}{2R} \tag{4.18}$$

in the band of the signal. Therefore a straightforward way to calculate the skew is doing a linear regression of this phase in the band of the signal to find the slope that is proportional to τ_1- τ_2 or τ_3- τ_4, the values we want to estimate.

We tested the proposed architecture and estimator using an experimental 46 GBd PDM-16QAM signal in a non-dispersion managed re-circulating loop composed of 4 spans of 100 km of large effective area single mode fiber with around 20 ps/nm of dispersion and hybrid Raman-EDFA amplification. We used root-raised-cosine pulse shaping with 0.1 roll-off factor. To emulate the receiver skew imperfection, we digitally delayed paths 1 and 3 with the same skew using Eq. *4.1* before processing them in 3 different ways.

Fig. 4.6 (a) shows the back-to-back results for the 3 algorithms: 2x2 complex (diamonds), 4x4 real (squares) and 4x2 complex (triangles). A penalty of around 0.5 dBQ is observed at ±6% skew when we use the classical 2x2 solution, and further the performance degrades rapidly. On the other hand, the two remaining solutions (4x4 real and 4x2 complex) are tolerant for the tested range of skews. When considering the 4000 km transmission, equivalent to around of 80000 ps/nm of accumulated dispersion (Fig. 4.6 (b)), we observe that the 4x4 real solution has similar performance as the 2x2 complex solution: with about 0.5 dBQ of penalty at ±9% of skew, therefore failing to compensate for the skew in the presence of CD. On the contrary, the 4x2 complex equalizer remains tolerant to the tested range of skews after 4000 km transmission, demonstrating the tolerance to large amount of CD of the studied architecture.

Next, in Fig. 4.6 (c) we show the estimated skew as a function of actual skew for a wider skew range. Squares represent the estimated skew and the solid line represents theoretical expectations. Note that we used here a step size μ for the equalizer of 1/12000 and we estimated the skew 200.000 symbols after equalizer initialization to ensure stable convergence. We can see in this figure that in the tested range of skew values, the proposed estimator is coherent with theoretical expectations, thus demonstrating the efficiency of the proposed estimator.

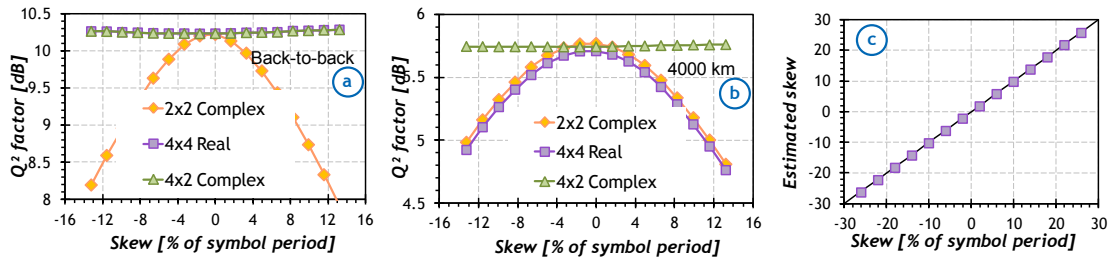

Fig. 4.6: Receiver skew tolerance of the algorithms in back-to-back (a) and after 4000 km transmission (b) . Skew estimation after 200000 symbols and step size 1/12000 (c).

Next, we investigated the impact of the convergence duration of the MIMO 4x2 equalizer onto the estimator performance. First, we set the skew of the horizontal

polarization to 0 ps (τ_1-τ_2=0) and 5.4 ps for the vertical polarization (τ_3-τ_4=5.4 ps, equivalent to 25% of symbol period). We also tested two different adaptive equalizer step sizes: 1/3000 (light curve) and 1/12000 (dark curve). Fig. 4.7 illustrates the evolution of estimated skew as a function of time, expressed in number of symbols. Note that we initialize the filters without a priori knowledge of the skew, namely with 0 ps. We observe in this figure that convergence around the actual skew of 25% of symbol period is achieved after $3 \cdot 10^4$ symbols when using 1/3000 step size. However, the estimations vary considerably over time. By choosing smaller step size μ of 1/12000, the estimation is clearly more stable at the expense of slower convergence.

Finally, we show an example of equalizer converged taps in Fig. 4.8. We calculated $\varphi_H(f)$ as function of the frequency for a receiver with 20% of skew between channels 1 and 2. Here we can see that the skew information is present on the slope of the curve and that this information is only present in the band of the signal. Since the signal has 2 samples per symbol and 0.1 of roll-off factor, the useful information is present roughly between $-R/2$ and $R/2$, R standing for the symbol rate. To estimate the skew, we used a simple linear regression between -23 GHz and 23 GHz to achieve all the previous results. We include in the curve a line with the slope of the actual skew as a reference.

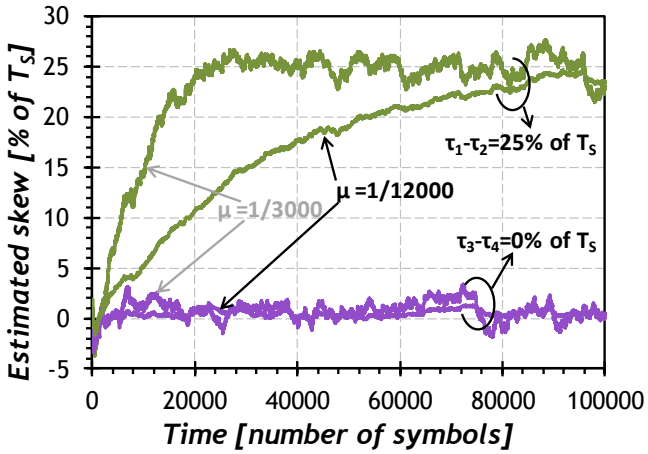

Fig. 4.7: Skew estimation convergence for both polarizations using two step sizes.

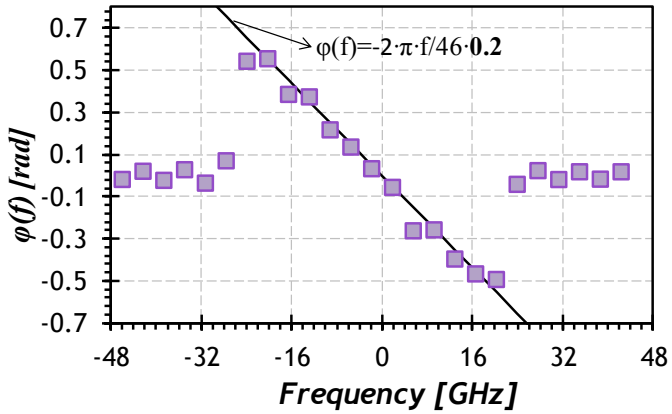

Fig. 4.8: Phase difference $\varphi_H(f)$ for a receiver impaired by a skew of 20% of symbol period, equivalent to 5.4 ps.

In summary, the receiver DSP architecture that we presented successfully compensates I/Q skew at the receiver even in the presence of large accumulated chromatic dispersion. This architecture is based on independent CD compensation filters followed by a 4x2 complex-valued MIMO equalizer. In addition, I/Q skew estimation can be derived from converged equalizer coefficients. As demonstrated in a 4000 km-long transmission of a 46 GBd PDM-16QAM signal, this solution is tolerant to large accumulated chromatic dispersion and successfully compensates and/or estimates for large range of receiver skews. Therefore this technique relaxes hardware constraints on receiver time alignment and would be particularly beneficial for non dispersion managed transmission systems relying on high symbol rate signals.

4.2. *First 400 Gb/s single-carrier transmission over submarine distances*

In this section, optical systems operating at a channel rate of 400 Gb/s are investigated. 400 Gb/s systems with ever-increasing spectral efficiency have been widely investigated to sustain traffic growth in optical fiber communications. For a few years, the approach of multi-carrier optical transport has gained momentum at such high bit rates to overcome the limitations of high-speed optoelectronics components. Particularly, the use of dual carrier transport of polarization division multiplexed (PDM-) 16-ary quadrature amplitude modulation (16QAM) format has been considered as a solution of interest to increase spectral efficiency beyond 5 bit/s/Hz in wavelength-division multiplexed (WDM) long haul transmission systems [112]. However, since the advent of WDM, increasing the bit rate per optical carrier has always proved to be the most effective method to drive the overall cost of optical

systems down so far. A few experiments based on electrical time division multiplexing have already demonstrated the generation and WDM transmission of single carrier 400-Gb/s using PDM-quadrature phase shift-keying (PDM-QPSK) [113], PDM-16QAM [114], [115] and PDM-64QAM [116]. Although distances up to 4000 km were demonstrated with 400 Gb/s single-carrier PDM-QPSK, the generation and reception of the 107-GBd signal remains challenging as it requires optoelectronic components with very high bandwidths. On the other hand, with PDM-64QAM, 400 Gb/s transport was shown using a much lower symbol rate (43 GBd) at the expense of strongly reduced maximum reach of 600 km. Thus, PDM-16QAM appears to be a good trade-off between required bandwidth of transceiver components and transmission reach. For previous single-carrier PDM-16QAM experiments, the spectral efficiency was limited to 4 bit/s/Hz and the maximum transmission distance reported was 1200 km due to the significantly high penalties coming from imperfect response and limited bandwidth of optoelectronic components, as well as non optimized forward error correction (FEC).

Here, we design a coherent transceiver at 400-Gb/s with improved performance compared with previous 400-Gb/s single-carrier experiments. This is achieved using: digital-to-analog conversion with higher resolution, minimization of inter-symbol interference based on optical shaping, and joint-optimization of symbol rate and channel coding overhead. By using PDM-16QAM combined with high symbol rates, it is possible to achieve bit rates well over 200 Gb/s per channel as well as reduce the number of transponders per fiber. However high-order formats at such symbol rates are more sensitive to the limited bandwidth and imperfect response of state-of-the-art electronics (transmitter and receiver). Thus more powerful FEC with larger overheads started to be used at the expense of channel capacity. Therefore, transceiver design results from complex trade-offs. Here, we address these trade-offs considering the following strategy. We set the constraint of a predefined net data rate of 400 Gb/s. We considered PDM-16QAM modulation and optimized inter-symbol interference mitigation as well as forward error correction.

As depicted in Fig. 4.9, to generate the PDM-16QAM signal, the in-phase and quadrature components are generated by a pair of 8-bit 88 GS/s DAC delivering multi-level delayed-decorrelated sequences of length 2^{15}. We digitally pulse shape these signals using a root-raised cosine filter with 0.01 roll-off factor and with a pre-emphasis filter to enhance the high frequencies and partially mitigate the transmitter limited bandwidth. These two electrical signals are amplified by wideband drivers before modulating the light from a tunable laser source (TLS) using a Mach-Zehnder I-Q modulator to generate 16QAM signal. Polarization division multiplexing (PDM) is then emulated with split-and-combine method to generate PDM-16QAM data. Next

the signal is amplified by an EDFA and filtered out by a reconfigurable filter used for optical pre-emphasis. The inset in Fig. 4.9 depicts the optical spectrum of the generated signal before optical pre-emphasis, illustrating the bandwidth limitations of our equipment (cascade of DAC, driver and modulator). The 15 dB attenuation observed in this figure underlines that we operate each of the transmitter components well above their nominal 3-dB electrical bandwidth.

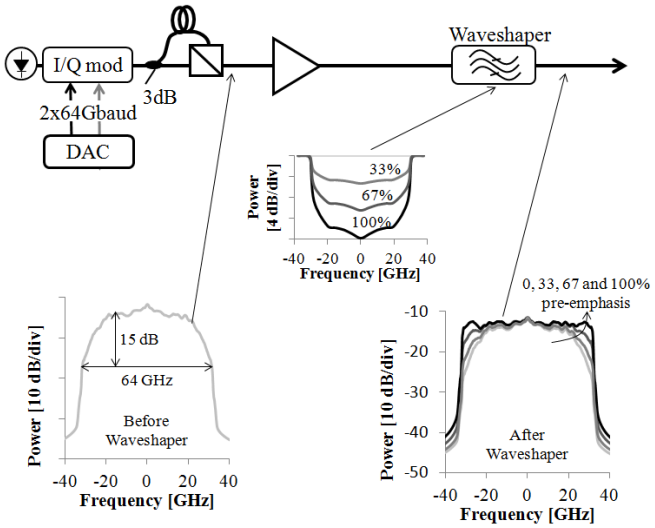

Fig. 4.9: Generation of optimized single carrier 400-Gb/s transceiver

At the receiver side, our channel is passed through a tunable filter, sent into a coherent mixer and sampled at 80 GS/s using a digital sampling oscilloscope with a 33-GHz electrical bandwidth. For each measurement, five data sets of 40 µs duration are captured. The waveforms are processed off-line using DSP blocks shown in Fig. 4.10. Since signals at such high symbol rates are known to be less tolerant to receiver imperfections, chromatic dispersion compensation (CDC) and polarization demultiplexing using constant modulus algorithm (CMA) are performed as in Section 4.1 (MIMO 4x2). Next, frequency and phase estimation (CFE/CPE) are performed using 0.5% overhead pilot symbols to recover absolute phase and support direct detection. The last DSP stage is a post-equalizer composed of a T-spaced decision-directed adaptive linear equalizer followed by a decision feed-back equalizer (DFE) to mitigate the impact of residual ISI. Bit error ratio (BER) is finally computed and subsequently converted into Q^2-factor.

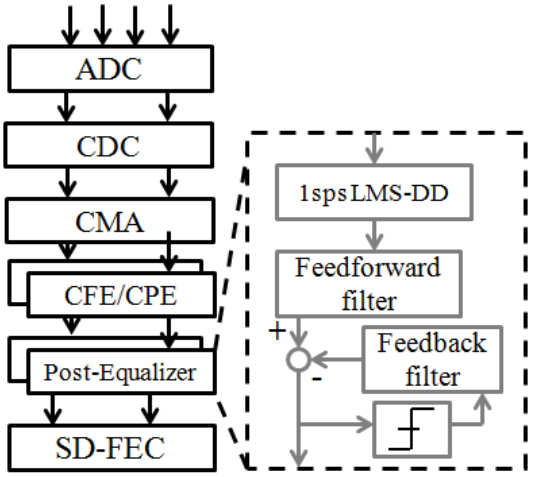

Fig. 4.10: Digital signal processing.

To mitigate ISI induced penalties, we set the symbol rate to 64 GBd and apply optical pre-emphasis using a reconfigurable optical filter. To flatten the signal frequency response, a full compensation profile (100%) can be applied accompanied with signal attenuation of 15 dB. To find out the best trade-off between ISI mitigation and maximum output OSNR of the signal, which may induce significant performance error floor, we vary the profile of optical pre-emphasis down to 67%, 33% and 0% with corresponding attenuation of 10, 5 and 0 dB respectively. Fig. 4.11 shows Q^2-factor (filled markers) and DFE gain (empty markers) as a function of the OSNR for the four profiles (0%, diamonds; 33%, squares; 67%, triangles and 100%, circles). The highest DFE gain is observed for the 0% pre-emphasis profile with up to 1.6 dB gain. The DFE gain indeed decreases when pre-emphasis is increased, and also when optical noise becomes dominant. The best Q^2 performance is measured for the 100% pre-emphasis, slightly outperforming the 67% profile for Q^2-factors below 7 dB. Both curves saturate in the high OSNR region with 67% profile providing slightly higher Q^2-factor thanks to higher maximum output OSNR. Nevertheless, the degradation in maximum output OSNR of the 100% pre-emphasis profile is sufficiently small so that this profile becomes the best performing one when the OSNR decreases below 23 dB as it is best mitigating ISI-induced penalties. We also observe that the experimental performance is only 2 dB away from theoretical expectations, depicted in the figure by the black solid line.

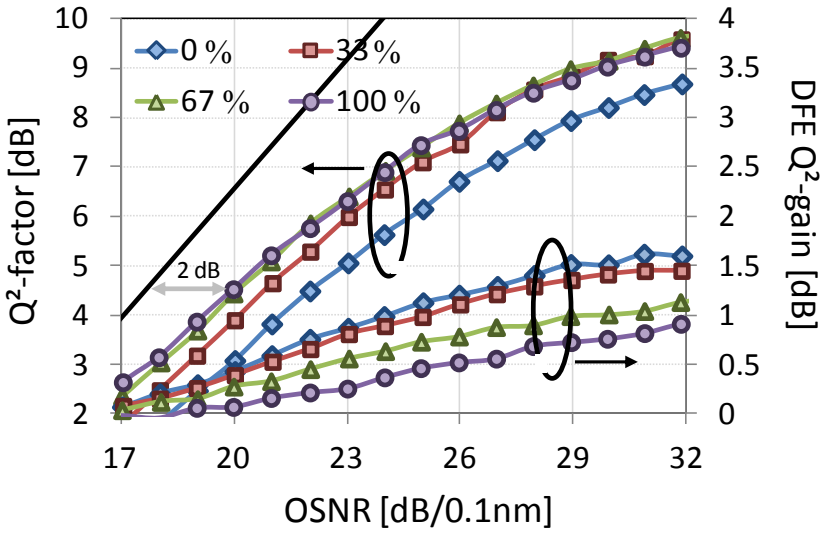

Fig. 4.11: Q²-factor and DFE gain as a function of OSNR for various pre-emphasis profiles

Next, we jointly optimize FEC overhead and symbol rate by considering five candidate symbol rates ranging from 58 to 66 GBd. We employ a left-terminated, weakly coupled irregular SC-LDPC [117] codes with syndrome former memory $\mu = 1$ as code class of choice, due to their excellent error floor properties (Section 1.3.2). SC-LDPC codes are also suited to realize rate-adaptive codes [118], [119], which makes them ideal candidate for this work. We select the code rates $r \in \{0.87,0.84,0.81,0.79,0.76\}$, corresponding to the rates providing 400 Gb/s of information rate using the symbol rates from 58, 60, 62, 64 and 66 GBd, respectively (see Table 4.1, expressed in FEC overhead). As coded modulation scheme, we use the pragmatic bit-interleaved coded modulation (BICM) scheme, which can closely approach the constellation constrained capacity with 16-QAM and Gray mapping. We use windowed decoding [24] with a window length of w = 15 and 10 decoding iterations are carried out in each window step. A full description of the code design can be found in [102], [120].

The measured performances of the considered FEC overheads for each symbol rate are summarized in Table 4.1. Fig. 4.12 top curve then depicts the experimental required OSNR for error free operation with each considered FEC overheads and symbol rates in single channel back-to-back configuration. These results are obtained from measured performance before and after FEC of the chosen overhead/symbol rate pair. We also included in Fig. 4.12 the theoretically required OSNR considering ideal signals with additive white Gaussian noise for each symbol rate and corresponding FEC threshold. This figure demonstrates that the implementation impairments increase with the symbol rate and can overcome the

coding gain improvement brought by empowered FEC. The best trade-off between coding gain and implementation penalties is found with 64 GBd and 27.3% overhead (highlighted with a star), leading to 19.8 dB of required OSNR. We additionally included in Fig. 4.12 the Shannon capacity limit and the 16QAM constellation constrained capacity, which defines the theoretical minimum required OSNR for error free operation at each candidate symbol rate when 16QAM constellation is used. From this figure, we can observe that our optimum design at 64 GBd is about 4 dB away from the Shannon limit, including 2 dB penalty from our experimental implementation (limited bandwidth and imperfect response of equipment), 1 dB penalty from our FEC implementation (BICM scheme with limited number of iterations…) and 1 dB theoretical penalty from the use of the 16QAM constellation.

Symbol rate (GBd)	58	60	62	64	66
Raw bit rate (Gb/s)	464	480	496	512	528
FEC OH (excluding 0.5% pilot)	15.4	19.4	23.4	27.3	31.3
Q^2 limit	5.6	5.25	4.9	4.55	4.3

Tab. 4.1: Symbol rates with corresponding FEC overheads and Q^2 thresholds

We finally validate the design of our 400-Gb/s single carrier transceiver in ultra long-haul WDM transmission experiments without inline chromatic dispersion compensation. With such transmission systems, the distribution of noise stemming from amplified spontaneous emission and non linear effects is well approximated by Gaussian distributions according to the Gaussian model [17]. Therefore our ISI and FEC overhead optimization procedure performed by minimizing the required OSNR for error-free operation in single-channel back-to-back configuration yields the maximum transmission distance. Our transmitter consists of five 75 GHz (resp. 66.7 GHz) spaced channels split in two sets of even and odd channels modulated separately with 64 GBd PDM-16QAM, yielding spectral efficiency of 5.33 bit/s/Hz (resp. 6 bit/s/Hz). Another set of thirty channels spaced by 50 GHz is used for amplifier loading and separately PDM-16QAM modulated with a symbol rate of 43 GBd (resp. 48 GBd) to maintain constant the power spectral density (43/50≈64/75). The three sets of channels are amplified and multiplexed by a flexible filter which also applies the attenuation profile optimized in Fig. 4.11 on the 64 GBd channels. The resulting multiplex is amplified before being injected into the recirculating loop (Fig. 4.13). The loop as in [15] consists of twelve 50-km-long spans made of 25 km of pure silica fiber (Corning EX3000) followed by 25 km of slightly different pure silica fiber

(EX2000). EX3000 (EX2000 resp.) effective area was 150 μm^2 (110 μm^2 resp.). Both fibers have 0.160 dB/km average loss, 20.5 ps/nm km dispersion at 1550 nm and less than 0.1 ps/√km polarization mode dispersion. Span loss was about 8.5 dB and was fully compensated by EDFA-only amplification. Power adjustment is performed with a dynamic gain equalizer inserted at the end of the loop prior to loop-synchronous polarization scrambling.

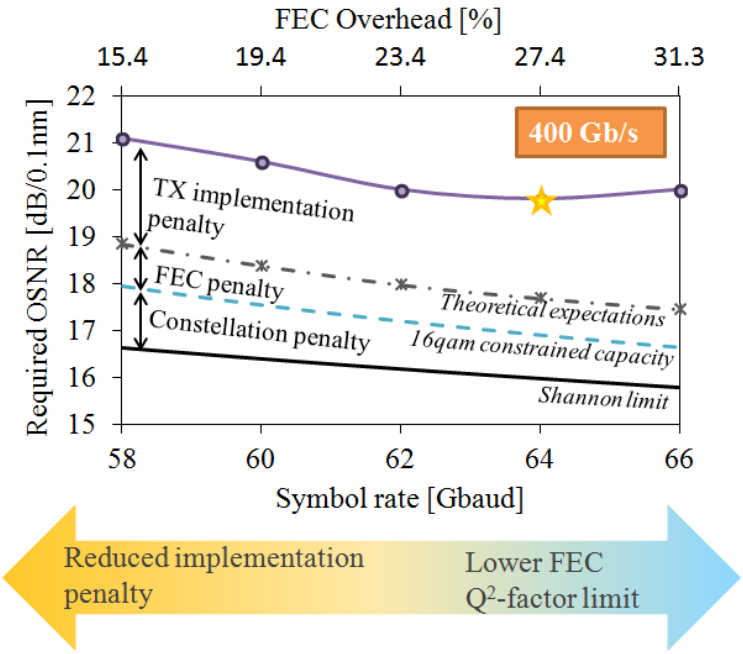

Fig. 4.12: Experimental required OSNR (in back-to-back) at SD-FEC limit versus symbol rate (circles). Monte Carlo simulated required OSNR at SD-FEC limit versus symbol rate (crosses). For reference: 16QAM constellation constrained capacity and Shannon limit.

At the receiver side, the test channel is selected by a tunable filter and sent into the coherent receiver which now includes non linear mitigation based on filtered digital back propagation (FDBP) [18] with one step every four spans, where during the nonlinear sub-steps the nonlinear phase is processed by low pass filter (LPF) to improve accuracy (see section 2.4.2). We found that super-Gaussian LPF with order 0.5 gives the best compensation performance [121]. Filter bandwidth and phase correction gain were optimized for each measurement. First, we set the channel spacing to 75 GHz and we optimize the total launched power at each fiber span input. Fig. 4.14 shows the performance after 6600 km (i.e. 11 loops) of one of the test channels measured in Q^2-factor as a function of power.

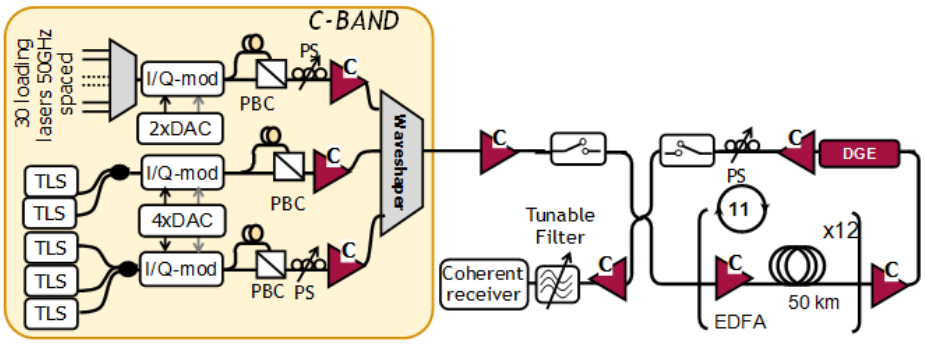

Fig. 4.13: Transmission setup.

Filled squares represent performance with filtered digital back-propagation and empty squares without it. We also included several reference curves. The first one depicted as a black solid line is the potential performance of the system if we had an ideal transmitter (TX) and nonlinearity-free propagation. To derive this metric, we first calculate the OSNR at the receiver using Eq. *2.7* (section 2.2) and transmission link parameters. We consider in addition to the 8.5 dB span loss, an extra 1 dB to account for connector's loss and other experimental penalties. Additionally, we have to account for extra amplifiers due to the use of recirculating loop with dynamic gain equalizer. The second reference curve (red solid line) depicts the potential performance of our experimental transmitter considering nonlinearity-free propagation. Despite efforts to minimize implementation penalties, our transmitter is still 2 dB worse than an ideal transmitter thus impacting the maximum achievable performance. Then, the solid light red curve depicts the expected performance after nonlinear transmission if we assume the use of our experimental transmitter and that nonlinear interference is Gaussian (see section 2.4.2). Variance of the nonlinear interference is calculated using the perturbation method [47]. We observe that expected performance and nonlinear threshold are very close to experimental results (empty squares), thus confirming the performance prediction capabilities of models that approximate nonlinear interference using Gaussian distribution. Finally, we divided the nonlinear interference into two distinct components: interference coming from intra-channel nonlinear interactions and interference depending on neighbors. The dashed curve depicts expected performance under nonlinear interference Gaussian approximation, assuming full compensation of intra-channel nonlinear impairments. We observe that under this assumption, we can obtain around 1 dB higher performance and launch power. We observe that experimental performance with filtered digital backpropagation approaches the dashed curve showing that this algorithm can effectively mitigate part of the nonlinear intra-channel interference.

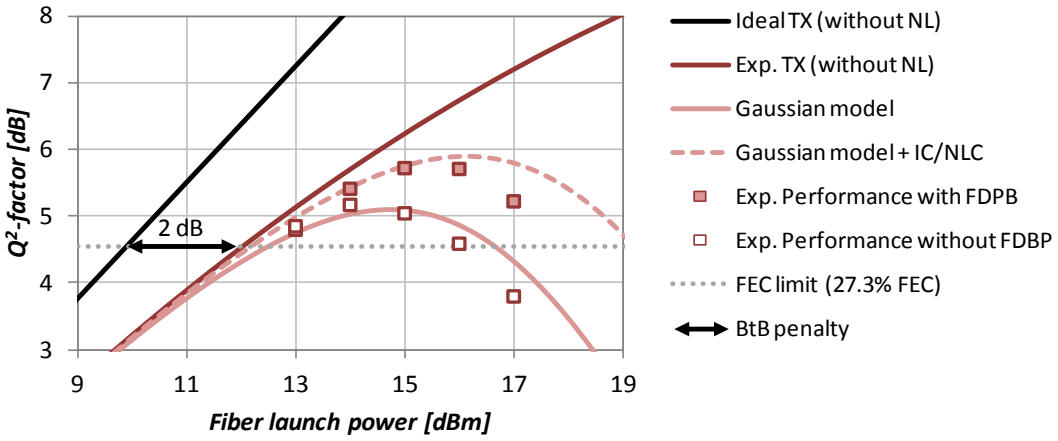

Fig. 4.14: Measured performance after 6600 km with 75 GHz spacing. With digital back-propagation (filled markers) and without it (empty markers). Solid lines represent expected performance: with ideal (black) or experimental (dark red) transmitter without considering transmission non-linearities, with experimental transmitter and non-linear interference modeling as extra Gaussian noise (light red). Dashed line represents expected performance with experimental transmitter with ideal intra-channel non-linear compensation and Gaussian model.

Experimental optimum launch power was found to be between 14 dBm and 15 dBm when not applying nonlinear mitigation and between 15 and 16 dBm when using filtered DBP algorithm (as predicted by analytical models). We set the total launched power to 15 dBm for both 75 GHz and 66.7 GHz channel spacing experiments which is near the optimum for both cases. We first measured the performance of the five 400 Gb/s test channels with 75 GHz spacing after 7200 km. Fig. 4.15 shows the performance of the five channels with (filled markers) and without applying filtered DBP (empty markers). The performance gain brought by filtered DBP is ~0.5 dB for each channel. Using filtered DBP, the performance is always above the considered SD-FEC limit of 4.55 dB and all sets of data are decoded without error by our SD-FEC, demonstrating the first successful transmission of 400 Gb/s channels over 7200 km with a spectral efficiency of 5.33 bit/s/Hz.

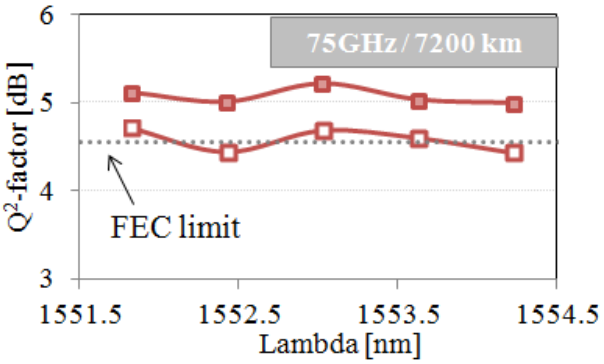

Fig. 4.15: Measured performance after 7200 with (filled markers) and without filtered DBP (empty markers) using 75 GHz spacing.

We then investigated the impact on the transmission distance of further increasing spectral efficiency up to 6 bit/s/Hz by decreasing the channel spacing. The channel spacing was set to 66.7 GHz using the reconfigurable filter and reconfiguring the wavelengths of the five test channels. The symbol rate of loading channels was set to 48 GBd in order to maintain a constant power spectral density in the WDM comb. Fig. 4.16 now shows the Q^2-factor as a function of wavelength for the five test channels after 6600 km with the new spacing of 66.7 GHz. Empty and filled squares indicate the performance obtained without and with filtered DBP. With this channel spacing of 66.7 GHz, we observe a similar gain of 0.5 dB brought by filtered DBP. This figure also shows that using filtered DBP all channels exhibit a performance above the FEC threshold of 4.55 dB and are decoded without error by our SD-FEC. Compared to the previous experiment, the transmission reach reduction from 7200 to 6600 km is attributed to the fact that decreasing the channel spacing from 75 GHz to 66.7 GHz increases the amount of non linear cross-talk between channels. Nevertheless, this result demonstrates the first single carrier transmission at 400 Gb/s net data rate over 6600 km with 6 bit/s/Hz of spectral efficiency.

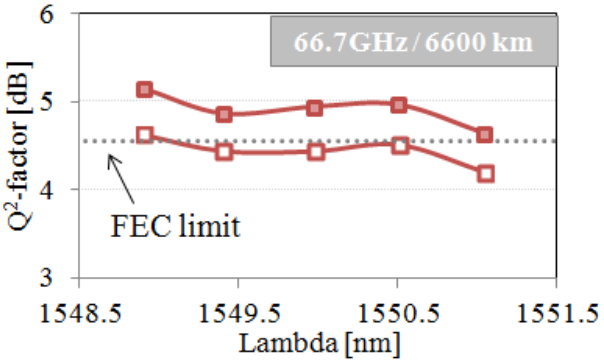

Fig. 4.16: Measured performance after 6600 km with (filled markers) and without filtered DBP (empty markers) using 66.7 GHz spacing.

In summary, we have designed a spectrally efficient single-carrier 400 Gb/s data rate terminal by optimizing ISI mitigation and FEC overhead. Using optical pre-emphasis, digital signal processing and spatially coupled LDPC, our optimized transceiver is only 4 dB away from the Shannon limit in back-to-back. We validated our design by successfully transmitting five channels spaced by 66.7 GHz and 75 GHz over 6600 km and 7200 km, respectively. An average Q^2-factor gain of 0.5 dB was achieved with nonlinear mitigation based on filtered DBP, resulting in the first single-carrier 400 Gb/s transmission over transatlantic distances. This result paves the way for submarine single-carrier transport at 400 Gb/s and beyond.

This result demonstrates some key trends in optical communications. First, thanks to constant improvement of opto-electronic devices we can now generate multi-level signals with symbol rates beyond 60 GBd. Therefore, this enables the integration of more capacity in a single transponder which has the potential to reduce the cost per bit. Furthermore, available computational power dedicated to signal processing and channel coding is expected to increase thus making the use of nonlinear compensation algorithms and high net coding gain FEC possible. Those are key technologies for further improvement of performance of coherent optical systems. In conclusion, considering that commercial systems operating over transatlantic distances are currently limited to 200 Gb/s per channel, our optimized 400 Gb/s transponder has the potential to reduce the number of transponders by a factor 2 while keeping the total fiber capacity constant.

4.3. *First 1 Terabit/s transmitter based on sub-band transmitter*

To further reduce the number of required transponders per fiber, we are also interested on investigating solutions beyond 400 Gb/s per channel. For example, the generation of single carrier signals using PDM-16QAM at 107 GBd [122], PDM-64QAM at 72 GBd [111] and 90 GBd [123] have already been demonstrated but with performance strongly limited by induced filtering penalties at such high symbol rates. The use of superchannels can overcome such a limitation to achieve very high interface rates (e.g. 400 Gb/s [112] or 1 Tb/s [107], [124], [125]). However, to push single-carrier transmission further, another approach based on spectral sub-bands synthesis has been proposed to take advantage of mature optoelectronics components with reduced bandwidth through a parallelized architecture [126]. Based on three spectral sub-bands synthesis, the long-haul transmission of single carrier PDM-16QAM channel has been recently demonstrated, but at a net data rate of 800

Gb/s and a spectral efficiency of 6.2 b/s/Hz [127]. Another experiments demonstrated the concept at lower symbol rate can be found in [128] and at the receiver [129].

Here, we describe the generation of a spectrally efficient 1.24 Tb/s single-carrier modulated channel and its long-haul transmission [103]. The Nyquist shaped 124 GBd PDM-32QAM signal is synthesized from the parallel generation and combination of four spectral sub-bands spaced by 32.5 GHz and detected using a 62.5-GHz coherent receiver, in which the four parallel sub bands are phase synchronized using a novel phase mismatch compensation stage. The 1-Tb/s net data rate channel is finally inserted into a 125-GHz slot and successfully transmitted over 660 km of low loss large effective area fibers with erbium doped fiber amplification (EDFA) only and soft decision forward error correction (SD-FEC).

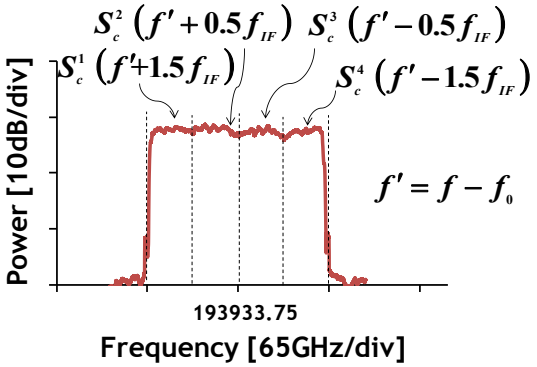

Fig. 4.17: 124 GBd signal made of 4 sub-bands..

We consider here the generation of a passband signal $s(t)$ which can be written as

$$s(t) \propto \Re\{s_c(t)e^{j2\pi f_0 t}\} \tag{4.19}$$

where f_o is our carrier frequency and $s_c(t)$ is the baseband complex envelope of the signal to transmit. The main idea of the sub-banded transmitter is to divide the total spectrum into K spectral sub-bands which are generated in parallel before being recombined, so as to reduce by K-fold the bandwidth requirement on opto-electronic components. Here we propose to divide $s_c(t)$ into four sliced sub-bands such as

$$s_c(t) = \sum_{k=1}^{4} s_c^k(t)e^{j2\pi(k-2.5)f_{IF}t} \tag{4.20}$$

where $s_c^k(t)$ is a baseband signal corresponding to a portion of the signal $s_c(t)$ and f_{IF} stands for an intermediate frequency. After Fourier transform, this can be written as:

$$S_c(f) = \sum_{k=1}^{4} S_c^k(f - (k - 2.5)f_{IF}) \tag{4.21}$$

In Fig. 4.17, we show an exemplary spectrum considering f_{IF} equals 32.5 GHz.

To generate our 124 GBd 32QAM signal with our digital-to-analog converter (DAC) equipment made of four independent outputs (x_a, x_b, x_c, x_d) and complementary ones $(\bar{x}_a, \bar{x}_b, \bar{x}_c, \bar{x}_d)$, we first generate a real valued 124 GBd pulse amplitude modulation (PAM) optical signal, before applying a PAM-to-QAM optical conversion (see Fig. 4.18). Using our independent and complementary outputs, we are able to generate the following signals:

$$S_c^3(f) = \mathcal{F}(x_a + jx_b) \tag{4.22}$$

$$-S_c^3(f) = \mathcal{F}(\bar{x}_a + j\bar{x}_b) \tag{4.23}$$

$$S_c^4(f) = \mathcal{F}(x_c + jx_d) \tag{4.24}$$

$$-S_c^4(f) = \mathcal{F}(\bar{x}_c + j\bar{x}_d) \tag{4.25}$$

where $\mathcal{F}(\cdot)$ denotes the Fourier transform. Then, using the Hermitian property (spectral symmetry of the Fourier transform of real signals) of PAM signals, and adjusting the bias point of our Mach-Zehnder Modulators (MZM) to generate complex conjugate signals, we are able to generate the symmetrical sub-bands as follows:

$$S_c^1(f) = \left(S_c^4(-f)\right)^* = \mathcal{F}(\underbrace{-}_{Bias\ C}\ \bar{x}_c + j\bar{x}_d) \tag{4.26}$$

$$S_c^2(f) = \left(S_c^3(-f)\right)^* = \mathcal{F}(\underbrace{-}_{Bias\ C}\ \bar{x}_a + j\bar{x}_b) \tag{4.27}$$

Once generated this real valued signal enters a PAM-to-QAM converter, which splits, decorrelates (500 ps = 62 symbols) and recombines the signals with π/2 optical phase difference. Our transmitter configuration is described in Fig. 4.18. We use an external cavity laser (ECL) with 100 kHz linewidth and optical frequency 193.95 THz (corresponding to f_0+0.5f_{IF}), followed by a MZM fed with a sinus wave at a frequency f_{IF} of 32.5 GHz from an external clock generator. This scheme produces a comb of multiple coherent spectral lines, equally-spaced by 32.5 GHz, which are amplified and demultiplexed by an optical flexible filter with 40 dB suppression ratio. Spectral lines 1, 2, 3 and 4 are filtered out, passed into four separate single-polarization I/Q modulators, fed with electrical waveforms from 8-bit DACs operating

at 65 GS/s and triggered by the same reference clock at 10 MHz as that of external synthesizer. The waveforms loaded in the DACs are obtained as follows: first a sequence of 6PAM pseudorandom symbols of length 2^{16} is generated and up-sampled by a factor of two before root-raised-cosine pulse shaping with 0.001 roll-off factor. Note here that the 6PAM sequence is defined so that the four corner states of the 36QAM constellation obtained from PAM-to-QAM conversion are not visited, thus yielding 32QAM constellation. Then the signal is split into four paths indexed as k={1,2,3,4} before being shifted in frequency by (k-2.5)*32.5 GHz and low pass filtered by ideal window filters with 16.25 GHz electrical bandwidth. At the output of this stage, four signals corresponding to the four sliced sub-bands of the 124 GBd signal are generated and down sampled to match our DAC sampling rate of 65 GS/s. Owing to the Hermitian property of real valued signals, only sub-bands 3 and 4 are loaded in the independent and complementary outputs of our DACs. The bias points of I/Q modulators 1 and 2 are adjusted to generate sub-bands 1 and 2 according to Eq.*4.26* and Eq. *4.27*, so that the four sub-bands of our real valued 124 GBd 6PAM signal are generated. Then, using the optical delay lines added to each optical path, the delays introduced between the different paths are optimized so that all sub bands are time aligned with less than 1ps, corresponding to less than 12.5% of the symbol duration. Fine phase adjustment between all sub-bands will be performed within the receiver DSP. The sub-bands are then coupled in order to obtain the 124 GBd 6PAM signal. This signal is then passed through our PAM-to-QAM converter to generate the 124 GBd 32QAM signal. PDM is then performed with split-and-combine method (around 10 ns) to generate 124 GBd PDM-32QAM data, yielding 1.24 Tb/s raw data rate.

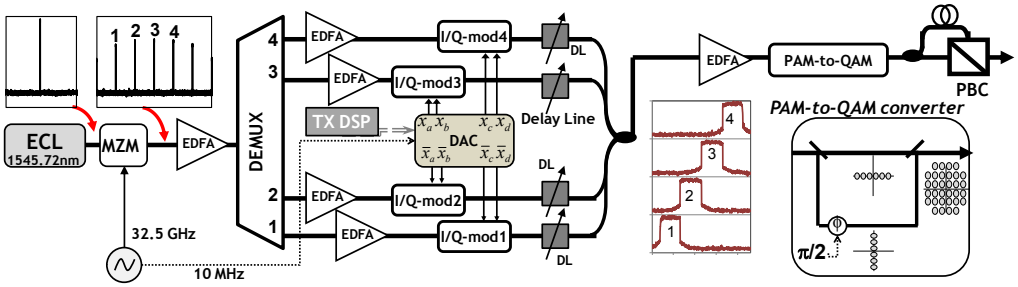

Fig. 4.18: Sliced sub band transmitter setup for the generation of 124 GBd Nyquist shaped PDM-32QAM

The generated 124GBd channel is then sent to a single high-bandwidth coherent receiver described in Fig. 4.19. The light from the channel is mixed with that of a local oscillator into a 90° hybrid whose outputs feed four balanced photodiodes pairs with 70-GHz bandwidth. Their electrical signals are sampled at 160 GS/s by the four heads of a real-time Keysight Technologies oscilloscope, forming a four-channel

analog-to-digital converter having a 62.5 GHz electrical bandwidth. For each measurement, ten different sets of 40 µs duration are stored and processed off-line. After frontend adjustments, resampling and chromatic dispersion (CD) compensation, a data-aided channel estimation is performed at startup in order to determine the phase mismatch between the sub bands composing the transmitted channel. After applying the phase mismatch compensation (PMC), the T/2-spaced 51 taps Multi-Modulus Algorithm (MIMO 2x2) is used to demultiplex both polarizations and compensates for residual phase difference between the sub-bands. Next, frequency offset compensation and blind search carrier phase recovery are performed. The recovered signals undergo T-spaced 121 taps post-equalization (LMS-DD) to mitigate transmitter impairments. Bit error ratio (BER) is finally computed, and subsequently converted into Q²-factor.

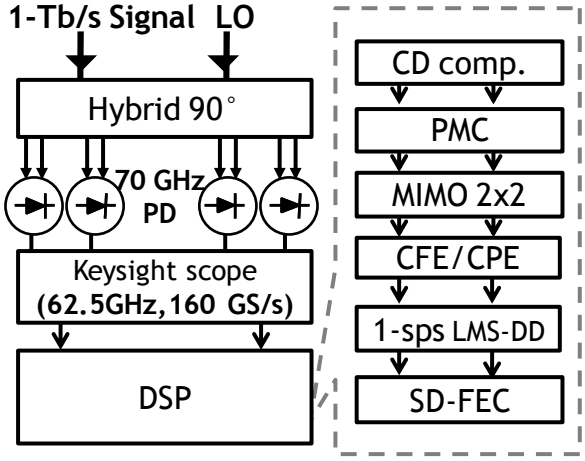

Fig. 4.19: Coherent receiver including DSP.

Fig. 4.20 (left) shows the probability density function of the real component of the received symbols in one polarization in the high OSNR region for the PDM-32QAM signal. We can observe the occurrence of the six amplitudes of the modified 6PAM signal with outer amplitudes having 33% less probability than four inner ones. Fig. 4.20 (right) then shows the performance statistics obtained at high OSNR (> 40dB) with and without using the PMC. This figure clearly shows that processing the PMC is mandatory to enable satisfying convergence of the MMA and thus avoid performance degradation.

Using the PMC, Fig. 4.21 (left) now shows the Q²-factor versus OSNR for the 124GBd channel modulated with PDM-16QAM and PDM-32QAM, generated respectively from 4PAM and modified 6PAM followed by PAM-to-QAM converter and PDM emulation as described previously. Dashed lines represent theoretical expectations. Squares and circles represent PDM-16QAM and PDM-32QAM results. Contrary to 16QAM which exhibits OSNR penalty around 4.5 dB at Q²-factor of 5 dB,

the 32QAM exhibits a much higher penalty around 8 dB as well as performance saturation at 6.1 dB of Q²-factor. To get a better insight on the achievable information capacity, mutual information between transmitted and received signals is calculated and Fig. 4.21 (right) now shows the measured performance in terms of mutual information (bits in left axis) and the product between mutual information and symbol rate (Gb/s in right axis). We included as well the theoretical expectations (dashed lines) for each format, also known as constellation constrained capacity. These results show the maximum number of bits per symbol (left axis) or bits per second at 124 GBd (right axis) that can be transported theoretically (dashed lines) and experimentally with our sub band transmitter (lines with markers). Although 32QAM is slightly outperformed by 16QAM for mutual information below 7 bit/symbol due to much higher implementation penalties, it outperforms 16QAM above 7 bit/symbol and exhibits a maximum capacity of 9.3 bit/symbol (1.15 Tb/s). Particularly, it exceeds the minimum required mutual information of 8.1 bit/symbol for the transport of 1 Tb/s at 124 GBd.

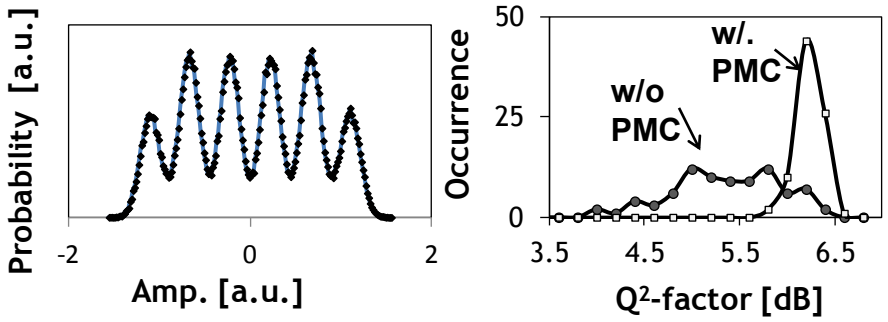

Fig. 4.20: Left: probability density function of received symbols, right: impact of phase mismatch compensation (PMC) stage on stability.

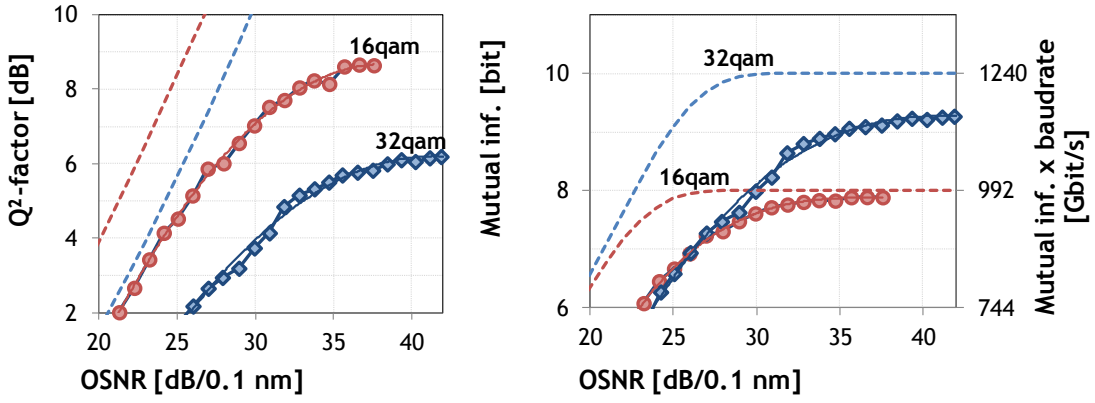

Fig. 4.21: Left: Q^2-factor vs OSNR at 124GBd, right: mutual information and information rate vs OSNR.

To validate the transmitter design, including TX/RX signal processing, we demonstrate the transmission of the 1 Tb/s signal over a long-haul distance using the setup described in Fig. 4.22 (left). As shown in the figure, the signal from the transmitter is inserted into a 125-GHz slot, boosted through an EDFA and transmitted together with forty four 50-GHz spaced PDM-16QAM channels modulated at 49 GBd used for amplifier loading. Each span of the transmission line is 55km-long and is made of pure silica ultra large area fiber having attenuation of 0.16 dB/km. Fiber losses are compensated by EDFAs. At the receiver end, our 1 Tb/s net data rate channel is sent into our coherent receiver and processed off line.

After coherent demodulation, the signal enters a 24 % overhead SD-FEC. We employ here a simple bit-interleaved coded modulation setting and use a spatially coupled low-density parity-check (LDPC) convolutional code with syndrome former memory μ=1, as detailed in [102]. The designed 24 % overhead SD-FEC leads to a limit of operation of 4.75 dB Q²-factor, as shown in Fig. 4.23 (left). Then, Fig. 4.23 (right) shows the measured Q²-factor (max, average, min) versus distance. Performance is always above FEC limit for distances up to 660 km and all 10 independent measured waveforms containing each $2 \cdot 10^6$ symbols are decoded error-free by our SD-FEC.

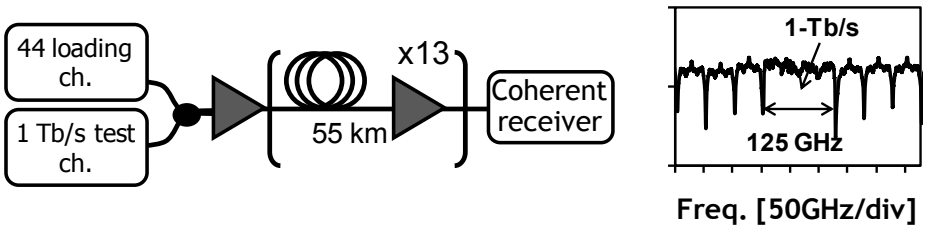

Fig. 4.22: Left: Transmission setup, right: WDM spectrum.

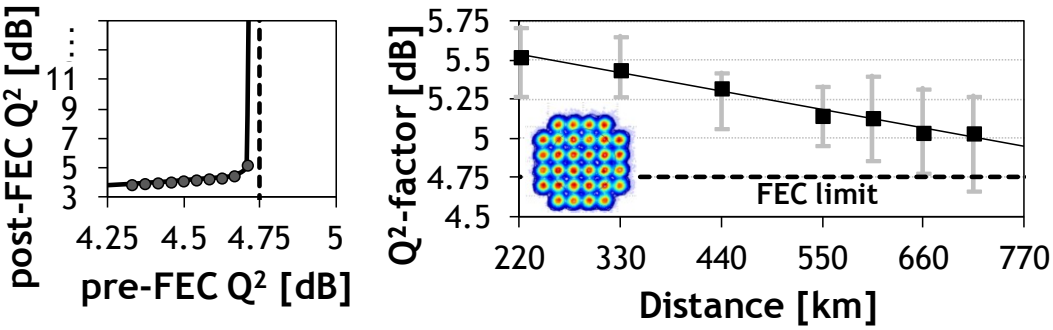

Fig. 4.23: Left: SD-FEC performance, right: transmission performance.

Here, we demonstrated the generation and transmission of a record 1-Tb/s net data rate single-carrier signal with 8 b/s/Hz using Nyquist pulse shaping, PDM-32QAM modulation and parallel spectral sub band generation. Using a phase

mismatch compensation processing within our 62.5-GHz coherent receiver, we transmitted successfully the single-carrier 124-GBd signal over 660 km using a 24 % overhead spatially coupled LDPC.

4.3.1 Sub-band single carrier vs super-channel

In the previous experiment, we used multiple low-bandwidth DAC and modulators at the transmitter to generate a very high symbol rate signal. This signal could be detected by a single coherent receiver with the same digital signal processing as the one used by a high symbol rate single carrier receiver. However, another option would be using multiple independent transmitters and receivers to generate and detect signals at a lower symbol rate. We refer to the first approach as sub-band single-carrier and to the second as super-channel. One potential advantage of the sub-band technique is the better spectral utilization since there is no guard-band between the sub-bands generated by each DAC. Super-channels, on the other hand, usually require guard-band to avoid overlap between neighbouring channels. Nevertheless, super-channels have a less complex transmitter setup since it does not require careful synchronization between channels.

Here, we compare experimentally these two solutions, namely super-channel and sub-band single-carrier, at 400 Gb/s and 800 Gb/s [104]. Since we compare both solutions at the same bitrate, we can exploit the higher spectral utilization of the sub-band single-carrier solution to increase its FEC overhead with respect to the super-channel solution.

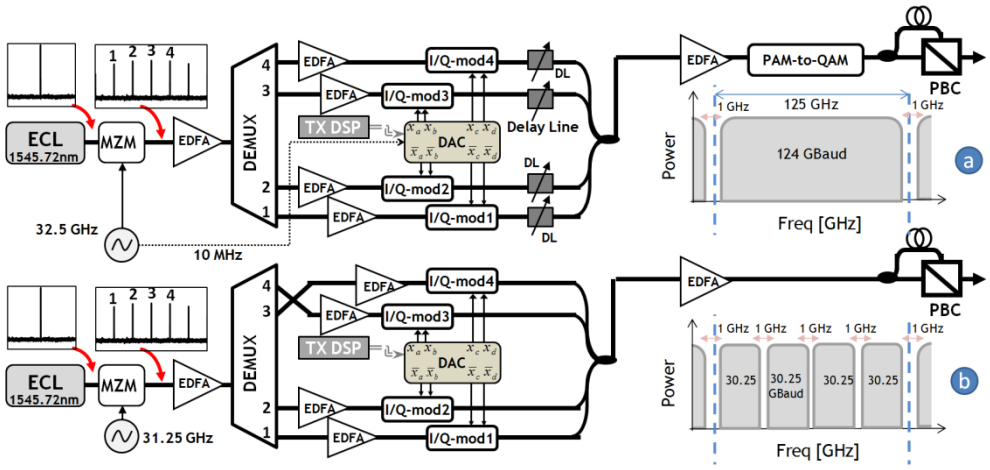

Fig. 4.24: a) Single-carrier generation based on sub-band transmitter and b) super-channel transmitter.

Using off-the-shelf components, we experimentally evaluate both solutions in terms of implementation penalties and forward error correction (FEC) limit. The two solutions we compare are shown in Fig. 4.24. The inset (a) depicts the desired

spectrum of the single-carrier approach at very high baud-rate. Pulse shaping with roll-off approaching zero is employed (~1/1000), so the 124 GBd signal occupies roughly 124 GHz and can be inserted in a 125 GHz slot with 1 GHz only guard-band. Using the same channel slot (125 GHz) and guard-band of 1 GHz, we show in inset (b) the desired spectrum of the super-channel solution based on 4 independent sub-channels. In the first solution (a), we have a higher utilisation of the spectrum (124 GHz compared to a total of 121 GHz for the super-channel) which will be used to increase the overhead for FEC.

As shown in Fig. 4.24 (a), the main idea of the sub-banded transmitter (top transmitter) is to divide the total spectrum into four spectral sub-bands which are generated in parallel before being recombined as detailed in section 4.3. Here, we generate 2PAM and 4PAM in order to obtain PDM-QPSK and PDM-16QAM (respectively) after PAM to QAM conversion and PDM emulation.

For the super-channel generation, the transmitter is modified as shown in the bottom of Fig. 4.24. We set the external clock frequency to 31.25 GHz to produce a comb corresponding to sub-channel spacing as in inset (b) of Fig. 4.24. We load in DAC memory sequences corresponding to independent 30.25 GBd 16QAM (respectively. QPSK) signal. We switch outputs 3/4 of demux to ensure neighbouring channels with correlated data from complementary DAC outputs are correctly interleaved avoiding inter-channel correlation. Finally we short-circuit the PAM-to-QAM converter, which is not necessary for the super-channel generation. In addition, fine synchronization between frequency of the comb generator and DAC is not needed anymore nor time alignment between signals generated by different modulators. At the output of this transmitter we have our super-channel made of 4 independent sub-channels which can be also inserted in a 125 GHz slot.

We first evaluated the back-to-back performance versus the optical signal-to-noise ratio (OSNR) of the two studied formats (QPSK and 16QAM) in the two configurations (single-carrier and super-channel). Results obtained with the same coherent receiver detailed in last section (70 GHz photodiodes and a single 4-channel 63-GHz bandwidth 160 GS/s oscilloscope) are depicted in Fig. 4.25 (top). Squares represent PDM-QPSK performance and dashed lines correspond to theoretical expectations. OSNR penalty with respect to theory is around 1 dB for both solutions for Q^2-factors below 5 dBQ, however the super-channel solution (4x30.25 GBd, empty squares) has slightly higher performance in the high-OSNR region. Line rate can be doubled by using 16QAM, represented Fig. 4.25 by circles. Single-carrier 124 GBd PDM-16QAM (empty circles) suffers from high implementation penalties of around 4 dB with respect to theory at 5 dBQ due to lower tolerance of 16QAM to

transmitter imperfections at such high line-rate (992 Gb/s). On the other hand, the super-channel scheme (filled circles) is only 1.5 dB away from theoretical expectations.

One benefit of single-carrier based on the sub-band transmitter is the reduced spectral loss due to guard-band compared to the super-channel approach. Therefore, the extra bits can be used to increase the FEC overhead from 21% (super-channel) to 24% (single-carrier). Considering these overheads, a net data-rate of 400 Gb/s is achieved with QPSK modulation and 800 Gb/s with 16QAM. Fig. 4.25 (bottom) shows performance obtained with spatially-coupled low-density party check (LDPC) code for both overheads, considering the two studied formats. We show post-FEC BER as a function of SNR, and we obtain SNR limit for error-free operation around 4.8 dB and 5.1 dB for QPSK. Higher overhead FEC (24%) also provides 0.3 dB lower SNR-limit for 16-QAM and Q^2-limits of around 4.8 dBQ and 5.1 dBQ are found for 24% and 21% overhead respectively for both formats.

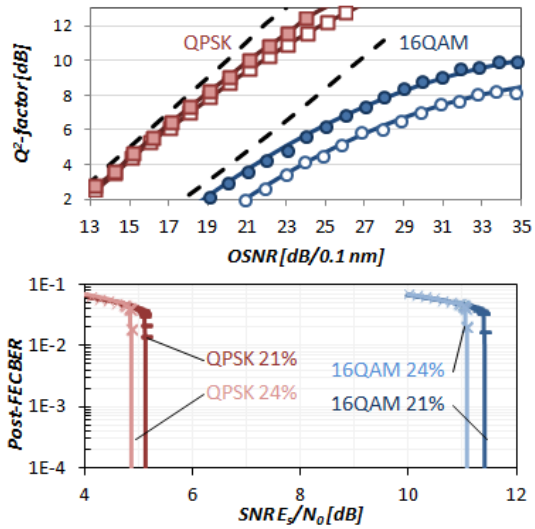

Fig. 4.25: Top: Back-to-back results. Empty markers represent sub-band signal and filled markers represent super-channel. Bottom: FEC performance.

Afterwards, we performed a transmission experiment using a re-circulating loop detailed in Fig. 4.26 consisting of four 100km-long spans of SSMF. No dispersion-compensating fiber is used here and hybrid Raman-EDFA optical repeaters compensates for fiber losses. The Raman pre-amplifier is designed to provide ~10dB on-off gain. Dynamic gain equalization (DGE) is performed thanks to a flex-grid wavelength selective switch inserted at the end of the loop. Our channel is inserted in a 125 GHz slot, and seventy 49 GBd loading channels are used for WDM emulation in 50 GHz grid. Additional 4 neighbours are added in both sides of the test channel for emulation of spacing close to symbol rate as shown in the inset of Fig. 4.26.

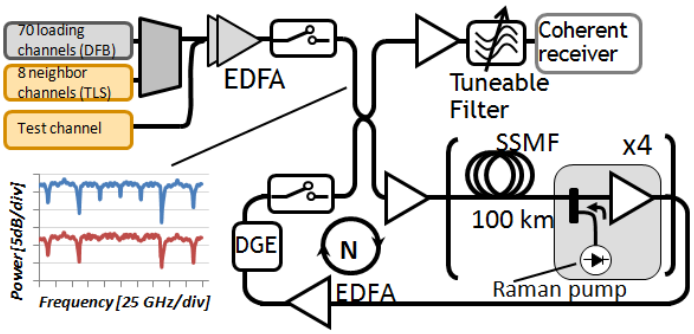

Fig. 4.26: Transmission setup.

After 6400 km (QPSK) and 800 km (16QAM), we varied the launch power at each fiber span input by changing the output power of the EDFAs and measured the average performance of the super-channel (filled markers) and single-carrier based on sub-band transmitter (empty markers) as shown in Fig. 4.27 (left). We included the corresponding expected FEC limits to compare performance margins for both solutions. Dashed lines correspond to soft-FEC limit for 24% overhead while dash-dot line represent limit for 21% overhead, providing both solutions a constant information rate of 400 or 800 Gb/s. Left curve shows PDM-QPSK performance after 6400 km (16 loops). At low launch power, corresponding to the linear regime, both solutions perform similarly as predicted by the back-to-back results. However, optimum launch power for super-channel (filled squares) was found to be 1 dB higher than single-carrier and it achieves a slightly higher maximum performance of near 7dBQ. Nevertheless, single-carrier (empty squares) can still provide the same performance margin of 1.8 dB as a result of its lower FEC limit. Consequently, for 400 Gb/s transport both solutions provide comparable operation margin.

We proceeded by evaluating PDM-16QAM performance after 800 km as shown in Fig. 4.27 (right). Super-channel back-to-back advantage is maintained after transmission and single-carrier performance is always below due to higher implementation penalties. Results indicate similar optimum launch power for single-carrier and super-channel. Next, we calculated the performance margins at the optimum launch power, and 1.5 dB and 1.9 dB was observed for the single-carrier and super-channel, respectively. Therefore, the higher coding gain due to empowered FEC for the single-carrier solution (empty circles/dashed line) is not sufficient to compensate for its lower maximum performance compared to super-channel for 800 Gb/s transport.

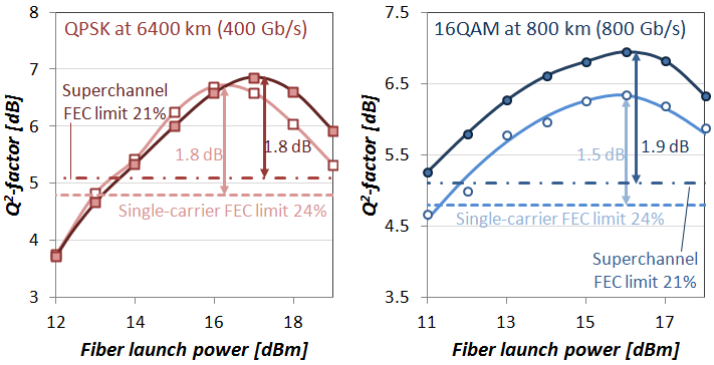

Fig. 4.27: Non-linear tolerance. Empty markers represent sub-band signal and filled markers represent super-channel

In summary, we compared two solutions, namely super-channel and sub-band single-carrier, at 400 Gb/s and 800 Gb/s. These results show that the sub-band single carrier solution is competitive compared to the super-channel with QPSK modulation at 400 Gb/s. However, there is still room for improvement when 16QAM is used. The very complex transmitter setup explains the 16QAM extra penalties and performance improvement is expected with integrated components (demux + array of modulators + coherent sub-band coupling). In addition, the use of an 8-output synchronized DAC may also increase performance as PAM-to-QAM emulation can be avoided.

4.4. *Summary*

In this chapter, we have investigated the generation and detection (including enhanced signal processing) of very high symbol rate signals, notably 64 GBd and 124 GBd. We started the chapter investigating a signal processing algorithm that compensates and estimates receiver skew in coherent receivers. This algorithm is particularly attractive for high symbol rate signals, which are less tolerant to receiver skew. Skew digital compensation can thus alleviate requirements on coherent receiver reciver skew. Afterwards, we investigated and demonstrated the first single-carrier 400 Gb/s transmission over transatlantic distances. To achieve this result, we relied on two technological trends: the continuous increase of bandwidth of opto-electronics enabling the generation and detection of a 64 GBd signal, and the continuous increase of available computational power which may enable more complex signal processing algorithms and channel coding in future transponder generations. To illustrate these trends, we employed state-of-the-art high bandwidth components paired with enhanced signal processing algorithms and FEC to improve performance. Particularly, filtered digital backpropagation improved performance in

terms of Q^2-factor by 0.5 dB in average, and overhead-optimized spatially-coupled LDPC operated only 1 dB away from the 16QAM constellation constrained capacity. Combining all the mentioned techniques, we demonstrated for the first time 400 Gb/s single carrier transmission over 6600 km at 6 b/s/Hz and over 7200 km at 5.3 b/s/Hz. Subsequently, we described high symbol rate signal generation based on parallel synthesis of multiple sub-bands generated by low-bandwidth synchronized transmitters. Using a sub-band transmitter, we generated a record 124 GBd PDM-32QAM signal. Despite penalty of around 8 dB compared to theoretical expectations, we demonstrated a record 1 Tb/s net-data rate detection using 24% overhead code based on spatially-coupled LDPC. Afterwards, we compared sub-band single carrier with conventional super-channel at fixed bitrate. Particularly, sub-band single carrier higher spectrum utilization enabled slightly higher FEC overhead. Despite the challenging sub-band transmitter setup, we obtained similar performance at 400 Gb/s (QPSK) and slightly lower performance at 800 Gb/s (16QAM). This demonstrates the feasibility of the sub-band transmitter approach, which is attractive to increase the symbol rate well beyond the bandwidth of current optoelectronic devices.

Conclusions

In this thesis, I have investigated advanced modulation formats and signal processing for high speed spectrally efficient optical communications. Such high speeds are required in the near future to cope with the ever-increasing traffic growth in core networks. Here, signal processing and information theory tools were used to design and optimize high-capacity and highly flexible transponders. Particularly, I focused on modulation format optimization under constraints of signal processing and FEC practical implementation. Then, transponder flexibility, which is one of the key requirements for next-generation optical networks, was also investigated. To improve transponder flexibility and receiver sensitivity, the use of modulation formats such as time-interleaved hybrid modulation formats and 4-dimensional modulation formats was studied. To conclude the thesis, a special attention was paid to transponders operating at 400 Gb/s and 1 Tb/s based on high symbol rate signals paired with enhanced signal processing.

Chapters 1 and 2 describe fundamental notions of digital communications, information theory, long-haul high speed optical communications systems, and digital signal processing were revisited. Notably, thanks to the widespread use of transmission links without inline dispersion compensation, the equivalent channel after transmission can be modeled by a Gaussian linear channel with 4 dimensions. This elegant model can accurately predict experimental performance not only in the linear regime but, more interestingly, also in the nonlinear regime. As a result, the powerful tools from information theory such as (generalized) mutual information can be used to quantify the maximum achievable information rate after transmission and compare different solutions. Moreover, the Gaussian noise assumption greatly

simplifies the study of receiver signal processing algorithms. These algorithms rely on well established tools from estimation theory under Gaussian noise and can be adapted to fiber optics transmission.

Relying on the aforementioned tools of signal processing and information theory, modulation format optimization for spectrally efficient long-haul optical systems was investigated. The main results related to modulation formats are the following. First, it was experimentally demonstrated that Circular-8QAM provides reach increase compared to Star-8QAM over links without inline dispersion compensation despite lower tolerance to frequency and phase impairments. Circular-8QAM has indeed a larger minimum Euclidean distance than Star-8QAM, thus it provides a better performance if the phase is correctly recovered. Afterwards, I included Rect-8QAM, 8PSK and 8SP16QAM constellations in the analysis, and I focused on achievable information rate comparison assuming the use of pragmatic BICM SD-FEC schemes without iterative demapping. These FEC schemes provide a good trade-off between performance and implementation complexity and are ideal for practical implementation. The most appropriate metric to quantify the achievable information rate of systems based on these FEC schemes is the generalized mutual information. The generalized mutual information depends not only on the minimum Euclidean distance of the tested constellation but also on the bit mapping. To maximize generalized mutual information, Gray mapping is particularly attractive because there is negligible information loss compared to the conventional mutual information metric. However, 8QAM constellations with Gray mapping such as Rect-8QAM and 8PSK have poor minimum Euclidean distance. Nevertheless, Rect-8QAM was shown to outperform other 8QAM constellations in the low code rate region. More specifically, it was demonstrated that there are three different regions with three corresponding formats that maximize generalized mutual information. The low code rate, intermediate code rate and high code rate regions which are optimized by Rect-8QAM, 8SP16QAM and Circular-8QAM, respectively. In essence, it became clear that for high signal-to-noise ratio high minimum Euclidean is the important metric to be considered, however for low signal-to-noise ratio performance depends on FEC implementation. In the case of BICM SD-FEC without iterative demapping, mapping plays an important role and should also be included in the analysis with Gray mapping being particularly attractive.

Subsequently, modulation formats capable of spectral efficiency fine tuning to increase transponder flexibility were investigated. Flexibility may be indeed one of the key features of future transponders. Particularly, we compared two solutions attracting much attention in the scientific community: time-interleaved hybrid formats and 4D modulation formats. The theory of both these solutions was developed,

followed by experimental verification. As an illustration, it was experimentally demonstrated that 4D-32SPQAM and Hybrid-QPSK/8QAM provide an intermediate reach in between PDM-QPSK and PDM-8QAM. In addition 4D-32SPQAM is attractive to provide reach increase compared to Hybrid-QPSK/8QAM for high pre-FEC Q^2-factor, however this advantage is reduced when lower FEC Q^2-factor limits are considered corresponding to the use of more powerful FEC codes. This is explained by the fact that 4D modulation formats are by design based in a denser lattice, hence they have a better minimum Euclidean distance than hybrid formats. On the contrary, when we move to lower signal-to-noise ratio mapping becomes important and hybrid formats become competitive again. Besides, since it was observed that the highest gains brought by 4D formats are achieved at high pre-FEC Q^2-factor, a novel use of 4D formats was proposed in this thesis: intensity modulation direct-detection short-reach systems based on 4-PAM operating at 100 Gb/s. To reduce cost, these systems rely on low-complexity FEC which is also advantageous to keep latency low. These low-cost systems at 100 Gb/s have been under active research to cope with the rapid traffic growth specially in data centers. To illustrate the 4D concept in such scenarios, it was experimentally demonstrated that 4D-Coded 4-PAM provided up to 1 dB better sensitivity over conventional 1D 4-PAM when paired with low complexity hard-decision FEC.

Afterwards, I moved to the design and optimization of transponders based on high symbol rate signals (beyond 60 GBd) aiming long-haul transmission. Operation at such high symbol rates has the potential to reduce the cost per transmitted bit as more capacity can be delivered by a single transponder. However, high symbol rate signals are less tolerant to transmitter and receiver impairments. Among these imperfections, I tackled the issue of receiver skew imperfection in the presence of large accumulated dispersion, which is particularly harmful for high symbol rate signals. I proposed and demonstrated a novel blind equalizer architecture based on independent chromatic dispersion compensation to avoid mixing between in-phase and quadrature received signal components followed by 4x2 multiple-input multiple-output adaptive filter. This adaptive equalizer was also shown to provide accurate skew estimation derived from converged equalizer coefficients. Ultimately, after minimizing transmitter and receiver imperfections, two record experiments based on high symbol rate signals were demonstrated. The first 400 Gb/s single carrier transmission over more than 6600 km was demonstrated based on 16QAM operating at 64 GBd. This result was achieved using: state-of the art 8-bit 88 GS/s DAC; intersymbol interference mitigation based on optical filtering and receiver signal processing; joint symbol rate and spatially-coupled FEC overhead optimization; as well as nonlinear mitigation using filtered digital backpropagation. This result paves

the way for future commercial single-carrier 400 Gb/s systems, based on high-speed opto-electronics paired with advanced signal processing and FEC. Finally, the first 1 Terabit/s net data rate transmission based on parallel synthesis of four sub-bands was demonstrated to achieve a record 124 GBd 32QAM signal. This technique opens the door for the generation of signals with symbol rates well beyond the bandwidth of current opto-electronic devices.

Acknowledgements

This thesis would not be possible without the support of all my colleagues at Bell Labs who were by my side for the whole 3 years of my thesis work and even before during my 6 months internship. So first I would like to thank all of them. Thanks to all the colleagues who provided helpful suggestions on presentations, papers and ideas. Thanks to all the colleagues who helped me a lot in the lab, all the experimental results in this thesis which are the core of this work depended on the hard work of every one of you guys.

Thanks to Gabriel Charlet for the great discussions, advice and particularly pushing me to achieve great results. Thanks to my academic advisors for the support. And the biggest thank you message goes to Jérémie Renaudier, my adviser in Bell Labs. Thank you Jérémie for everything, I can't think of a better adviser than you. Thanks for all the advice on writing papers, the quality of the papers I have written would not be the same without you. Thank you for believing in my ideas when others thought it would not work. Thank you for teaching me so many things about optical communications, signal processing and laboratory work. After more than 3 years working with you, to continue in Bell Labs as a full-time researcher in your group was the easiest choice to make.

Also, thanks to Gabriella Bosco and Magnus Karlsson for reviewing my thesis. It was an honor to have you as reviewers and in my defense committee. Thanks for all the members of the defense committee, I appreciate you took the time to come to Paris to attend my defense, read the manuscript and ask insightful questions during the defense. A special thanks to Darli Mello for coming from Brazil

to the defense and also for the suggestions to improve the manuscript. You Darli were the first to teach me optical communications in University of Brasilia a few years ago and doing an internship in your lab is one of the main reasons I now work as a researcher in optical communications.

Finally, thanks to my friends and family. Having all of you made things a lot easier. Thanks to my mom Dione, I would not be doing a PhD in France if was not for you, you are the best. You do the possible and impossible to make your son happy and I will be forever grateful. Thanks to my dad Marinho and my sister Mariana, there is not a single day that I do not feel “saudade” of you.

Résumé en Français

Depuis les dernières décennies, l'Internet est passé d'un petit réseau entre instituts de recherche à une infrastructure globale. Les applications Internet ont évolué passant de services simples comme le partage de fichiers et courrier électronique aux services beaucoup plus complexes comme la vidéo en demande, les jeux en ligne, les communications entre objets, etc. Ces nouvelles applications demandent des vitesses de transmission croissantes. De plus, le nombre de nœuds réseau qui étaient de l'ordre de millions dans les années 90 est maintenant dans l'ordre des milliards. Avec l'ascension de l'Internet des objets, le nombre des nœuds va bientôt atteindre la dizaine de milliards. Pour supporter la croissance exponentielle du trafic, des réseaux cœur avec les débits toujours croissants sont nécessaires. Actuellement, les réseaux cœur se basent sur les communications sur fibre optique et la capacité et portée de ces réseaux optiques ont augmentés dans les dernières décennies grâce à plusieurs nouvelles technologies: les fibres à faible perte, les amplificateurs optiques, le multiplexage par longueur d'onde, le multiplexage de polarisation, la détection cohérente, le traitement numérique du signal, les formats de modulation avancés, etc. Les débits qui étaient 2.5 gigabit par second par canal sur des distances transatlantiques dans les années 90 ont augmenté jusqu'à 100 gigabit par seconde dans les années 2010. De plus, le multiplexage par longueur d'onde permet la transmission d'environ 100 canaux par fibre optique résultant en capacité de l'ordre de 10 térabit par second par fibre.

Actuellement, la détection cohérente combinée avec le traitement numérique du signal est le standard pour les transmissions dépassant 1000 km à haute capacité sur les fibres optiques à 100 gigabit par seconde. Avec l'essor des convertisseurs à haute fréquence d'échantillonnage et haut résolution, la génération des formats de modulation avec les filtres de mise en forme ont aussi permis l'augmentation du débit par canal ainsi que la densité spectrale

Dans cette thèse, les formats de modulation et traitement du signal pour les systèmes de communications optiques haut débit et forte densité spectrale ont été étudiés (Fig. 0.1). Les débits élevés sont nécessaires dans le futur proche pour répondre à la demande croissante dans les réseaux cœur de télécommunications. Dans ce manuscrit, des outils de la théorie de l'information et du traitement du signal ont été utilisés pour la conception d'émetteurs et récepteurs flexibles en débit attendant des débits de l'ordre du térabit par seconde. Particulièrement, je me suis intéressé à l'optimisation de formats de modulation considérant des contraintes pratiques liées au traitement du signal et les codes correcteurs d'erreurs. Ensuite, la flexibilité en débit, qui est une des principales exigences de réseaux optiques de prochaine génération, a été aussi examinée. Afin d'améliorer la flexibilité des systèmes optiques ainsi que la sensitivité des récepteurs, l'emploi de formats de modulations entrelacés dans le temps (« hybrides ») ainsi que les formats de modulation à 4 dimensions ont été étudiés. Pour finaliser la thèse, je me suis concentré à la conception d'émetteurs à 400 gigabit par seconde et 1 térabit par seconde, basés sur les signaux à rythme symbole très élevé et le traitement du signal avancé.

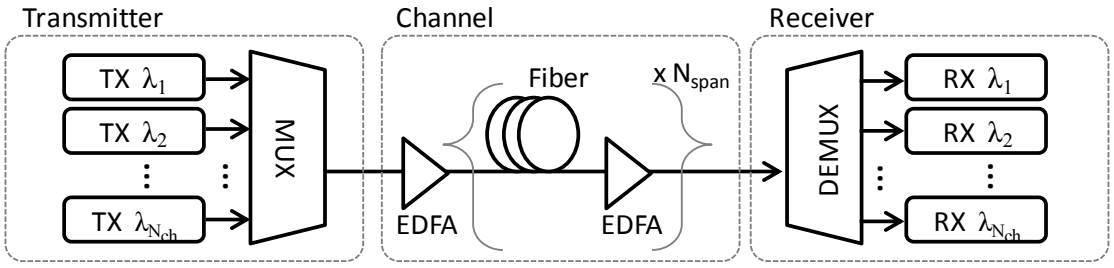

Fig. 0.1: Système de communication sur fibre optique avec amplification optique et multiplexage par longueur d'onde.

Les chapitres 1 et 2 décrivent quelques notions fondamentales: la théorie de communications numériques, la théorie de l'information, les systèmes de communications optiques à débits élevés visant les distances de transmission dépassant 1000 kilomètres et le traitement numérique du signal. Notamment, j'ai montré que grâce à l'utilisation massive de liens de transmission sans compensation

de la dispersion chromatique en ligne, le canal équivalent après transmission et détection cohérente peut être modélisé par un canal Gaussian à 4 dimensions (Fig. 0.2). Le modèle peut prédire la performance pas seulement dans le régime linéaire de transmission mais aussi dans le régime non-linéaire. Par conséquent, les outils puissants de la théorie de l'information peuvent être utilisés pour quantifier le débit maximum possible de différentes solutions. En outre, l'approximation Gaussienne simplifie énormément l'étude des algorithmes de traitement du signal présents à la réception. Ces algorithmes s'appuient sur les outils de la théorie de l'estimation avec la présence de bruit additive Gaussian et peuvent être adaptés aux transmissions sur fibre optique.

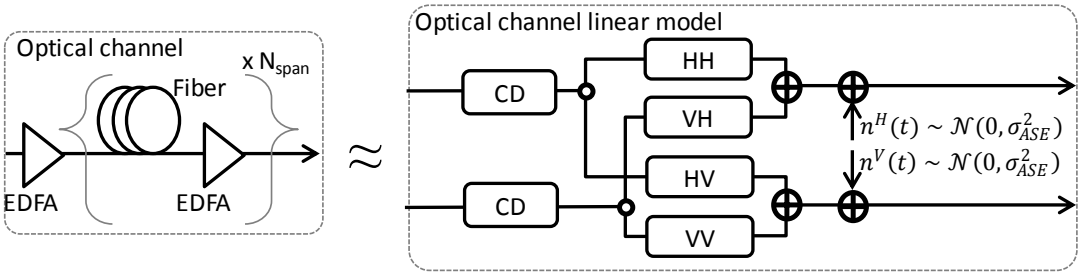

Fig. 0.2: Modèle de canal considérant 4 dimension plus bruit additif.

En s'appuyant sur ces outils de traitement du signal et théorie de l'information, l'optimisation de formats de modulation pour les systèmes de communications optiques longue distance à forte densité spectrale a été analysée. Les principaux résultats liés aux formats de modulation sont les suivants. Premièrement, on a démontré expérimentalement que le « Circular-8QAM » atteint une distance de transmission plus longue que le « Star-8QAM » considérant les liens sans compensation en ligne de la dispersion chromatique malgré une tolérance inferieure aux effets de fréquence et phase (Fig. 0.3). Le « Circular-8QAM » a en effet une distance Euclidienne minimale plus grande que le «Star-8QAM », résultant en une meilleure performance supposant que les distorsions de phase sont correctement compensées.

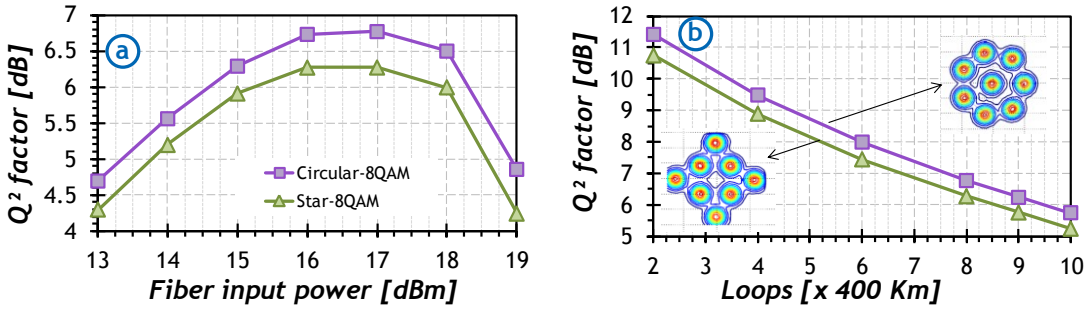

Fig. 0.3: Circular-8QAM vs. Star-8QAM. a) Performance à distance fixe et à puissance de transmission variable. b)Performance en fonction de la distance.

Ensuite, les formats « Rect-8QAM », “8PSK” et “8SP16QAM” ont été aussi considérés dans l’analyse, et je me suis concentré à la comparaison des différents formats en termes de débit maximale possible considérant l’usage des codes correcteurs d’erreur pragmatiques du type « BICM » à décision souple sans démodulation itérative. Ces codes fournissent un bon compromis entre performance et complexité de mise en œuvre et sont très populaires pour les implémentations pratiques. La métrique la plus approprié pour quantifiée le débit possible de ces codes est l’information mutuelle généralisée. Cette métrique ne dépend pas seulement de la distance Euclidienne minimale du format considéré mais aussi du choix du codage bit/symbole. Pour maximiser l’information mutuelle généralisée, le codage Gray est particulièrement intéressant parce que ce codage présent une perte d’information négligeable venant du codage bit/symbole. Pourtant, les formats « 8QAM » avec codage Gray ont des distances Euclidiennes minimales plus petites par rapport aux formats qui ne permettent pas le codage Gray. Malgré ça, le « Rect-8QAM » présente une meilleure performance que les autres options dans la région de basse efficacité spectrale. Plus précisément, on a montré l’existence de trois régions correspondant à trois formats différents qui maximisent l’information mutuelle généralisée pour chaque région. Les régions à basse/moyenne/haute efficacité spectrale qui sont optimisées par le « Rect-8QAM », « 8SP16QAM » et « Circular-8QAM » respectivement (Fig. 0.4). Essentiellement, il est devenu évident que pour les rapports signal-à-bruit élevés la distance Euclidienne minimale est la métrique importante à considérer, par contre pour les rapports signal-à-bruit bas, la performance dépend de l’implémentation du code correcteur d’erreur. Dans le cas des codes du type « BICM » à décision souple sans démodulation itérative, le codage bit/symbole joue un rôle important est doit être inclus dans l’analyse et le codage Gray est particulièrement intéressant.

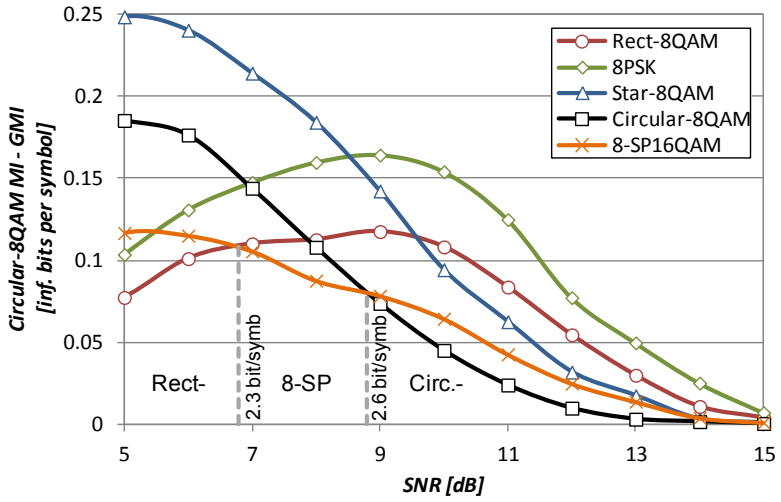

Fig. 0.4: 3 régions avec 3 formats correspondants qui maximise le débit maximale possible en fonction du rapport signal-à-bruit (axis y représente la perte par rapport à l'optimal, donc le plus petite la perte le mieux).

Postérieurement, les formats de modulation capables d'adapter de manière fine la densité spectrale de transmission ont été étudiés. La flexibilité est en effet un des éléments clés des systèmes de prochaine génération. Plus précisément, on a comparé 2 solutions qui suscitent beaucoup d'intérêt de la communauté scientifique : les formats de modulation à entrelacement temporelle dits « hybrides » et les formats de modulation à 4 dimensions. La théorie relative aux deux formats a été développée et ensuite la validation expérimentale a été décrite. Pour illustrer le concept, on a démontré que le « 4D-32SPQAM » et le « Hybrid-QPSK/8QAM » permettent une portée de transmission intermédiaire entre les solutions classiques « QPSK » et « 8QAM ». De plus, le « 4D-32SPQAM » présente une meilleure performance particulièrement pour les distances plus courtes (rapport signal à bruit élevé). Par contre, cet avantage déviant plus petit pour les distances plus longues correspondant à l'usage des codes correcteurs d'erreurs plus puissantes (Fig. 0.5). On peut explique ce comportement par le fait que le format 4D est conçu à partir d'un « lattice » plus dense, résultant une plus grande distance Euclidienne minimale que celle des formats « hybrides ». Néanmoins, quand on vise les rapports signal-à-bruit plus bas, le codage bit/symbole déviant plus important donc les formats « hybrides » deviennent compétitifs encore une fois.

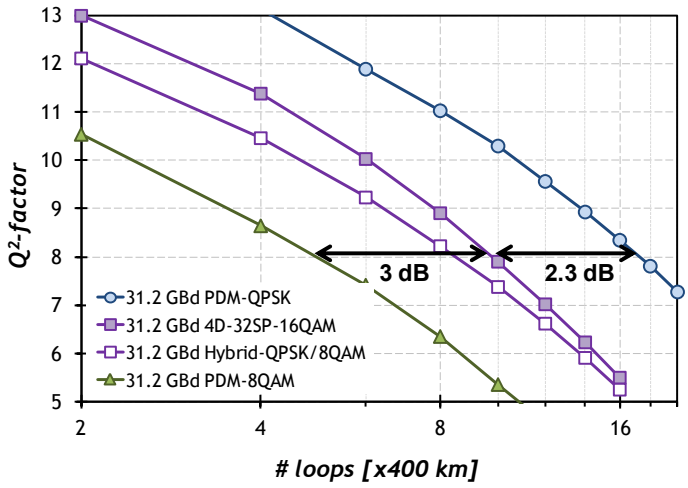

Fig. 0.5: QPSK vs 4D vs hybrid vs 8QAM. L'avantage du 4D par rapport au format hybride réduit avec la distance.

De plus, puisque on a observé que les gains apportés par les formats 4D sont plus grands à fort rapport signal-à-bruit, on a proposé une nouvelle application pour les formats 4D dans cette thèse : les systèmes bas cout à distance courte basés sur la modulation d'intensité et la détection quadratique. Pour réduire le cout, ces systèmes comptent sur les codes correcteurs d'erreurs à faible complexité (codes à latence petite aussi). Ces systèmes à petit cout à 100 gigabit par seconde représentent une participation importante de la recherche en communications optiques grâce à l'explosion du trafic dans les centres des donnés. Pour illustrer le concept basé sur la modulation 4D appliqué a ce nouveau scenario, on a démontré expérimentalement que le « 4D-coded PAM4 » apporte jusqu'a 1 dB (Fig. 0.6) en gain de sensitivité par rapport aux systèmes basés sur le « PAM4 » traditionnel quand associé aux codes correcteurs d'erreurs à faible complexité (décision à seuil).

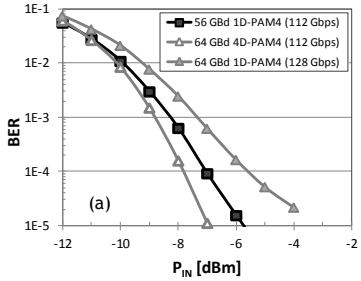

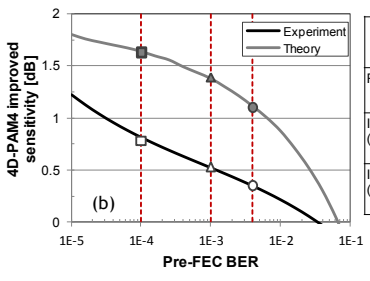

	FEC limit	4D impr. sens. (exp.)	4D impr. sens. (th.)	Block size
RS (255,239)	10^{-4}	0.8 dB	1.65 dB	255
Interleaved RS (2720,2550)	10^{-3}	0.55 dB	1.4 dB	2720
Interleaved BCH (522240,489472)	$4 \cdot 10^{-3}$	0.35 dB	1.1 dB	522240

(c)

Fig. 0.6: a) Performance en fonction de la puissance (PAM4 56 Gbaud vs 4D-coded PAM4 64 Gbaud vs PAM4 64 Gbaud) b) Gain 4D versus performance : théorie et expérience. C) Table récapitulative.

Ensuite, j'ai exploré la conception et optimisation des émetteurs et récepteurs à rythme symbole élevé (au-delà de 60 gigabaud) visant les transmissions longues distances. Des rythmes symbole aussi élevés présentent une opportunité pour réduire le coût des transmissions puisque les débits plus élevés peuvent être offerts par un seul pair émetteur/récepteur. Cependant, les signaux à rythme symbole élevé tolèrent moins bien les distorsions présentes dans la chaine de transmission. Parmi ces distorsions, j'ai attaqué l'enjeu posé par le décalage temporel introduit dans les récepteurs cohérents en présence de dispersion chromatique non-compensé. Cette distorsion est particulièrement nocive aux signaux à rythme symbole élevé. J'ai proposé une nouvelle architecture (Fig. 0.7) combinant compensation indépendant (par dimension) de la dispersion chromatique empêchant le mélange entre les voies (phase et quadrature) et un égaliseur adaptatif à 4 entrées et 2 sorties (complexes). J'ai aussi montré que ce nouvel égaliseur peut aussi fournir une estimation précise du décalage introduit dans le récepteur cohérent à partir de l'étude des coefficients des filtres de l'égaliseur.

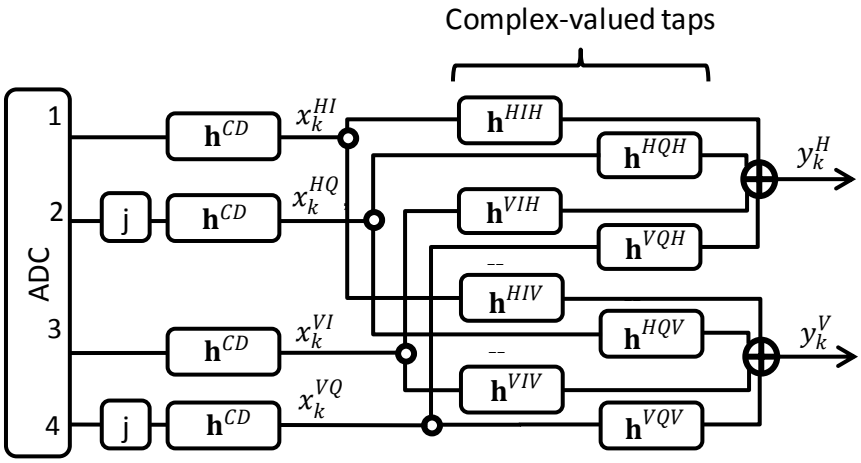

Fig. 0.7: Architecture proposé pour être tolérant au décalage temporel présent dans les récepteurs cohérents.

Finalement, après la minimisation des distorsions introduites dans la chaine de transmission, deux expériences de transmission record ont été démontrées. La première transmission à 400 gigabit par seconde utilisant une seule porteuse sur une distance avec une portée au-delà de 6000 km (Fig. 0.8). L'émetteur est basé sur un convertisseur travaillant à 88 giga-échantillons ; réduction de l'interférence entre-symbole résiduel utilisant des filtres optiques et traitement du signal ; une procédure jointe d'optimisation du rythme symbole et le sur-débit réservé au code correcteur d'erreurs réalisé utilisant le couplage spatial ; et la compensation de non linéarités basé sur la « filtered digital backpropagation ». Ce résultat trace la voie aux

systèmes 400 gigabit par seconde dans une seule porteuse basés sur les composants haute vitesse et le traitement du signal ainsi que le codage de canal avancé.

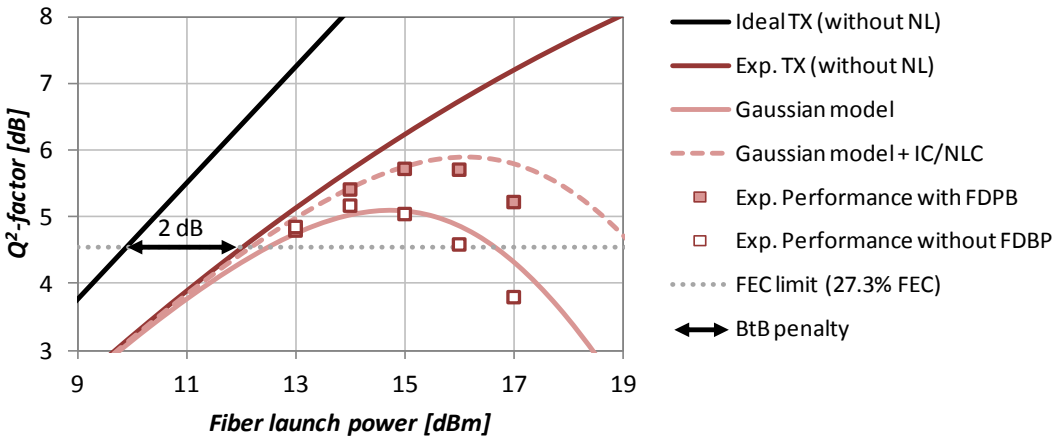

Fig. 0.8: Performance après 6600 km à 400 gigabit par seconde. Carrés vides : performance sans compensation non linéaire. Carrés remplis : avec compensation. Ligne grise pointillé, performance requis.

Pour terminer la thèse, le premier émetteur à 1 térabit par seconde basé sur la synthèse parallèle de plusieurs tranches spectrales a été démontré pour atteindre le rythme symbole record de 124 giga baud et le format de modulation « 32QAM » (Fig. 0.9). Cette technique ouvre la voie à la génération des signaux dont le rythme symbole est bien supérieure à la bande passante des composants optoélectroniques disponibles.

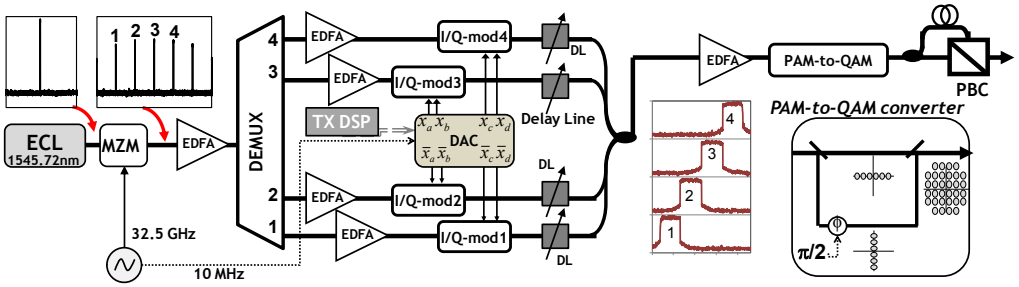

Fig. 0.9: Architecture base sur génération parallèle des multiples tranches spectrales (4) permettant la génération d'un signal 32QAM à 124 giga bauds.

Cette thèse est basée essentiellement sur 8 articles publiés dans les conférences OFC et ECOC dont je suis premier auteur. Parmi ces articles, 2 étaient publiés dans la prestigieuse session « post-deadline » et 2 articles ont été ensuite

détaillés dans le journal « Journal of Lightwave Technology ». Le contenu de ces articles ainsi que ma contribution est listé ensuite :

[1] R. Rios-Muller, J. Renaudier, O. Bertran-Pardo, A. Ghazisaeidi, P. Tran, G. Charlet, and S. Bigo, "Experimental comparison between hybrid-QPSK/8QAM and 4D-32SP-16QAM formats at 31.2 GBaud using Nyquist pulse shaping," in 39th European Conference and Exhibition on Optical Communication (ECOC 2013), 2013.

Dans cet article, on a fait la comparaison expérimentale entre deux formats de modulation permettant une densité spectrale intermédiaire entre le QPSK et le 8QAM. Les formats sont : 4D-32SP-16QAM et Hybrid-QPSK/8QAM. J'ai réalisé les expériences, j'ai adapté les algorithmes de traitement du signal pour le Hybrid-QPSK/8QAM, j'ai fait l'analyse des résultats et rédigé l'article avec l'aide des autres co-auteurs. Le contenu de cet article est présent dans le chapitre 3 de la thèse.

[2] R. Rios-Muller, J. Renaudier, P. Tran, and G. Charlet, "Experimental comparison of two 8-QAM constellations at 200 Gb/s over ultra long-haul transmission link," in Optical Communication (ECOC), 2014 European Conference on, 2014, pp. 1–3.

Dans cet article, on a fait la comparaison expérimentale entre deux formats de modulation à 3 bits par symbole : Star-8QAM et Circular-8QAM. Dans cet article, on compare aussi la différence de tolérance entre les 2 formats par rapport au bruit de phase ainsi que le décalage de fréquence entre l'oscillateur local et la porteuse du signal. On analyse le sur-débit réservé aux symboles pilote pour que les 2 formats aient tolérance similaire aux distorsions de phase. J'ai réalisé les expériences, j'ai adapté les algorithmes de traitement du signal pour le Circular-8QAM, j'ai fait l'analyse des résultats et rédigé l'article avec l'aide des autres co-auteurs. Le contenu de cet article est présent dans le chapitre 3 de la thèse.

[3] R. Rios-Muller, J. Renaudier, and G. Charlet, "Blind receiver skew compensation for long-haul non-dispersion managed systems," in Optical Communication (ECOC), 2014 European Conference on, 2014, pp. 1–3.

[4] R. Rios-Müller, J. Renaudier, and G. Charlet, "Blind Receiver Skew Compensation and Estimation for Long-Haul Non-Dispersion Managed

Systems Using Adaptive Equalizer," J. Light. Technol., vol. 33, no. 7, pp. 1315–1318, 2015.

Dans cet article, j'ai proposé une nouvelle architecture de traitement du signal dans un récepteur cohérent combinant la compensation de la dispersion chromatique et l'égaliseur adaptif. Cette architecture se montre plus tolérante au décalage entre les différentes voies d'échantillonnage dans un récepteur cohérent même en présence de dispersion chromatique non compensée en ligne (situation ou les autres méthodes échouent). Cette architecture permet aussi l'estimation du décalage. J'ai conçu et implémenté la nouvelle architecture et l'estimateur, j'ai réalisé les expériences et j'ai simulé la distorsion (décalage), j'ai fait l'analyse des résultats et rédigé l'article avec l'aide des autres co-auteurs. Le contenu de cet article est présent dans le chapitre 4 de la thèse. Ce papier [3] a été récompensé comme 2ème prix pour le meilleur papier étudiant de la conférence ECOC 2014 et a été invité pour une version prolongée dans le « Journal of Lightwave Technology » [4].

[5] R. Rios-Muller, J. Renaudier, P. Brindel, C. Simonneau, P. Tran, A. Ghazisaeidi, I. Fernandez, L. Schmalen, and G. Charlet, "Optimized spectrally efficient transceiver for 400-Gb/s single carrier transport," in Optical Communication (ECOC), 2014 European Conference on, 2014, pp. 1–3.

[6] R. Rios-Müller, J. Renaudier, P. Brindel, A. Ghazisaeidi, I. Fernandez, P. Tran, C. Simonneau, L. Schmalen, and G. Charlet, "Spectrally-Efficient 400-Gb/s Single Carrier Transport Over 7 200 km," J. Light. Technol., vol. 33, no. 7, pp. 1402–1407, 2015.

Dans cet article, on a démontré la première transmission à 400 gigabit par seconde utilisant une seule porteuse sur une distance avec une portée au-delà de 6000 km. J'ai caractérisé le nouveau convertisseur numérique anagogique, j'ai réalisé les expériences, j'ai fait une partie l'analyse des résultats et rédigé l'article avec l'aide des autres co-auteurs. Le contenu de cet article est présent dans le chapitre 4 de la thèse. Ce papier [5] a été présenté dans la prestigieuse session post-deadline de la conférence ECOC 2014 et a été invité pour une version prolongée dans le « Journal of Lightwave Technology » [6].

[7] R. Rios-Müller, J. Renaudier, L. Schmalen, and G. Charlet, "Joint Coding Rate and Modulation Format Optimization for 8QAM Constellations Using BICM

Mutual Information," in Optical Fiber Communication Conference, 2015, p. W3K–4.

Dans cet article, on a comparé plusieurs formats de modulation à 3 bits par symbole en fonction du rapport signal à bruit avec 2 métriques différentes. On a démontré que le format Rect-8QAM peut être intéressant dans certaines situations, démontrant l'importance l'utilisation de la bonne métrique (information mutuelle généralisée). J'ai réalisé les expériences et simulations, j'ai fait une partie l'analyse des résultats et rédigé l'article avec l'aide des autres co-auteurs. Le contenu de cet article est présent dans le chapitre 3 de la thèse.

[8] R. Rios-Müller, J. Renaudier, P. Brindel, H. Mardoyan, P. Jennevé, L. Schmalen, and G. Charlet, "1-Terabit/s Net Data-Rate Transceiver Based on Single-Carrier Nyquist-Shaped 124 GBaud PDM-32QAM," in Optical Fiber Communication Conference, 2015, p. Th5B–1.

Dans cet article, on a démontré la première transmission à 1 térabit par seconde utilisant un émetteur à multiples tranches spectrales capable de générer un 32QAM à 124 Gbaud. J'ai proposé l'utilisation de l'architecture à tranches, j'ai participé à la conception de l'expérience, j'ai réalisé les expériences, j'ai fait une partie l'analyse des résultats et rédigé l'article avec l'aide des autres co-auteurs. Le contenu de cet article est présent dans le chapitre 4 de la thèse. Ce papier a été présenté dans la prestigieuse session post-deadline de la conférence OFC 2015.

[9] R. Rios-Muller, J. Renaudier, P. Brindel, P. Jenneve, H. Mardoyan, L. Schmalen, and G. Charlet, "Experimental comparison between super-channel and sub-band single-carrier for 400 Gb/s and 800 Gb/s transport," in 2015 European Conference on Optical Communication (ECOC), 2015, pp. 1–3.

Dans cet article, on a comparé la méthode basée sur multiples tranches spectrales avec la solution classique dite « superchannel ». J'ai réalisé les expériences, j'ai fait une partie l'analyse des résultats et rédigé l'article avec l'aide des autres co-auteurs. Le contenu de cet article est présent dans le chapitre 4 de la thèse.

[10] R. Rios-Müller, J. Renaudier, L. Schmalen, and G. Charlet, "Practical Approaches to 400G Single-Carrier Submarine Transmission," in Optical Fiber Communication Conference, Anaheim,California, 2016, p. Th1B.4 (Invited).

Présentation invitée pour parler des systèmes 400 Gb/s après la bonne réception de [5-6].

[11] R. Rios-Muller, J. Renaudier, M. A. Mestre, H. Mardoyan, A. Konczykowska, F. Jorge, B. Duval, and J.-Y. Dupuy, "Multi-Dimension Coded PAM4 Signaling for 100Gb/s Short- Reach Transceivers," in Optical Fiber Communication Conference, Anaheim,California, 2016, p. Th1G.4.

Dans cet article, on a montré un système utilisant la modulation 4D dans les systèmes modulés en intensité avec détection quadratique. J'ai proposé l'utilisation des formats 4D pour ce genre d'application, j'ai fait l'analyse des résultats et rédigé l'article avec l'aide des autres co-auteurs. Le contenu de cet article est présent dans le chapitre 3 de la thèse.

Bibliography

[1] M. K. Weldon, *The Future X Network: A Bell Labs Perspective*. CRC Press, 2016.

[2] J. G. Proakis, *Digital Communications*. McGraw-Hill, 2001.

[3] J. Forney G. D. and G. Ungerboeck, “Modulation and coding for linear Gaussian channels,” *IEEE Trans. Inf. Theory*, vol. 44, no. 6, pp. 2384–2415, Oct. 1998.

[4] D. J. Costello and G. D. Forney, “Channel coding: The road to channel capacity,” *Proc. IEEE*, vol. 95, no. 6, pp. 1150–1177, Jun. 2007.

[5] A. Leven and L. Schmalen, “Status and Recent Advances on Forward Error Correction Technologies for Lightwave Systems,” *J. Light. Technol.*, vol. 32, no. 16, pp. 2735–2750, Aug. 2014.

[6] G. Tzimpragos, C. Kachris, I. B. Djordjevic, M. Cvijetic, D. Soudris, and I. Tomkos, “A Survey on FEC Codes for 100 G and Beyond Optical Networks,” *IEEE Commun. Surv. Tutor.*, vol. 18, no. 1, pp. 209–221, Firstquarter 2016.

[7] K. Zeger and A. Gersho, “Pseudo-Gray coding,” *IEEE Trans. Commun.*, vol. 38, no. 12, pp. 2147–2158, Dec. 1990.

[8] J. Hagenauer, “Soft is Better Than Hard,” in *Communications and Cryptography*, R. E. Blahut, D. J. Costello, U. Maurer, and T. Mittelholzer, Eds. Boston, MA: Springer US, 1994, pp. 155–171.

[9] M. Nolle, F. Frey, R. Elschner, C. Schmidt-Langhorst, A. Napoli, and C. Schubert, “Performance comparison of different 8QAM constellations for the use in flexible optical networks,” in *Optical Fiber Communications Conference and Exhibition (OFC), 2014*, 2014, pp. 1–3.

[10] J. Smith, “Odd-Bit Quadrature Amplitude-Shift Keying,” *IEEE Trans. Commun.*, vol. 23, no. 3, pp. 385–389, Mar. 1975.

[11] C. E. Shannon, “A Mathematical Theory of Communication,” *Bell Syst. Tech. J.*, vol. 27, no. 3, pp. 379–423, Jul. 1948.

[12] I. S. Reed and G. Solomon, “Polynomial Codes Over Certain Finite Fields,” *J. Soc. Ind. Appl. Math.*, vol. 8, no. 2, pp. 300–304, 1960.

[13] P. Elias, “Error-free Coding,” *Trans. IRE Prof. Group Inf. Theory*, vol. 4, no. 4, pp. 29–37, Sep. 1954.

[14] G. D. (George D. Forney, “Concatenated codes.,” 1965.

[15] "ITU-T Recommendation G.975.1 -Forward error correction for high bit-rate DWDM submarine systems." Feb-2014.

[16] R. Gallager, "Low-density parity-check codes," *IRE Trans. Inf. Theory*, vol. 8, no. 1, pp. 21–28, Jan. 1962.

[17] M. Lentmaier, D. G. M. Mitchell, G. Fettweis, and J. Costello D. J., "Asymptotically good LDPC convolutional codes with AWGN channel thresholds close to the Shannon limit," in *2010 6th International Symposium on Turbo Codes and Iterative Information Processing (ISTC)*, 2010, pp. 324–328.

[18] D. Chang, F. Yu, Z. Xiao, N. Stojanovic, F. N. Hauske, Y. Cai, C. Xie, L. Li, X. Xu, and Q. Xiong, "LDPC Convolutional Codes using Layered Decoding Algorithm for High Speed Coherent Optical Transmission," 2012, p. OW1H.4.

[19] S. Kudekar, T. J. Richardson, and R. L. Urbanke, "Threshold Saturation via Spatial Coupling: Why Convolutional LDPC Ensembles Perform So Well over the BEC," *IEEE Trans. Inf. Theory*, vol. 57, no. 2, pp. 803–834, Feb. 2011.

[20] R. W. Hamming, "Error Detecting and Error Correcting Codes," *Bell Syst. Tech. J.*, vol. 29, no. 2, pp. 147–160, Apr. 1950.

[21] R. Tanner, "A recursive approach to low complexity codes," *IEEE Trans. Inf. Theory*, vol. 27, no. 5, pp. 533–547, Sep. 1981.

[22] G. D. Forney, "Codes on Graphs: Fundamentals," *IEEE Trans. Inf. Theory*, vol. 60, no. 10, pp. 5809–5826, Oct. 2014.

[23] N. Wiberg, *Codes and Decoding on General Graphs*. 1996.

[24] A. R. Iyengar, M. Papaleo, P. H. Siegel, J. K. Wolf, A. Vanelli-Coralli, and G. E. Corazza, "Windowed Decoding of Protograph-Based LDPC Convolutional Codes Over Erasure Channels," *IEEE Trans. Inf. Theory*, vol. 58, no. 4, pp. 2303–2320, Apr. 2012.

[25] M. Lentmaier, M. M. Prenda, and G. P. Fettweis, "Efficient message passing scheduling for terminated LDPC convolutional codes," in *2011 IEEE International Symposium on Information Theory Proceedings (ISIT)*, 2011, pp. 1826–1830.

[26] D. A. Morero, M. A. Castrillon, F. A. Ramos, T. A. Goette, O. E. Agazzi, and M. R. Hueda, "Non-Concatenated FEC Codes for Ultra-High Speed Optical Transport Networks," in *2011 IEEE Global Telecommunications Conference (GLOBECOM 2011)*, 2011, pp. 1–5.

[27] L. Schmalen, D. Suikat, D. Rosener, and A. Leven, "Evaluation of left-terminated spatially coupled LDPC codes for optical communications," in *2014 European Conference on Optical Communication (ECOC)*, 2014, pp. 1–3.

[28] E. Desurvire, J. R. Simpson, and P. C. Becker, “High-gain erbium-doped traveling-wave fiber amplifier,” *Opt. Lett.*, vol. 12, no. 11, p. 888, Nov. 1987.

[29] D. M. Baney, P. Gallion, and R. S. Tucker, “Theory and Measurement Techniques for the Noise Figure of Optical Amplifiers,” *Opt. Fiber Technol.*, vol. 6, no. 2, pp. 122–154, Apr. 2000.

[30] “Optical interfaces for multichannel systems with optical amplifiers - ITU Recommendation G.692 (10/98).” .

[31] G. P. Agrawal, *Fiber-Optic Communication Systems*. John Wiley & Sons, 2012.

[32] F. N. Hauske, M. Kuschnerov, B. Spinnler, and B. Lankl, “Optical Performance Monitoring in Digital Coherent Receivers,” *J. Light. Technol.*, vol. 27, no. 16, pp. 3623–3631, Aug. 2009.

[33] E. Ip, A. P. T. Lau, D. J. F. Barros, and J. M. Kahn, “Coherent detection in optical fiber systems,” *Opt. Express*, vol. 16, no. 2, p. 753, 2008.

[34] S. J. Savory, “Digital Coherent Optical Receivers: Algorithms and Subsystems,” *IEEE J. Sel. Top. Quantum Electron.*, vol. 16, no. 5, pp. 1164–1179, Sep. 2010.

[35] F. M. Gardner, “A BPSK/QPSK Timing-Error Detector for Sampled Receivers,” *IEEE Trans. Commun.*, vol. 34, no. 5, pp. 423–429, May 1986.

[36] S. J. Savory, “Digital filters for coherent optical receivers,” *Opt. Express*, vol. 16, no. 2, pp. 804–817, 2008.

[37] M. J. Ready and R. P. Gooch, “Blind equalization based on radius directed adaptation,” in *, 1990 International Conference on Acoustics, Speech, and Signal Processing, 1990. ICASSP-90*, 1990, pp. 1699–1702 vol.3.

[38] D. Rife and R. R. Boorstyn, “Single tone parameter estimation from discrete-time observations,” *IEEE Trans. Inf. Theory*, vol. 20, no. 5, pp. 591–598, Sep. 1974.

[39] M. Morelli and U. Mengali, “Feedforward frequency estimation for PSK: A tutorial review,” *Eur. Trans. Telecommun.*, vol. 9, no. 2, pp. 103–116, Mar. 1998.

[40] F. Munier, E. Alpman, T. Eriksson, A. Svensson, and H. Zirath, “Estimation of Phase Noise for QPSK Modulation over AWGN Channels,” in *Chalmers Publication Library (CPL)*, 2003.

[41] T. Pfau, S. Hoffmann, and R. Noe, “Hardware-Efficient Coherent Digital Receiver Concept With Feedforward Carrier Recovery for -QAM Constellations,” *J. Light. Technol.*, vol. 27, no. 8, pp. 989–999, Apr. 2009.

[42] G. Gavioli, E. Torrengo, G. Bosco, A. Carena, V. Curri, V. Miot, P. Poggiolini, F. Forghieri, S. J. Savory, L. Molle, and R. Freund, “NRZ-PM-QPSK 16 100 Gb/s Transmission Over Installed Fiber With Different Dispersion Maps,” *IEEE Photonics Technol. Lett.*, vol. 22, no. 6, pp. 371–373, Mar. 2010.

[43] A. Carena, G. Bosco, V. Curri, P. Poggiolini, M. T. Taiba, and F. Forghieri, “Statistical characterization of PM-QPSK signals after propagation in uncompensated fiber links,” in *2010 36th European Conference and Exhibition on Optical Communication (ECOC)*, 2010, pp. 1–3.

[44] F. Vacondio, O. Rival, C. Simonneau, E. Grellier, A. Bononi, L. Lorcy, J.-C. Antona, and S. Bigo, “On nonlinear distortions of highly dispersive optical coherent systems,” *Opt. Express*, vol. 20, no. 2, p. 1022, Jan. 2012.

[45] P. Poggiolini, G. Bosco, A. Carena, V. Curri, Y. Jiang, and F. Forghieri, “The GN-Model of Fiber Non-Linear Propagation and its Applications,” *J. Light. Technol.*, vol. 32, no. 4, pp. 694–721, Feb. 2014.

[46] P. Serena and A. Bononi, “A Time-Domain Extended Gaussian Noise Model,” *J. Light. Technol.*, vol. 33, no. 7, pp. 1459–1472, Apr. 2015.

[47] A. Mecozzi and R.-J. Essiambre, “Nonlinear Shannon Limit in Pseudolinear Coherent Systems,” *J. Light. Technol.*, vol. 30, no. 12, pp. 2011–2024, Jun. 2012.

[48] A. Mecozzi, C. B. Clausen, and M. Shtaif, “Analysis of intrachannel nonlinear effects in highly dispersed optical pulse transmission,” *IEEE Photonics Technol. Lett.*, vol. 12, no. 4, pp. 392–394, Apr. 2000.

[49] R. Essiambre and P. J. Winzer, “Fibre nonlinearities in electronically pre-distorted transmission,” in *31st European Conference on Optical Communication, 2005. ECOC 2005*, 2005, vol. 2, pp. 191–192 vol.2.

[50] E. Ip and J. M. Kahn, “Compensation of Dispersion and Nonlinear Impairments Using Digital Backpropagation,” *J. Light. Technol.*, vol. 26, no. 20, pp. 3416–3425, Oct. 2008.

[51] L. B. Du and A. J. Lowery, “Improved single channel backpropagation for intra-channel fiber nonlinearity compensation in long-haul optical communication systems,” *Opt. Express*, vol. 18, no. 16, p. 17075, Aug. 2010.

[52] Z. Tao, L. Dou, W. Yan, L. Li, T. Hoshida, and J. C. Rasmussen, “Multiplier-Free Intrachannel Nonlinearity Compensating Algorithm Operating at Symbol Rate,” *J. Light. Technol.*, vol. 29, no. 17, pp. 2570–2576, Sep. 2011.

[53] P. J. Winzer and R.-J. Essiambre, “Advanced Modulation Formats for High-Capacity Optical Transport Networks,” *J. Light. Technol.*, vol. 24, no. 12, pp. 4711–4728, Dec. 2006.

[54] R. Essiambre, G. Kramer, P. J. Winzer, G. J. Foschini, and B. Goebel, “Capacity Limits of Optical Fiber Networks,” *J. Light. Technol.*, vol. 28, no. 4, pp. 662–701, Feb. 2010.

[55] M. Karlsson and E. Agrell, “Spectrally efficient four-dimensional modulation,” 2012, p. OTu2C.1.

[56] R. Rios-Muller, J. Renaudier, O. Bertran-Pardo, A. Ghazisaeidi, P. Tran, G. Charlet, and S. Bigo, “Experimental comparison between hybrid-QPSK/8QAM and 4D-32SP-16QAM formats at 31.2 GBaud using Nyquist pulse shaping,” in *39th European Conference and Exhibition on Optical Communication (ECOC 2013)*, 2013.

[57] H. Zhang, H. G. Batshon, C. R. Davidson, D. G. Foursa, and A. Pilipetskii, “Multi-Dimensional Coded Modulation in Long-Haul Fiber Optic Transmission,” *J. Light. Technol.*, vol. 33, no. 13, pp. 2876–2883, Jul. 2015.

[58] A. D. Shiner, M. Reimer, A. Borowiec, S. O. Gharan, J. Gaudette, P. Mehta, D. Charlton, K. Roberts, and M. O’Sullivan, “Demonstration of an 8-dimensional modulation format with reduced inter-channel nonlinearities in a polarization multiplexed coherent system,” *Opt. Express*, vol. 22, no. 17, p. 20366, Aug. 2014.

[59] X. Zhou, L. E. Nelson, P. Magill, R. Isaac, B. Zhu, D. W. Peckham, P. I. Borel, and K. Carlson, “High Spectral Efficiency 400 Gb/s Transmission Using PDM Time-Domain Hybrid 32 #x2013;64 QAM and Training-Assisted Carrier Recovery,” *J. Light. Technol.*, vol. 31, no. 7, pp. 999–1005, Apr. 2013.

[60] F. Buchali, W. Idler, H. Buelow, and K. Schuh, “Hybrid Modulation Formats Outperforming 16QAM and 8QAM in Transmission Distance and Filtering with Cascaded WSS,” 2015, p. M3G.4.

[61] S. Chandrasekhar, X. Liu, B. Zhu, and D. W. Peckham, “Transmission of a 1.2-Tb/s 24-carrier no-guard-interval coherent OFDM superchannel over 7200-km of ultra-large-area fiber,” in *35th European Conference on Optical Communication, 2009. ECOC ’09*, 2009, vol. 2009-Supplement, pp. 1–2.

[62] A. Carbo, J. Renaudier, R. Rios-Muller, P. Tran, and G. Charlet, “Experimental analysis of non linear tolerance dependency of multicarrier modulations versus bandwidth efficiency,” in *2015 European Conference on Optical Communication (ECOC)*, 2015, pp. 1–3.

[63] J. Fickers, A. Ghazisaeidi, M. Salsi, F. Horlin, P. Emplit, and G. Charlet, “Multicarrier offset-QAM modulations for coherent optical communication systems,” in *Optical Fiber Communications Conference and Exhibition (OFC), 2014*, 2014, pp. 1–3.

[64] P. Poggiolini, Y. Jiang, A. Carena, G. Bosco, and F. Forghieri, “Analytical results on system maximum reach increase through symbol rate optimization,” 2015, p. Th3D.6.

[65] S. T. Le, M. E. McCarthy, N. Mac Suibhne, A. D. Ellis, and S. K. Turitsyn, “Phase-Conjugated Pilots for Fibre Nonlinearity Compensation in CO-OFDM Transmission,” *J. Light. Technol.*, vol. 33, no. 7, pp. 1308–1314, Apr. 2015.

[66] J. Estaran, D. Zibar, and I. T. Monroy, “Capacity-Approaching Superposition Coding for Optical Fiber Links,” *J. Light. Technol.*, vol. 32, no. 17, pp. 2960–2972, Sep. 2014.

[67] F. Buchali, G. Böcherer, W. Idler, L. Schmalen, P. Schulte, and F. Steiner, “Experimental Demonstration of Capacity Increase and Rate-Adaptation by Probabilistically Shaped 64-QAM,” *ArXiv150908836 Cs Math*, Sep. 2015.

[68] T. H. Lotz, X. Liu, S. Chandrasekhar, P. J. Winzer, H. Haunstein, S. Randel, S. Corteselli, B. Zhu, and D. W. Peckham, “Coded PDM-OFDM Transmission With Shaped 256-Iterative-Polar-Modulation Achieving 11.15-b/s/Hz Intrachannel Spectral Efficiency and 800-km Reach,” *J. Light. Technol.*, vol. 31, no. 4, pp. 538–545, Feb. 2013.

[69] R. Rios-Muller, J. Renaudier, P. Tran, and G. Charlet, “Experimental comparison of two 8-QAM constellations at 200 Gb/s over ultra long-haul transmission link,” in *Optical Communication (ECOC), 2014 European Conference on*, 2014, pp. 1–3.

[70] R. Rios-Müller, J. Renaudier, L. Schmalen, and G. Charlet, “Joint Coding Rate and Modulation Format Optimization for 8QAM Constellations Using BICM Mutual Information,” in *Optical Fiber Communication Conference*, 2015, p. W3K–4.

[71] R. Rios-Muller, J. Renaudier, M. A. Mestre, H. Mardoyan, A. Konczykowska, F. Jorge, B. Duval, and J.-Y. Dupuy, “Multi-Dimension Coded PAM4 Signaling for 100Gb/s Short- Reach Transceivers,” in *Optical Fiber Communication Conference*, Anaheim,California, 2016, p. Th1G.4.

[72] M. Salsi, A. Ghazisaeidi, P. Tran, R. R. Muller, L. Schmalen, J. Renaudier, H. Mardoyan, P. Brindel, G. Charlet, and S. Bigo, “31 Tb/s transmission over 7,200 km using 46 Gbaud PDM-8QAM with optimized error correcting code rate,” in *OptoElectronics and Communications Conference held jointly with 2013 International Conference on Photonics in Switching (OECC/PS), 2013 18th*, 2013, pp. PD3–5.

[73] G. Bosco, V. Curri, A. Carena, P. Poggiolini, and F. Forghieri, “On the Performance of Nyquist-WDM Terabit Superchannels Based on PM-BPSK, PM-QPSK, PM-8QAM or PM-16QAM Subcarriers,” *J. Light. Technol.*, vol. 29, no. 1, pp. 53–61, Jan. 2011.

[74] X. Zhou, J. Yu, M.-F. Huang, Y. Shao, T. Wang, P. Magill, M. Cvijetic, L. Nelson, M. Birk, G. Zhang, S. Ten, H. B. Matthew, and S. K. Mishra, “Transmission of 32-Tb/s Capacity Over 580 km Using RZ-Shaped PDM-8QAM Modulation Format and Cascaded Multimodulus Blind Equalization Algorithm,” *J. Light. Technol.*, vol. 28, no. 4, pp. 456–465, Feb. 2010.

[75] L. Schmalen, A. J. de Lind van Wijngaarden, and S. ten Brink, “Forward Error Correction in Optical Core and Optical Access Networks,” *Bell Labs Tech. J.*, vol. 18, no. 3, pp. 39–66, Dec. 2013.

[76] A. Alvarado, E. Agrell, D. Lavery, R. Maher, and P. Bayvel, “Replacing the Soft-Decision FEC Limit Paradigm in the Design of Optical Communication Systems,” *J. Light. Technol.*, vol. 33, no. 20, pp. 4338–4352, Oct. 2015.

[77] V. Curri, A. Carena, P. Poggiolini, R. Cigliutti, F. Forghieri, C. R. Fludger, and T. Kupfer, “Time-Division Hybrid Modulation Formats: Tx Operation Strategies and Countermeasures to Nonlinear Propagation,” 2014, p. Tu3A.2.

[78] L. Schmalen, A. Alvarado, and R. Rios Muller, “Predicting the Performance of Nonbinary Forward Error Correction in Optical Transmission Experiments,” in *Optical Fiber Communication Conference*, Anaheim,California, 2016, p. M2A.2.

[79] E. Agrell and M. Karlsson, “Power-Efficient Modulation Formats in Coherent Transmission Systems,” *J. Light. Technol.*, vol. 27, no. 22, pp. 5115–5126, Nov. 2009.

[80] G. Foschini, R. Gitlin, and S. Weinstein, “Optimization of Two-Dimensional Signal Constellations in the Presence of Gaussian Noise,” *IEEE Trans. Commun.*, vol. 22, no. 1, pp. 28–38, Jan. 1974.

[81] J. Renaudier, O. Bertran-Pardo, H. Mardoyan, M. Salsi, P. Tran, E. Dutisseuil, G. Charlet, and S. Bigo, “Experimental comparison of 28Gbaud polarization switched-and polarization division multiplexed-QPSK in WDM long-haul transmission system,” in *2011 37th European Conference and Exhibition on Optical Communication (ECOC)*, 2011, pp. 1–3.

[82] J. Renaudier, O. Bertran-Pardo, A. Ghazisaeidi, P. Tran, H. Mardoyan, P. Brindel, A. Voicila, G. Charlet, and S. Bigo, “Experimental transmission of Nyquist pulse shaped 4-D coded modulation using dual polarization 16QAM set-partitioning schemes at 28 Gbaud,” in *Optical Fiber Communication Conference and Exposition and the National Fiber Optic Engineers Conference (OFC/NFOEC), 2013*, 2013, pp. 1–3.

[83] T. A. Eriksson, M. Sjödin, P. Johannisson, P. A. Andrekson, and M. Karlsson, “Comparison of 128-SP-QAM and PM-16QAM in long-haul WDM transmission,” *Opt. Express*, vol. 21, no. 16, p. 19269, Aug. 2013.

[84] J. K. Fischer, S. Alreesh, R. Elschner, F. Frey, M. Nolle, C. Schmidt-Langhorst, and C. Schubert, “Bandwidth-Variable Transceivers based on Four-Dimensional Modulation Formats,” *J. Light. Technol.*, vol. 32, no. 16, pp. 2886–2895, Aug. 2014.

[85] A. Alvarado and E. Agrell, “Four-Dimensional Coded Modulation with Bit-Wise Decoders for Future Optical Communications,” *J. Light. Technol.*, vol. 33, no. 10, pp. 1993–2003, May 2015.

[86] M. Chagnon, M. Morsy-Osman, M. Poulin, C. Paquet, S. Lessard, and D. V. Plant, “Experimental Parametric Study of a Silicon Photonic Modulator Enabled 112-Gb/s PAM Transmission System With a DAC and ADC,” *J. Light. Technol.*, vol. 33, no. 7, pp. 1380–1387, Apr. 2015.

[87] M. A. Mestre, H. Mardoyan, A. Konczykowska, R. Rios-Muller, J. Renaudier, F. Jorge, B. Duval, J.-Y. Dupuy, A. Ghazisaeidi, P. Jenneve, and S. Bigo, “Direct detection transceiver at 150-Gbit/s net data rate using PAM 8 for optical interconnects,” in *2015 European Conference on Optical Communication (ECOC)*, 2015, pp. 1–3.

[88] M. Sjödin, B. J. Puttnam, P. Johannisson, S. Shinada, N. Wada, P. A. Andrekson, and M. Karlsson, “Transmission of PM-QPSK and PS-QPSK with different fiber span lengths,” *Opt. Express*, vol. 20, no. 7, p. 7544, Mar. 2012.

[89] X. Xiao and F. Li, “Real-Time Demonstration of 100Gbps Class Dual-carrier DDO-16QAM-DMT Transmission with Directly Modulated Laser,” 2014, p. M2E.6.

[90] D. Sadot, G. Dorman, A. Gorshtein, E. Sonkin, and O. Vidal, “Single channel 112Gbit/sec PAM4 at 56Gbaud with digital signal processing for data centers applications,” in *Optical Fiber Communications Conference and Exhibition (OFC), 2015*, 2015, pp. 1–3.

[91] J. Renaudier, R. Rios Muller, M. A. Mestre, H. Mardoyan, A. Konczykowska, F. Jorge, B. Duval, and J.-Y. Dupuy, “Multi Rate IMDD Transceivers for Optical Interconnects Using Coded Modulation,” in *Optical Fiber Communication Conference*, Anaheim,California, 2016, p. Tu2J.2.

[92] A. Konczykowska, F. Jorge, J.-Y. Dupuy, M. Riet, V. Nodjiadjim, H. Aubry, and A. Adamiecki, “84 GBd (168 Gbit/s) PAM-4 3.7 Vpp power DAC in InP DHBT for short reach and long haul optical networks,” *Electron. Lett.*, vol. 51, no. 20, pp. 1591–1593, 2015.

[93] L. Schmalen, F. Buchali, A. Leven, and S. ten Brink, “A Generic Tool for Assessing the Soft-FEC Performance in Optical Transmission Experiments,” *IEEE Photonics Technol. Lett.*, vol. 24, no. 1, pp. 40–42, Jan. 2012.

[94] G. E. Moore, “Cramming More Components Onto Integrated Circuits,” *Proc. IEEE*, vol. 86, no. 1, pp. 82–85, Jan. 1998.

[95] I. Fatadin, S. J. Savory, and D. Ives, “Compensation of Quadrature Imbalance in an Optical QPSK Coherent Receiver,” *IEEE Photonics Technol. Lett.*, vol. 20, no. 20, pp. 1733–1735, Oct. 2008.

[96] T. Tanimura, S. Oda, T. Tanaka, T. Hoshida, Z. Tao, and J. C. Rasmussen, “A simple digital skew compensator for coherent receiver,” in *35th European Conference on Optical Communication, 2009. ECOC ’09*, 2009, pp. 1–2.

[97] N. Stojanovic and X. Changsong, “An Efficient Method for Skew Estimation and Compensation in Coherent Receivers,” *IEEE Photonics Technol. Lett.*, vol. 28, no. 4, pp. 489–492, Feb. 2016.

[98] R. Rios-Muller, J. Renaudier, and G. Charlet, “Blind receiver skew compensation for long-haul non-dispersion managed systems,” in *Optical Communication (ECOC), 2014 European Conference on*, 2014, pp. 1–3.

[99] R. Rios-Müller, J. Renaudier, and G. Charlet, “Blind Receiver Skew Compensation and Estimation for Long-Haul Non-Dispersion Managed Systems Using Adaptive Equalizer,” *J. Light. Technol.*, vol. 33, no. 7, pp. 1315–1318, 2015.

[100] R. Rios-Müller, J. Renaudier, L. Schmalen, and G. Charlet, “Practical Approaches to 400G Single-Carrier Submarine Transmission,” in *Optical Fiber Communication Conference*, Anaheim,California, 2016, p. Th1B.4 (Invited).

[101] R. Rios-Muller, J. Renaudier, P. Brindel, C. Simonneau, P. Tran, A. Ghazisaeidi, I. Fernandez, L. Schmalen, and G. Charlet, “Optimized spectrally efficient transceiver for 400-Gb/s single carrier transport,” in *Optical Communication (ECOC), 2014 European Conference on*, 2014, pp. 1–3.

[102] R. Rios-Müller, J. Renaudier, P. Brindel, A. Ghazisaeidi, I. Fernandez, P. Tran, C. Simonneau, L. Schmalen, and G. Charlet, “Spectrally-Efficient 400-Gb/s Single Carrier Transport Over 7 200 km,” *J. Light. Technol.*, vol. 33, no. 7, pp. 1402–1407, 2015.

[103] R. Rios-Müller, J. Renaudier, P. Brindel, H. Mardoyan, P. Jennevé, L. Schmalen, and G. Charlet, “1-Terabit/s Net Data-Rate Transceiver Based on Single-Carrier Nyquist-Shaped 124 GBaud PDM-32QAM,” in *Optical Fiber Communication Conference*, 2015, p. Th5B–1.

[104] R. Rios-Muller, J. Renaudier, P. Brindel, P. Jenneve, H. Mardoyan, L. Schmalen, and G. Charlet, “Experimental comparison between super-channel and sub-band single-carrier for 400 Gb/s and 800 Gb/s transport,” in *2015 European Conference on Optical Communication (ECOC)*, 2015, pp. 1–3.

[105] J.-X. Cai, H. Zhang, H. G. Batshon, M. Mazurczyk, O. V. Sinkin, Y. Sun, A. Pilipetskii, and D. G. Foursa, “Transmission over 9,100 km with a capacity of 49.3 Tb/s using variable spectral efficiency 16 QAM based coded modulation,” in *Optical Fiber Communications Conference and Exhibition (OFC), 2014*, 2014, pp. 1–3.

[106] L. Carvalho, C. Floridia, C. Franciscangelis, V. Parahyba, E. P. da Silva, N. G. Gonzalez, and J. Oliveira, “WDM Transmission of 3x1.12-Tb/s PDM-16QAM Superchannels with 6.5-b/s/Hz in a 162.5-GHz Flexible-Grid using only Optical Spectral Shaping,” 2014, p. M3C.3.

[107] J. Renaudier, R. Rios-Muller, L. Schmalen, M. Salsi, P. Tran, G. Charlet, and S. Bigo, “1-Tb/s Transceiver Spanning Over Just Three 50-GHz Frequency Slots for Long-Haul Systems,” in *Optical Communication (ECOC 2013), 39th European Conference and Exhibition on*, 2013, p. PD2–D.

[108] M. S. Faruk and K. Kikuchi, “Compensation for In-Phase/Quadrature Imbalance in Coherent-Receiver Front End for Optical Quadrature Amplitude Modulation,” *IEEE Photonics J.*, vol. 5, no. 2, pp. 7800110–7800110, Apr. 2013.

[109] M. Paskov, D. Lavery, and S. J. Savory, “Blind Equalization of Receiver In-Phase/Quadrature Skew in the Presence of Nyquist Filtering,” *IEEE Photonics Technol. Lett.*, vol. 25, no. 24, pp. 2446–2449, Dec. 2013.

[110] B. Picinbono and P. Chevalier, “Widely linear estimation with complex data,” *IEEE Trans. Signal Process.*, vol. 43, no. 8, pp. 2030–2033, Aug. 1995.

[111] S. Randel, D. Pilori, S. Corteselli, G. Raybon, A. Adamiecki, A. Gnauck, S. Chandrasekhar, P. Winzer, L. Altenhain, A. Bielik, and R. Schmid, “All-electronic flexibly programmable 864-Gb/s single-carrier PDM-64-QAM,” in *Optical Fiber Communications Conference and Exhibition (OFC), 2014*, 2014, pp. 1–3.

[112] H. Zhang, J. Cai, H. G. Batshon, M. Mazurczyk, O. V. Sinkin, D. G. Foursa, A. Pilipetskii, G. Mohs, and N. S. Bergano, “200 Gb/s and dual-wavelength 400 Gb/s transmission over transpacific distance at 6 b/s/Hz spectral efficiency,” in *Optical Fiber Communication Conference and Exposition and the National Fiber Optic Engineers Conference (OFC/NFOEC), 2013*, 2013, pp. 1–3.

[113] G. Raybon, A. L. Adamiecki, P. Winzer, C. Xie, A. Konczykowska, F. Jorge, J.-Y. Dupuy, L. L. Buhl, S. Chandrashekhar, S. Draving, M. Grove, and K. Rush,

"Single-carrier 400G interface and 10-channel WDM transmission over 4,800 km using all-ETDM 107-Gbaud PDM-QPSK," in *Optical Fiber Communication Conference and Exposition and the National Fiber Optic Engineers Conference (OFC/NFOEC), 2013*, 2013, pp. 1–4.

[114] P. J. Winzer, A. H. Gnauck, S. Chandrasekhar, S. Draving, J. Evangelista, and B. Zhu, "Generation and 1,200-km transmission of 448-Gb/s ETDM 56-Gbaud PDM 16-QAM using a single I/Q modulator," in *2010 36th European Conference and Exhibition on Optical Communication (ECOC)*, 2010, pp. 1–3.

[115] J. Renaudier, W. Idler, O. Bertran-Pardo, F. Buchali, K. Schuh, H. Mardoyan, P. Tran, G. Charlet, and S. Bigo, "Long-haul WDM transmission of 448 Gbit/s polarisation-division multiplexed 16-ary quadrature amplitude modulation using coherent detection," *Electron. Lett.*, vol. 47, no. 17, pp. 973–975, Aug. 2011.

[116] O. Bertran-Pardo, J. Renaudier, H. Mardoyan, P. Tran, R. Rios-Muller, A. Konczykowska, J.-Y. Dupuy, F. Jorge, M. Riet, B. Duval, and others, "Transmission of 50-GHz-spaced single-carrier channels at 516Gb/s over 600km," in *Optical Fiber Communication Conference*, 2013, p. OTh4E–2.

[117] L. Schmalen, V. Aref, J. Cho, D. Suikat, D. Rosener, and A. Leven, "Spatially Coupled Soft-Decision Error Correction for Future Lightwave Systems," *J. Light. Technol.*, vol. 33, no. 5, pp. 1109–1116, Mar. 2015.

[118] Y. Zhang and I. B. Djordjevic, "Staircase rate-adaptive LDPC-coded modulation for high-speed intelligent optical transmission," in *Optical Fiber Communications Conference and Exhibition (OFC), 2014*, 2014, pp. 1–3.

[119] M. Beermann, F. Wickert, and P. Vary, "Highly flexible design of multi-rate multi-length quasi-cyclic LDPC codes," in *2014 8th International Symposium on Turbo Codes and Iterative Information Processing (ISTC)*, 2014, pp. 37–41.

[120] A. Ghazisaeidi, L. Schmalen, I. F. de J. Ruiz, P. Tran, C. Simonneau, P. Brindel, and G. Charlet, "Transoceanic Transmission Systems Using Adaptive Multirate FECs," *J. Light. Technol.*, vol. 33, no. 7, pp. 1479–1487, Apr. 2015.

[121] I. F. de J. Ruiz, A. Ghazisaeidi, and G. Charlet, "Optimization rules and performance analysis of filtered digital backpropagation," in *2015 European Conference on Optical Communication (ECOC)*, 2015, pp. 1–3.

[122] G. Raybon, A. Adamiecki, P. P. J. Winzer, M. Montoliu, S. Randel, A. Umbach, M. Margraf, J. Stephan, S. Draving, M. Grove, and K. Rush, "All-ETDM 107-Gbaud PDM-16QAM (856-Gb/s) transmitter and coherent receiver," in *39th European Conference and Exhibition on Optical Communication (ECOC 2013)*, 2013, pp. 1–3.

[123] G. Raybon, A. Adamiecki, J. Cho, P. Winzer, A. Konczykowska, F. Jorge, J.-Y. Dupuy, M. Riet, B. Duval, K. Kim, S. Randel, D. Pilori, B. Guan, N. Fontaine, and E. C. Burrows, “Single-carrier all-ETDM 1.08-Terabit/s line rate PDM-64-QAM transmitter using a high-speed 3-bit multiplexing DAC,” in *Photonics Conference (IPC), 2015*, 2015, pp. 1–2.

[124] J. Renaudier, A. Ghazisaeidi, P. Tran, O. Bertran-Pardo, G. Charlet, and S. Bigo, “Long-haul transmission of 1-Tb/s superchannels, 175-GHz spaced, over SSMF using Nyquist pulse shaping and flex-grid WDM architecture,” in *39th European Conference and Exhibition on Optical Communication (ECOC 2013)*, 2013, pp. 1–4.

[125] F. Buchali, K. Schuh, L. Schmalen, W. Idler, E. Lach, and A. Leven, “1-Tbit/s dual-carrier DP 64QAM transmission at 64Gbaud with 40% overhead soft-FEC over 320km SSMF,” in *Optical Fiber Communication Conference and Exposition and the National Fiber Optic Engineers Conference (OFC/NFOEC), 2013*, 2013, pp. 1–3.

[126] D. J. Geisler, N. K. Fontaine, R. P. Scott, T. He, L. Paraschis, O. Gerstel, J. P. Heritage, and S. J. B. Yoo, “Bandwidth scalable, coherent transmitter based on the parallel synthesis of multiple spectral slices using optical arbitrary waveform generation,” *Opt. Express*, vol. 19, no. 9, p. 8242, Apr. 2011.

[127] H. Mardoyan, R. Rios-Müller, M. A. Mestre, P. Jennevé, L. Schmalen, A. Ghazisaeidi, P. Tran, S. Bigo, and J. Renaudier, “Transmission of Single-Carrier Nyquist-Shaped 1-Tb/s Line-Rate Signal over 3,000 km,” in *Optical Fiber Communication Conference*, 2015, p. W3G–2.

[128] B. Guan, N. K. Fontaine, R. Ryf, S. Chen, H. Chen, G. Raybon, C. Xie, R. P. Scott, and S. J. B. Yoo, “Optical Spectrally Sliced Transmitter for High Fidelity and Bandwidth Scalable Waveform Generation,” *J. Light. Technol.*, vol. 34, no. 2, pp. 737–744, Jan. 2016.

[129] N. K. Fontaine, X. Liu, S. Chandrasekhar, R. Ryf, S. Randel, P. Winzer, R. Delbue, P. Pupalaikis, and A. Sureka, “Fiber nonlinearity compensation by digital backpropagation of an entire 1.2-Tb/s superchannel using a full-field spectrally-sliced receiver,” in *39th European Conference and Exhibition on Optical Communication (ECOC 2013)*, 2013, pp. 1–3.

Publications

As first author

[I] R. Rios-Muller, J. Renaudier, O. Bertran-Pardo, A. Ghazisaeidi, P. Tran, G. Charlet, and S. Bigo, “Experimental comparison between hybrid-QPSK/8QAM and 4D-32SP-16QAM formats at 31.2 GBaud using Nyquist pulse shaping,” in 39th European Conference and Exhibition on Optical Communication (ECOC 2013), 2013.

[II] R. Rios-Muller, J. Renaudier, P. Tran, and G. Charlet, “Experimental comparison of two 8-QAM constellations at 200 Gb/s over ultra long-haul transmission link,” in Optical Communication (ECOC), 2014 European Conference on, 2014, pp. 1–3.

[III] R. Rios-Muller, J. Renaudier, and G. Charlet, “Blind receiver skew compensation for long-haul non-dispersion managed systems,” in Optical Communication (ECOC), 2014 European Conference on, 2014, pp. 1–3.

[IV] R. Rios-Muller, J. Renaudier, P. Brindel, C. Simonneau, P. Tran, A. Ghazisaeidi, I. Fernandez, L. Schmalen, and G. Charlet, “Optimized spectrally efficient transceiver for 400-Gb/s single carrier transport,” in Optical Communication (ECOC), 2014 European Conference on, 2014, pp. 1–3.

[V] R. Rios-Müller, J. Renaudier, L. Schmalen, and G. Charlet, “Joint Coding Rate and Modulation Format Optimization for 8QAM Constellations Using BICM Mutual Information,” in Optical Fiber Communication Conference, 2015, p. W3K–4.

[VI] R. Rios-Müller, J. Renaudier, P. Brindel, H. Mardoyan, P. Jennevé, L. Schmalen, and G. Charlet, “1-Terabit/s Net Data-Rate Transceiver Based on Single-Carrier Nyquist-Shaped 124 GBaud PDM-32QAM,” in Optical Fiber Communication Conference, 2015, p. Th5B–1.

[VII] R. Rios-Müller, J. Renaudier, and G. Charlet, “Blind Receiver Skew Compensation and Estimation for Long-Haul Non-Dispersion Managed Systems Using Adaptive Equalizer,” J. Light. Technol., vol. 33, no. 7, pp. 1315–1318, 2015.

[VIII] R. Rios-Müller, J. Renaudier, P. Brindel, A. Ghazisaeidi, I. Fernandez, P. Tran, C. Simonneau, L. Schmalen, and G. Charlet, “Spectrally-Efficient 400-Gb/s Single Carrier Transport Over 7 200 km,” J. Light. Technol., vol. 33, no. 7, pp. 1402–1407, 2015.

[IX] R. Rios-Muller, J. Renaudier, P. Brindel, P. Jenneve, H. Mardoyan, L. Schmalen, and G. Charlet, “Experimental comparison between super-channel and sub-band single-carrier for 400 Gb/s and 800 Gb/s transport,” in 2015 European Conference on Optical Communication (ECOC), 2015, pp. 1–3.

[X] R. Rios-Müller, J. Renaudier, L. Schmalen, and G. Charlet, “Practical Approaches to 400G Single-Carrier Submarine Transmission,” in Optical Fiber Communication Conference, Anaheim,California, 2016, p. Th1B.4 (Invited).

[XI] R. Rios-Muller, J. Renaudier, M. A. Mestre, H. Mardoyan, A. Konczykowska, F. Jorge, B. Duval, and J.-Y. Dupuy, “Multi-Dimension Coded PAM4 Signaling for 100Gb/s Short- Reach Transceivers,” in Optical Fiber Communication Conference, Anaheim,California, 2016, p. Th1G.4.

As co-author

[XII] O. Bertran-Pardo, J. Renaudier, H. Mardoyan, P. Tran, R. Rios-Muller, A. Konczykowska, J.-Y. Dupuy, F. Jorge, M. Riet, B. Duval, and others, “Transmission of 50-GHz-spaced single-carrier channels at 516Gb/s over 600km,” in Optical Fiber Communication Conference, 2013, p. OTh4E–2.

[XIII] M. Salsi, A. Ghazisaeidi, P. Tran, R. R. Muller, L. Schmalen, J. Renaudier, H. Mardoyan, P. Brindel, G. Charlet, and S. Bigo, “31 Tb/s transmission over 7,200 km using 46 Gbaud PDM-8QAM with optimized error correcting code rate,” in OptoElectronics and Communications Conference held jointly with 2013 International Conference on Photonics in Switching (OECC/PS), 2013 18th, 2013, pp. PD3–5.

[XIV] M. Salsi, R. Muller, J. Renaudier, P. Tran, L. Schmalen, A. Ghazisaeid, H. Mardoyan, P. Brindel, G. Charlet, and S. Bigo, “38.75 Tb/s transmission experiment over transoceanic distance,” in Optical Communication (ECOC 2013), 39th European Conference and Exhibition on, 2013, p. PD3–E.

[XV] J. Renaudier, R. Rios-Muller, L. Schmalen, M. Salsi, P. Tran, G. Charlet, and S. Bigo, “1-Tb/s Transceiver Spanning Over Just Three 50-GHz Frequency Slots for Long-Haul Systems,” in Optical Communication (ECOC 2013), 39th European Conference and Exhibition on, 2013, p. PD2–D.

[XVI] G. Charlet, P. Tran, P. Brindel, and R. Rios-Muller, “On the emulation of high spectral efficiency systems in laboratory experiments,” in Optical Fiber Communications Conference and Exhibition (OFC), 2014, 2014, pp. 1–3.

[XVII] J. Renaudier, R. R. Muller, L. Schmalen, P. Tran, P. Brindel, and G. Charlet, “1-Tb/s PDM-32QAM superchannel transmission at 6.7-b/s/Hz over SSMF and 150-GHz-grid ROADMs,” in Optical Communication (ECOC), 2014 European Conference on, 2014, pp. 1–3.

[XVIII] P. Genevaux, G. Labroille, J.-F. Morizur, C. Simonneau, G. Campbell, P. K. Lam, N. Treps, P. Brindel, R. R. Muller, J. Renaudier, and others, “3 Modes transmission using hybrid separation with high mode selectivity and low losses spatial mode multiplexer,” in Optical Communication (ECOC), 2014 European Conference on, 2014, pp. 1–3.

[XIX] J. Renaudier, R. Rios-Müller, L. Schmalen, and G. Charlet, “Spectrally Efficient 1Tb/s Transceivers,” in Optical Fiber Communication Conference, 2015, p. M2G–3.

[XX] H. Mardoyan, R. Rios-Müller, M. A. Mestre, P. Jennevé, L. Schmalen, A. Ghazisaeidi, P. Tran, S. Bigo, and J. Renaudier, “Transmission of Single-Carrier Nyquist-Shaped 1-Tb/s Line-Rate Signal over 3,000 km,” in Optical Fiber Communication Conference, 2015, p. W3G–2.

[XXI] J. Renaudier, R. Rios-Müller, P. Tran, P. L. Schmalen, and G. Charlet, “Spectrally Efficient 1-Tb/s Transceivers for Long-Haul Optical Systems,” J. Light. Technol., vol. 33, no. 7, pp. 1452–1458, 2015.

[XXII] A. Carbo, J. Renaudier, R. Rios-Muller, P. Tran, and G. Charlet, “Experimental analysis of non linear tolerance dependency of multicarrier modulations versus bandwidth efficiency,” in 2015 European Conference on Optical Communication (ECOC), 2015, pp. 1–3.

[XXIII] M. A. Mestre, H. Mardoyan, A. Konczykowska, R. Rios-Muller, J. Renaudier, F. Jorge, B. Duval, J.-Y. Dupuy, A. Ghazisaeidi, P. Jenneve, and S. Bigo, “Direct detection transceiver at 150-Gbit/s net data rate using PAM 8 for optical interconnects,” in 2015 European Conference on Optical Communication (ECOC), 2015, pp. 1–3.

[XXIV] J. Renaudier, R. Rios-Muller, M. A. Mestre, H. Mardoyan, A. Konczykowska, F. Jorge, B. Duval, and J.-Y. Dupuy, “Multi Rate IMDD Transceivers for Optical Interconnects Using Coded Modulation,” in Optical Fiber Communication Conference, Anaheim,California, 2016, p. Tu2J.2.

[XXV] L. Schmalen, A. Alvarado, and R. Rios Muller, “Predicting the Performance of Nonbinary Forward Error Correction in Optical Transmission Experiments,” in Optical Fiber Communication Conference, Anaheim,California, 2016, p. M2A.2.

[XXVI] M. A. Mestre, H. Mardoyan, C. Caillaud, R. Rios-Muller, J. Renaudier, P. Jenneve, F. Blache, F. Pommereau, J. Decobert, F. Jorge, P. Charbonnier, A. Konczykowska, J.-Y. dupuy, K. Mekhazni, J.-F. Paret, M. Faugeron, F. Mallecot, M. Achouche, and S. Bigo, “Compact InP-based DFB-EAM Enabling PAM-4 112 Gb/s Transmission over 2 km,” J. Light. Technol., vol. PP, no. 99, pp. 1–1, 2015.

[XXVII] A. Carbo Meseguer, J. Renaudier, R. Rios-Muller, P. Tran, and G. Charlet, “Impact of Bandwidth Efficiency in Nonlinear Tolerance of Multicarrier Modulations,” J. Light. Technol., vol. PP, no. 99, pp. 1–1, 2015.

Patents

[XXVIII] J. Renaudier, R. Rios Muller, and G. Charlet, “Method and Device for Optical Data Transmission,” US20150349894, 03-Dec-2015.

[XXIX] G. Charlet, R. Rios Muller, and J. Renaudier, “Optical coherent transponder,” EP2713532, 02-Apr-2014.

[XXX] G. Charlet and R. Rios Muller, “Multiplexing system and demultiplexing system for WDM channel transmission,” EP2919404, 16-Sep-2015.